

## THE ACS NEARBY GALAXY SURVEY TREASURY

JULIANNE J. DALCANTON<sup>1</sup>, BENJAMIN F. WILLIAMS<sup>1</sup>, ANIL C. SETH<sup>2</sup>, ANDREW DOLPHIN<sup>3</sup>, JON HOLTZMAN<sup>4</sup>, KEITH ROSEMA<sup>1</sup>, EVAN D. SKILLMAN<sup>5</sup>, ANDREW COLE<sup>6</sup>, LÉO GIRARDI<sup>7</sup>, STEPHANIE M. GOGARTEN<sup>1</sup>, IGOR D. KARACHENTSEV<sup>8</sup>, KNUT OLSEN<sup>9</sup>, DANIEL WEISZ<sup>5</sup>, CHARLOTTE CHRISTENSEN<sup>1</sup>, KEN FREEMAN<sup>11</sup>, KAROLINE GILBERT<sup>1</sup>, CARME GALLART<sup>12</sup>, JASON HARRIS<sup>13</sup>, PAUL HODGE<sup>1</sup>, ROELOF S. DE JONG<sup>10</sup>, VALENTINA KARACHENTSEVA<sup>14</sup>, MARIO MATEO<sup>15</sup>, PETER B. STETSON<sup>16</sup>, MARITZA TAVAREZ<sup>17</sup>, DENNIS ZARITSKY<sup>13</sup>, FABIO GOVERNATO<sup>1</sup>, THOMAS QUINN<sup>1</sup>

*Draft version May 25, 2009*

## ABSTRACT

The ACS Nearby Galaxy Survey Treasury (ANGST) is a systematic survey to establish a legacy of uniform multi-color photometry of resolved stars for a volume-limited sample of nearby galaxies ( $D < 4$  Mpc). The survey volume encompasses 69 galaxies in diverse environments, including close pairs, small & large groups, filaments, and truly isolated regions. The galaxies include a nearly complete range of morphological types spanning a factor of  $\sim 10^4$  in luminosity and star formation rate. The survey data consists of images taken with the Advanced Camera for Surveys (ACS) on the *Hubble Space Telescope* (HST), supplemented with archival data and new Wide Field Planetary Camera (WFPC2) imaging taken after the failure of ACS. Survey images include wide field tilings covering the full radial extent of each galaxy, and single deep pointings in uncrowded regions of the most massive galaxies in the volume. The new wide field imaging in ANGST reaches median 50% completenesses of  $m_{F475W} = 28.0$  mag,  $m_{F606W} = 27.3$  mag, and  $m_{F814W} = 27.3$  mag, several magnitudes below the tip of the red giant branch (TRGB). The deep fields reach magnitudes sufficient to fully resolve the structure in the red clump (RC). The resulting photometric catalogs are publicly accessible and contain over 34 million photometric measurements of  $>14$  million stars. In this paper we present the details of the sample selection, imaging, data reduction, and the resulting photometric catalogs, along with an analysis of the photometric uncertainties (systematic and random), for both the ACS and WFPC2 imaging. We also present uniformly derived relative distances measured from the apparent magnitude of the TRGB.

*Subject headings:* galaxies: formation — galaxies: stellar content – catalogs – surveys –

## 1. INTRODUCTION

The study of nearby galaxies has been revolutionized by the *Hubble Space Telescope* (HST). The high spatial resolutions of WFPC2 and ACS reveal individual stars and parsec-scale structures, permitting studies of stellar populations, star formation histories, and stellar clusters for galaxies out to several megaparsecs. However, despite the large number of HST projects on these topics, past observations have been piecemeal and lack a unifying, coherent observational strategy in spite of the considerable overlap in the core scientific goals of many of the projects. Within a single galaxy, or from galaxy to galaxy, the locations of the HST exposures have been chaotic (having been chosen independently and for different purposes), and the filters and depths of the exposures have been highly variable. While past observations have provided dramatic insights into the star formation histories of individual systems, the resulting archive complicates any uniform comparative study of galaxies in the Local Universe and dramatically reduces the scientific legacy of this data set.

The ACS Nearby Galaxy Survey Treasury (ANGST) program aims to rectify this situation by creating a uniform, multi-color archive of observations of resolved stel-

<sup>1</sup> Department of Astronomy, Box 351580, University of Washington, Seattle, WA 98195; jd@astro.washington.edu; ben@astro.washington.edu; krosema@astro.washington.edu; stephanie@astro.washington.edu; christensen@astro.washington.edu; becker@astro.washington.edu; fabio@astro.washington.edu; trq@astro.washington.edu

<sup>2</sup> CfA Fellow, Harvard-Smithsonian Center for Astrophysics, 60 Garden Street, Cambridge, MA 02138; aseth@cfa.harvard.edu

<sup>3</sup> Raytheon, 1151 E. Hermans Road, Tucson, AZ 85756; adolphin@raytheon.com

<sup>4</sup> Department of Astronomy, New Mexico State University, Box 30001, 1320 Frenger St., Las Cruces, NM 88003; holtz@nmsu.edu

<sup>5</sup> Department of Astronomy, University of Minnesota, 116 Church St. SE, Minneapolis, MN 55455; dweisz@astro.umn.edu; skillman@astro.umn.edu

<sup>6</sup> School of Mathematics and Physics, University of Tasmania, Hobart, Tasmania, Australia; andrew.cole@utas.edu.au

<sup>7</sup> Osservatorio Astronomico di Padova – INAF, Vicolo dell'Osservatorio 5, I-35122 Padova, Italy; leo.girardi@oapd.inaf.it

<sup>8</sup> Special Astrophysical Observatory, Russian Academy of Sciences, Nizhnji Arkhyz, Karachai-Circassia Republic 369167, Russia; ikar@luna.sao.ru

<sup>9</sup> NOAO, National Optical Astronomy Observatory 950 N. Cherry Ave., Tucson, AZ 85719; kolsen@noao.edu

<sup>10</sup> Space Telescope Science Institute, 3700 San Martin Dr., Baltimore, MD 21218; dejong@stsci.edu

<sup>11</sup> Mount Stromlo Observatory, Research School of Astronomy and Astrophysics, Mount Stromlo Observatory, The Australian National University, ACT 0200 Australia; kcf@mso.anu.edu.au

<sup>12</sup> Instituto de Astrofísica de Canarias, Vía Lctea, s/n, 38200 La Laguna, Tenerife, SPAIN; carme@iac.es

<sup>13</sup> Steward Observatory, University of Arizona, 933 North Cherry Avenue, Tucson, AZ 85721; jharris@as.arizona.edu; dennis@fishingholes.as.arizona.edu

<sup>14</sup> Astronomical Observatory of Kiev University, Observatorna 3, 254053, Kiev, Ukraine; vkarach@observ.univ.kiev.ua

<sup>15</sup> Department of Astronomy, University of Michigan, 830 Den-

inson Building, Ann Arbor, MI 48109-1090; mmateo@umich.edu

<sup>16</sup> Dominion Astrophysical Observatory, Herzberg Institute of Astrophysics, National Research Council, 5071 West Saanich Road, Victoria, BC V9E 2E7, Canada; Peter.Stetson@nrc-cnrc.gc.ca

<sup>17</sup> Forest Ridge School of the Sacred Heart, 4800 139th Ave SE, Bellevue, WA 98006; martavbrown@yahoo.com

lar populations within a volume-limited sample of nearby galaxies. The survey provides complete and unbiased sampling of the local universe, thereby maximizing the legacy impact of the resulting data set, and enabling meaningful comparisons among galaxies in the sample and with cosmological simulations. Within this volume, ANGST adds more than a hundred orbits of new high-quality observations, and provides uniform reduction and photometry of both the new and archival observations. The resulting survey now offers superb targets for future multi-wavelength surveys, including the VLA-ANGST survey (Ott et al. 2008) and the Spitzer Local Volume Legacy Survey (LVL; Kennicutt et al. 2007), by allowing one to tie the multi-wavelength observations to the local star formation history revealed by ANGST.

In this paper we describe the survey design of ANGST, including the sample selection (§2), the observing strategy for new observations (tiling patterns, filter choices, exposure times, etc.) using both ACS (§3) and WFPC2 (§4), and the archival data employed by the survey (§5). We then present photometry for the survey galaxies for both ACS (§6) and WFPC2 (§7), tests of the photometric reliability (§8), astrometry (§9), and the resulting data products included in this data release (§10). In §11 we plot color-magnitude diagrams (CMDs) for all of the ANGST galaxies, and in §12 we measure colors and magnitudes for the tip of the red giant branch (TRGB), from which accurate relative distances are derived.

## 2. THE SAMPLE

### 2.1. Sample Selection

We drew the initial ANGST sample from the Karachentsev et al. (2004) Catalog of Neighboring Galaxies (CNG), updated with revised distances provided by I. Karachentsev. We restricted the catalog to galaxies beyond the zero velocity surface of the Local Group (van den Bergh 2000), due to the efficacy of ground-based observations within 2 Mpc and the large number of existing HST observations (e.g., Holtzman et al. 2006). We further restricted the sample to  $|b| > 20^\circ$ , to avoid sample incompleteness at low Galactic latitudes.

The choice of a maximum distance for the sample required balancing our scientific goals against constructing an observationally efficient program. At large distances, a wider variety of galaxy environments can be sampled, at the expense of larger photometric errors due to increased crowding and longer exposure times. We adopted an initial outer radius cut of 3.5 Mpc, within which deep CMDs could be derived with only modest exposure times. However, the Local Volume contains mostly field galaxies until reaching the massive M81 group at  $\sim 3.6$  Mpc and the Cen A group at  $\sim 3.7$  Mpc. Scientifically, the case for including at least one of these groups is strong. Without them, the limited range of environments sampled by a  $D \lesssim 3.5$  Mpc sphere would preclude studies of correlations between star formation history, galaxy morphology, and local environment. Of the two groups, the M81 group was judged to be the preferred target due to its high galactic latitude, low foreground extinction, and highly complete membership information. Galaxies in the M81 group were drawn from Karachentsev et al. (2002a), but do not include the newest candidate members reported in Chiboucas et al. (2008). We also in-

cluded a second high-density environment centered on the NGC 253 clump ( $D \approx 3.9$  Mpc) in the Sculptor filament (Karachentsev et al. 2003), further increasing the range of environments probed. The extensions into the M81 group and NGC 253 clump of the Sculptor group also improves coverage of luminous galaxies that are poorly represented in the  $D < 3.5$  Mpc volume.

The resulting sample of 69 galaxies is given in Table 1, along with the distances adopted during sample selection. Notable changes from the published version of the CNG include larger distances for UGC 8638, E059-01, and KKH60, which took them out of the sample, revised closer distances for NGC 4163 and DDO 183 which brought them into the sample, and elimination of HIJASS, which has no detectable stars. Distances for NGC 247, NGC 55, DDO 187, UGC 8833, HS117, and KKH37 were also revised according to new distances in Karachentsev (2005). Other data compiled in Table 1 includes absolute total magnitudes in  $B$ , morphological  $T$ -types, angular diameters ( $D_{25}$  for large galaxies,  $D_{26.5}$  for some dwarfs), and HI line widths ( $W_{50}$ ); all these quantities are listed as originally compiled in the CNG, and details can be found in Karachentsev et al. (2004). We also include apparent total  $K$ -band magnitudes from the literature when available; these are included for completeness only, and no attempt has been made to bring these to a common aperture with the  $B$ -band magnitudes from the CNG. Table 1 also indicates the original *planned* observational strategy for the sample galaxies; as we discuss below, not all observations were carried out as planned, due to the failure of ACS.

### 2.2. Properties of the Final Sample

The volume-limited sample defined above contains a rich assortment of galaxies. The range of distances, luminosities (in  $B$  and  $K$ ), and morphological types of the sample galaxies can be seen in Figure 1. Galaxy absolute magnitudes span from brighter than  $M_B = -20$  (M81 and NGC 253, the dominant galaxies in the M81 group and the Sculptor filament), down to fainter than  $M_B = -9$ , comparable to the Carina dwarf spheroidal in the Local Group.  $K$ -band total magnitudes were adopted from Jarrett et al. (2003) or Vaduvescu et al. (2005) when available, or inferred from  $B$  band magnitudes assuming  $B - K \sim 2.86$ , based on the estimates in Mannucci et al. (2001) for dwarf irregular spectral types.

As for any volume-limited sample, the distribution of luminosities is strongly weighted towards dwarf systems. Roughly 90% of the galaxies in the ANGST volume are fainter than the Large Magellanic Cloud (LMC), and 80% are fainter than the Small Magellanic Cloud. Integrating the luminosities of the galaxies, 99% of the  $B$ -band luminosity is contained in galaxies brighter than  $M_B = -13.7$  (33% by number). In the  $K$ -band, which presumably is a better tracer of the stellar mass, 99% of the luminosity is contained within only 17% of the galaxies ( $M_K < -17.5$ ). The large number of low luminosity systems is also reflected in the distribution of morphological types. Only 17% of the galaxies have morphological types characteristic of spirals ( $1 \leq T \leq 9$ ), while 58% are classified as dwarf irregulars and 25% as dwarf ellipticals. In spite of the large population of dwarf ellipticals, there are no massive early types in the sample. NGC 404 is classified as an S0, but has relatively low luminosity and

an extended gas disk (del Río et al. 2004). The earliest massive spiral in the sample is M81, with a morphological type of Sab.

The sample galaxies reside in diverse environments. There are at least 4 distinct groups with a range of richnesses – the dwarf dominated NGC 3109 group, two clumps in the Sculptor filament (one at NGC 55/NGC 300, and one at NGC 253/NGC 247), and the rich M81 group. Several of Tully et al. (2006)’s “dwarf groups” are also included in the ANGST survey volume (14+12, 14+13 14+07,14+08; the first two are the NGC 3109 and NGC 55/NGC 300 groups mentioned above). Group membership is also included in Table 1. Some of these groups can be seen in Figure 2, where we show the 3-dimensional distribution of the survey galaxies, using updated distances from §12 below<sup>18</sup>.

### 3. ACS OBSERVING STRATEGY

When designing an observing strategy for the ANGST sample, we balanced the limited number of orbits (295, down from an initial request of 555) against the goal of simultaneously recovering the star formation history (SFH) of the volume and establishing a general purpose imaging archive. We aimed to maximize uniformity, depth, and versatility, while making efficient use of the allocated orbits and the data already in the archive.

As part of this strategy, we chose to allocate a larger fraction of the orbits to the galaxies with the most stars, which contained either 99% of the stars, or 99% of the recently formed stars. These galaxies fall to the right of the vertical lines in the right and left hand panels of Figure 1.

The full radial extent of all galaxies was imaged in at least 2 filters. For dwarfs, these wide field tiles could be acquired in a single pointing. Larger, angularly extended galaxies were each imaged with a radial strip of overlapping ACS tiles extending from the galaxy’s center to its outskirts. In addition to the wide fields, deep fields with high completeness in the red clump were planned for the 12 galaxies that dominate the *K*-band luminosity of the ANGST volume; this depth provides strong constraints on the the ancient star formation history (e.g., Dolphin 2002). Another 16 galaxies within  $\sim 2.5$  Mpc would reach a comparable depth from their wide field tilings alone. In addition to the two filters in the standard wide field tilings, the 23 galaxies which dominate the recent star formation density (as assessed in the *B*-band) would be imaged in three filters, to permit extinction corrections and multi-wavelength source identification. Fourth, archival imaging of comparable depth to the new observations would be used when possible.

We now discuss the details of the wide-field tilings, the deep fields, the choice of filters, and the exposure times. In §4, we discuss how this strategy was modified after ACS failed during our program’s execution.

#### 3.1. Wide Field Tiling

The wide field tilings were designed for efficient multi-filter coverage of each galaxy’s radial extent. Thanks to ACS’s large field-of-view (FOV), dwarf galaxies could be imaged with a single pointing. For smaller dwarf galaxies, the galaxy center was aligned with the center of the

WFC1 chip to avoid the chip gap’s occluding the center of the galaxy. For the larger dwarf galaxies DDO 44 and DDO 82, the center was placed slightly above the chip gap. For galaxies whose radial extents were larger than could be imaged in a single pointing, we adopted a set of radial tiles extending from the center of the galaxy out to the position of the deep field, along the major axis in whichever direction required the smallest number of tiles. To allow flexible telescope scheduling, the tiles were allowed to be at any multiple of a  $90^\circ$  rotation from the major axis, with a  $\pm 5^\circ$  leeway. Adjacent tiles were overlapped by  $22''$  to allow complete coverage throughout the permitted range of telescope roll angles. All tiles were dithered to fill the chip gap and to remove cosmic rays and hot pixels. In the ANGST target naming scheme, tiles are numbered from the outermost tile inwards. The resulting field locations are shown superimposed on images from the Digitized Sky Survey in Figures 3-6, for both the ANGST observations and the archival observations described below (Table 2 & 3).

Among the galaxies eligible for a full radial strip, we did not image M81 or M82. The former had complete tiling through programs GO-10250 (*F814W* only) and GO-10584 (*F435W*, *F606W*, and some *F814W* in outer fields). M82 was tiled by STScI through program DD-10776 (Mutchler et al. 2007). Only the M81 photometry from GO-10584 is presented here; the *F814W* tiling in GO-10250 was not aligned in either pointing or rotation with the bluer observations in GO-10584, and thus requires capabilities not included in the current data processing pipeline.

#### 3.2. Deep Field Pointing

A single deep pointing was originally planned for each of the 12 galaxies which dominate the *K*-band luminosity (and presumably the stellar mass) of the local universe. The deep field exposure times were chosen to provide high completeness in the red clump region of the CMD, as described below. However, deep exposures are subject to significant stellar crowding, due to the increasing number of stars at fainter magnitudes in the CMD. When stellar fields become too crowded, longer exposure times no longer decrease the photometric errors or increase the number of detected stars. Instead, the photometric uncertainties are dominated by systematic errors produced by crowded, blended point-spread functions (PSFs). To avoid this situation, the deep fields needed to be placed in regions of the galaxies where photometric errors would not be dominated by crowding.

When placing the deep fields, we used the simulations of Olsen et al. (2003) to calculate the surface brightness below which photometric errors would be less than 0.1 mag in the red clump. This limiting surface brightness depends on distance, the underlying stellar population, and the pixel scale and PSF of the camera. We found typical ACS limiting surface brightness of  $\mu_V \sim 22.2 - 24.6$  mag arcsec<sup>-2</sup> for galaxies at  $D = 1.3 - 4$  Mpc. These limits yielded of order 100K stars per ACS FOV at our typical exposure time, which was consistent with our previous experience with an ACS snapshot survey (Seth et al. 2005b). The resulting limiting surface brightnesses were used to identify appropriate field locations for each of the target galaxies, us-

<sup>18</sup> These updated distances agree with the distances in Table 1 to 10% in almost all cases, as discussed in §12.

ing a combination of 2MASS, SDSS, and deep Malin (<http://www.aao.gov.au/images/>) images to estimate the local surface brightness along each galaxy’s major axis. The fields were allowed to have any orientation, and were contiguous with the outermost wide field tile.

### 3.3. Filter Choice

Imaging was carried out in three filters for the galaxies that dominate the recent star formation in the local volume (i.e., to the right of the line in the left panel of Figure 1), and two filters for all others. For the galaxies with 3 filter coverage, we used  $F475W + F606W + F814W$ , which maximized the combination of wavelength coverage and throughput. The three filters are useful for identifying X-ray counterparts, HII region nebulousity, and extinction (when combined with future UV or NIR imaging). Although the  $F435W$  filter allows for a larger wavelength baseline and disjoint wavelength coverage with  $F606W$ , its throughput is much less than that of  $F475W$ .

For the dwarf galaxies with 2 filter coverage, we used a  $F475W + F814W$  filter combination, instead of the more commonly used  $F606W + F814W$ . Although  $F475W$  does not reach as far down the CMD as  $F606W$  for a given exposure time, it provides greater temperature sensitivity due to the longer wavelength baseline of the  $F475W - F814W$  color combination. For regions above the red clump, more scientific information can be extracted from better temperature sensitivity than from the slight gain in depth possible with  $F606W + F814W$ . This choice allowed us to better separate main sequence stars from the blue helium burning sequence, and to derive stronger constraints on the metallicity distribution of red giant branch (RGB) stars. This effect can be seen in Figures 9-22, when comparing CMDs in  $F475W + F814W$  and  $F606W + F814W$  for galaxies with 3-filter observations (such as DDO 190). Given the very low extinctions expected in low metallicity systems, a third filter was not deemed necessary for the faintest dwarf galaxies. For many of these, some  $F606W$  imaging is already available in the archive, largely from the SNAP-9771 and SNAP-10210 programs.

For the deep fields, the scientific demand of constraining ancient star formation requires the highest possible completeness in the red clump. Thus, the majority of time invested in deep fields was in the more traditional  $F606W + F814W$  color combination, which maximizes the depth along the RGB at the expense of lower color sensitivity. A single orbit of  $F475W$  was also included for continuity with the wide-field observing strategy, and to allow the possibility for extinction mapping in the future.

### 3.4. Exposure Times

Exposure times were chosen to achieve two separate goals. For the wide fields, the goal was efficient, multi-color imaging of the upper regions of the CMD, allowing good constraints on the occupation of the main sequence, the luminosity function of the blue and red helium burning sequences, the color distribution of the RGB, and the population of AGB stars. For the deep field, the goal was high completeness and photometric accuracy in the red clump. We discuss the details of the wide field and deep field observations in §3.4.1 and §3.4.2 below. A listing

of the new observations taken for this program can be found in Table 2.

#### 3.4.1. Wide Fields

The wide field observing strategy was shaped by the need to get up to 3 filters at each tile position. In each filter we need at least a 2- or 3-point dither pattern to reject cosmic rays and to cover the chip gap. Due to data volume constraints, two orbits are required to get at least 2 images in each of the three filters. For crowded areas, we used the minimum 2 orbits for the wide-field tilings, while in the outermost wide fields, where crowding was not a limiting factor on the photometry, we used 3 orbits, 1 orbit per filter. For dwarf galaxies, we devoted one orbit to each of the 2 filters. Total exposure times can be found in Table 2. The typical photometric depths ( $S/N=5$ ) were 28.4 in  $F475W$  and  $F606W$ , and 27.5 in  $F814W$  for a single orbit.

#### 3.4.2. Deep Fields

The goal of the ANGST deep fields is to obtain an accurate census on the number, magnitude and color of stars in the red clump. These stars place a strong constraint on the ancient SFH enabling the possibility of breaking the age-metallicity degeneracy present along the upper RGB. We requested deep fields for 12 galaxies in the ANGST volume with  $M_K < -17.5$ . These 12 galaxies contain 99% of the K-band luminosity within our survey volume, and thus have dominated the past total SFH. The significant time investment required to obtain CMDs reaching below the red clump meant that these exposures were limited to a single field in each galaxy.

Exposure times were chosen to obtain  $S/N \gtrsim 10$  in both  $F606W$  and  $F814W$  for stars in the red clump. In practice, we achieved this by using the ACS Imaging Exposure Time Calculator to estimate the time necessary to reach  $S/N=3.5$  for a G0III star normalized to  $M_V = +1.5$  (for  $F606W$ ) and  $M_I = +0.7$  (for  $F814W$ ), a magnitude below the theoretical red clump for a  $[Fe/H]=-1.3$ , 10 Gyr population in the Padova isochrones (<http://pleiadi.pd.astro.it/>). To calculate the appropriate red clump magnitude for each galaxy, reddening and extinctions were adopted from Schlegel et al. (1998), and distance moduli were chosen by carefully evaluating data from the literature (Karachentsev et al. 2002a, 2003; Rekola et al. 2005; Mouhcine et al. 2005; Sakai & Madore 2001; Karachentsev et al. 2006; Freedman et al. 1994; Sakai & Madore 1999; Tikhonov et al. 2003; Maíz-Apellániz et al. 2002; Drozdovsky et al. 2002; Gieren et al. 2004, 2005; Rizzi et al. 2006; Minniti et al. 1999; Méndez et al. 2002; Aparicio & Tikhonov 2000) and from our own TRGB measurements using archival data. Exposure times were turned into orbit estimates using the appropriate overheads and available visibility times depending on the declination of the source. For the two deep exposures of M81 and NGC 2976 that were obtained with ACS before its failure, a single long exposure ( $\sim 2700$  sec) was taken in each orbit. Each visit contained an orbit in each filter both to maximize our baseline for variable stars and to minimize the risk of obtaining incomplete filter coverage in the event of spacecraft failure. A short 100s exposure was taken to permit photometry of the brighter stars saturated in



the full orbit exposures, and a full orbit of *F475W* data was included for consistency with the wide fields and to enable the possibility of internal reddening estimations.

### 3.5. *Parallels*

WFPC2 observations were taken in parallel with the ACS observations in Table 2. These observations were divided evenly between *F606W* and *F814W*, and are 6' away from the center of the ACS FOV. Photometry of these fields will be reduced with the WFPC2 pipeline described below in §7, but is not included in this initial data release.

## 4. WFPC2 OBSERVING STRATEGY

ACS observations for our program began in early September 2006. Unfortunately, the wide field camera on ACS failed in late January 2007, ~5 months into the execution of our program. As a result, we lost 147 orbits on the massive galaxies with deep fields ( $M_K < -17.5$ ; 71% lost), and lost 44 orbits on the fainter galaxies (50% lost), for a total of 191 orbits lost from the original allocation of 295 orbits. Of the 195 orbits that were to be devoted to the deep fields, we received 41 orbits (79% lost), primarily for NGC 2976 and M81. Given the uncertainties in the upcoming HST servicing mission, we decided to continue the program with WFPC2.

Following an appeal, the Telescope Time Review Board restored 116 of the 191 lost orbits to execute deep single-pointing observations for the nearest luminous galaxies and the very closest dwarfs (NGC 55, NGC 4214, NGC 404, NGC 2403, NGC 3109, Sex B, and IC 5152). Time for wide field observations was not granted. For the majority of these galaxies, sufficient data exist in the archive for tying the large radius deep fields to the SFH of the galaxy as a whole, although with a lack of complete radial coverage and uniformity. However, NGC 55 and NGC 3109 did not have adequate radial coverage due to their large angular extents. Through a Director's Discretionary request (DD-11307), we were awarded an additional 25 orbits to execute radial tilings for these two remaining galaxies (5 pointings per galaxy, with 2 orbits per tile for NGC 3109 and 3 orbits per tile for NGC 55).

### 4.1. *WFPC2 Deep Fields*

Transferring the ANGST deep field observing strategy to WFPC2 required a number of modifications. The first significant change was in field placement. The wide-field chips of WFPC2 are undersampled compared to ACS, leading to larger photometric errors due to crowding at comparable surface brightnesses and exposure times. We therefore had to move the deep fields to even lower surface brightnesses (and thus larger radii) than the original ACS deep field locations. Using the Olsen et al. (2003) simulations, we recalculated the surface brightness limit at which our observations would become crowding limited. These revised limits were ~1.5 mag fainter than for ACS. These changes required shifting the fields typically another ~1.4 disk scale lengths further out, increasing the risk that the WFPC2 FOV would fall beyond any significant disk truncation, if present. This appears to have happened for IC 5152, but did not affect any of the other observations.

The second adaptation was to accept slightly less photometric depth. WFPC2's throughput is substantially

worse than ACS's, and thus matching the depth of the ACS deep fields would require a prohibitive number of orbits. However, our experience with the ACS deep fields for M81 and NGC 2976 suggested that we could reach our scientific goals with slightly shallower data, and thus we revised our target depth to a SNR of 3 at 1.5 magnitudes below the middle of the red clump. The final change to the program was to eliminate the *F475W* observations, where WFPC2's sensitivity is particularly poor.

When allocating orbits, we maximized the photometric accuracy in the red clump (where  $F606W - F814W \approx 0.75$ ) by allocating twice as many orbits to *F814W* than to *F606W*. A random-walk dither pattern was adopted and full-orbit exposures were used; the number (>5) of exposures made cosmic-ray rejection straightforward without the need to CR-split the exposures during the orbit, allowing us to obtain the maximum depth possible with each orbit.

The resulting images typically had between 5000 and 15000 stars per WFPC2 chip. We checked our photometry on a chip-by-chip basis to identify potential problems or offsets due to the well-known WF4 bias anomaly. Images of WF4 showed no obvious problems with the bias, nor was the photometry noticeably worse, suggesting that the anomaly had been properly addressed by STScI's WFPC2 data reduction pipeline and/or that the chip was performing well at the time the observations were performed. We therefore are including WF4 data in the released photometric catalogs. These catalogs include a flag identifying the chip that a star fell on in the reference image, allowing the user to filter out WF4 data, if needed.

### 4.2. *WFPC2 Wide Field Tilings*

For the WFPC2 wide field tilings of NGC 55 and NGC 3109, we aimed to match the depth (in absolute magnitude) of the wide radial tiles in the more distant systems of the ANGST survey, assuring that the WFPC2 tiles were at least as deep as the shallowest wide field tiles in the survey. This depth corresponds to a signal-to-noise of 5 and 50% completeness at  $M_{F814W} = -0.5$  for the colors of the RGB. At the distances of NGC 3109 (1.3 Mpc;  $m_{lim, F814W} = 25.1$ ) and NGC 55 (2.1 Mpc;  $m_{lim, F814W} = 25.8$ ), we could reach this depth and completeness in 2 orbits for NGC 3109 and 3 orbits for NGC 55, including overheads for CR-SPLITS and guide-star acquisition, based on comparable 2-orbit observations for Sextans A (Dohm-Palmer et al. 1997) and WFPC2 parallel data from the main ANGST ACS observations.

To produce a radial strip, we adopted a "Groth strip" tiling strategy of interleaved chips, with an orientation set to maximize schedulability for each target. Unlike the original ANGST ACS program, we did not tile all the way out to the deep fields, which had to be moved even further out to cope with WFPC2's lower resolution. We instead stopped the radial tiling where we are sure that we have imaged most of the recent star formation. To conserve orbits, tiles were placed on whichever side of the galaxy presented the smallest distance to the edge of the star-forming disk.

## 5. ARCHIVAL DATA

The original ANGST survey strategy was designed to take advantage of archival data whenever it matched or surpassed the quality of the proposed observations, in comparable filters. The failure of ACS during execution of the ANGST program further increased our reliance on archival data. In Table 3 we summarize the archival data sets that are incorporated into the ANGST data release, along with papers that have published CMDs from these data independently. We have excluded data sets that have only one filter at a single position, or that have severe offsets or misalignments among multiple filters. Photometry in the latter cases is significantly compromised by the distortion of the ACS WFC, and cannot be readily produced by the ANGST pipeline. In future data releases, we will incorporate such data as needed, most notably for the *F814W* tilings of M81 by GO-10250.

## 6. ACS PHOTOMETRY

Photometry was carried out on bias subtracted, flat-fielded `*flt` images (or `*crj` images when available) produced by the STScI ACS pipeline OPUS versions 2006.5 through 2008.1, which used CALACS version 4.6.1. through 4.6.4. For `*crj` images, the value of the readnoise reported in the CALACS header did not reflect that the final image contains two co-added readouts. In these cases, we multiplied the read noise listed in the header by  $\sqrt{2}$ , so that it properly accounted for the combined read noise of the co-added CR-SPLIT observations. Failure to make this correction would have produced systematic errors in the reported photometric errors.

To measure stellar photometry, we used the software package DOLPHOT<sup>19</sup> (Dolphin et al. 2002) including the ACS module. This package is optimized for measuring photometry of stars on dithered ACS images, where the position angle of the multiple exposures are the same, and the shifts between exposures are small ( $\lesssim 30''$ ). To align images, DOLPHOT makes a fast initial pass through the data to find bright stars common to all of the frames, using approximate shifts supplied by the user. The final shifts between the images are then determined based on these stars. By this method, our exposures were able to be aligned to  $\sim 0.01''$  precision. The precision is slightly worse ( $\sim 0.015''$ ) for fields with small numbers of stars, and slightly better ( $\sim 0.005''$ ) for more crowded fields. When aligning images, we currently do not incorporate time-dependent corrections to the geometric distortion. While improved distortion corrections would help improve the astrometric solution for the frames, it has only a second-order effect on our photometry, since the photometric accuracy depends primarily on multiple images being aligned correctly relative to each other, rather than relative to an undistorted frame. As we currently are only analyzing stacks of images with small positional shifts, taken close together in time, temporal drifts in the geometric distortion are not a limiting factor in our photometry. They will, however, be considered in future releases.

Although DOLPHOT operates on non-drizzled images, we also combined all images into a single drizzled image using the `multidrizzle` task within PyRAF (Koekemoer et al. 2002), which allowed us to flag the

cosmic rays in the individual images. Once the cosmic rays were identified, the photometry was measured for all of the objects using the individual, uncombined frames.

To calculate the flux of each star, DOLPHOT initially adopts the point spread function (PSF) calculated by Tiny Tim (Krist 1995), and scales the PSF in flux to minimize residuals throughout the image stack. The shape and width of the Tiny Tim PSF has been shown to match to the shape of the true PSF well throughout both ACS chips, based on the extensive analysis presented by Jee et al. (2007). There are slight deviations close to the bottom of Chip 1, but our tests in §8 find that these do not lead to noticeable systematics in the magnitude errors. DOLPHOT makes additional minor adjustments to the Tiny Tim PSF by using the brightest and most isolated stars to correct for PSF changes due to temperature variations of the telescope during orbit. These adjustments typically affect the photometry at the 0.01 magnitude level.

DOLPHOT also uses the most isolated stars in the field to determine aperture corrections to the PSF magnitudes, which accounts for any systematic differences between the model and true PSF. These corrections were generally  $\lesssim 0.05$  mag for a given exposure. DOLPHOT then applies the aperture corrections for each exposure, corrects for the charge transfer efficiency of the ACS detector using the coefficients given in the ACS-ISR 2004-006<sup>20</sup>, combines the results from the individual exposures, and converts the measured count rates to the VEGAMAG system (a system where Vega is defined to have mag=0 in all filters) using the Sirianni et al. (2005) zero points for each filter. Note that the Sirianni et al. (2005) zero points have since been updated in ACS-ISR 2007-02 to reflect the change in sensitivity due to the increase in ACS’s operating temperature in July 2006 after the switch to Side 2 electronics; these changes are of order  $\sim 0.015$  mag, and have been propagated into the relevant photometric catalogs covered in this release. The resulting zero points match those in Table 5 of ACS-ISR 2007-02. We have not yet propagated zero point changes due to improvements in the calibration of the system throughput (ACS-ISR 2007-06); these changes seem to be of the order of less than 0.01 in the filters covered in this data release, but still have significant unresolved uncertainties in the red wavelength regimes that dominate much of the ANGST catalogs.

DOLPHOT makes use of all exposures of a field when measuring stellar properties. This technique results in a single raw photometry output file for each field that contains measured properties of all objects detected in the field, including the position, object type (point source, extended, elongated, or indeterminate), combined magnitude, magnitude error, signal-to-noise, sharpness, roundness,  $\chi^2$  fit to the PSF, crowding, and error flag (chip edge or saturated) in all filters. The output catalog contains these measurements for each star in each individual exposure as well, providing the opportunity for variability studies.

We spent significant time investigating optimal values

<sup>19</sup> <http://purcell.as.arizona.edu/dolphot>

<sup>20</sup> Preliminary versions of revised ACS charge transfer efficiency (CTE) corrections have recently been released on STScI’s web site, but were announced after all the data had been processed for this release. These corrections will be used in subsequent releases, and updated on the data release website.

for the dozens of parameters that can be adjusted in DOLPHOT to maximize the quality of the photometry measured from the data. Three of the parameters which had the strongest influence on our resulting photometry were the **Force1** parameter, the aperture radius (**RAper**), and the sky fitting parameter (**FitSky**).

The **Force1** parameter forces all sources detected to be fitted as stars, assuming that separate culling will be performed on the output file to discard non-point sources. For our crowded fields, this option was optimal, but required that special care be taken in fitting the sky. We found that with **FitSky** set to 1 (fit the sky in an annulus around each star), our photometry was much more heavily affected by crowding, resulting in large crowding errors for nearly all of the stars in our wide field data. With **FitSky**= 2 (fit the sky inside the PSF radius but outside the photometry aperture), we needed a small aperture radius (4 pixels), and found systematic errors ( $\sim 0.02$  mag) in the recovered magnitudes of artificial stars added to the data, using bright stars whose random photometric uncertainties did not overwhelm the systematic error. We found that setting **FitSky**= 3 (fit the sky within the photometry aperture as a 2-parameter PSF fit) allowed a larger photometry radius (10 pixels) with smaller aperture correction, and provided photometry with the smallest crowding errors and no significant systematic errors. Note that in all these methods DOLPHOT subtracts the flux of neighboring stars before measuring the sky and stellar flux; differences in the operation of **FitSky** therefore change the way residuals propagate, but not the total flux of nearby stars.

We provide full photometry output for each field along with culled catalogs containing the highest quality photometry. We culled the raw DOLPHOT output in two ways, releasing both a complete and a conservative (but very high quality) catalog for each field. The complete catalog contains all sources that were not flagged by DOLPHOT as extended, elongated, extremely sharp, highly saturated, significantly cut off by the edge of the chip, or not detected at high signal-to-noise (4.0 or higher in at least 2 filters).

In addition to the complete catalog, we also provide a more conservative catalog of stellar photometry which has been culled to remove highly uncertain photometry. These catalogs have been filtered to only allow objects with low sharpness ( $(\text{sharp}_1 + \text{sharp}_2)^2 \leq 0.075$ ) and crowding ( $(\text{crowd}_1 + \text{crowd}_2) \leq 0.1$ ) in both filters. The sharpness parameter cut removes extended objects such as background galaxies missed by the earlier cuts. The crowding parameter gives the difference between the magnitude of a star measured before and after subtracting the neighboring stars in the image. When this value is large, it suggests that the star's photometry was significantly affected by crowding effects, and we therefore exclude it from our most conservative catalogs. Quality cuts based on the  $\chi^2$  values were also considered, but they were rejected when a correlation was found between  $\chi^2$  and the local background.

We found that these final cuts produce CMDs with well-defined features in the uncrowded field, while retaining most of the stars in high surface brightness regions. However, the cuts in the more conservative catalog may remove stars from certain interesting regions, like stellar clusters. We advise anyone interested in studying clus-

ters or identifying stellar counterparts for specific sources to check the effects of the different parameter cuts. In Gogarten et al. (2008), we found that relaxing the crowding parameter cuts to  $\text{crowd}_1 + \text{crowd}_2 \leq 0.6$  recovered a number of stars in clusters without dramatically compromising the quality of the photometry.

Our final catalogs include stars that may contain some saturated pixels, as long as the saturation was not so bad that the PSF could not be reliably fitted. Saturation limits our wide field photometry to magnitudes fainter than  $\sim 18$  and our deep field photometry to magnitudes fainter than  $\sim 20$ . In Table 4 we give the level of 50% photometric completeness for each observation, as determined from initial artificial star tests. These completeness limits are for the field as a whole, but can be expected to vary spatially within a field due to spatial variations in the degree of crowding.

While these cuts do an excellent job of restricting the catalogs to stellar sources, we have noted occasional limits to star-galaxy separation near the photometric limits of the data, and spurious “stellar” sources in the diffraction spikes of extremely bright stars. If these issues are of critical importance for a particular scientific project, we recommend additional culling using information from galaxy-specific photometry packages such as SExtractor (Bertin & Arnouts 1996) to mask out possible sources of contamination.

We also note that star-galaxy separation is frequently impossible for sources near the photometric limit, even in high-resolution HST data. Some fraction of the faintest sources in the photometric catalogs are therefore likely to be unresolved background galaxies. We do not think that these sources are a significant issue for most analyses, however, since they represent a negligible fraction of the sources in the main body of most galaxies. To quantify this, we can use the WFPC2 field for IC5152. This field has a completeness limit of 26.45 magnitudes in *F814W* and contains 325 objects in the cleaned \*.gst catalog (described below), over an area of 5.65 square arcminutes. The field unfortunately fell beyond the radius where IC5152's disk truncates, and thus the majority of the 325 objects are likely to be either foreground MW stars or unresolved background galaxies. We can then take 57.5 stars per square arcminute to be the upper limit for the contamination in observations of this depth.

We can scale the IC5152 data to other completeness limits, using the observed galaxy number counts given in Figure 3b of Windhorst et al. (2008). Over the range of depths for the ANGST data, the slope in the galaxy number counts scales as  $\log_{10}(N_1/N_2) \approx 0.32(m_{lim,1} - m_{lim,2})$ . We have applied this scaling relation to the data in Table 4 to calculate the upper limit on the fraction of sources that could potentially be contaminants in each field. After IC5152 itself (which has 100% contamination by definition), the next highest contamination fraction is 35% for an outer halo field of M81 (NGC3031-HALO-2), which lies well beyond the main body of the galaxy. All other contamination fractions are less than 23%, and 90% have maximum contamination fractions of less than 10%. Given that most ANGST targets take up less than one third of the total chip area, the contribution of unresolved galaxies to the CMD is likely to be less than 3% within the galaxy radius in almost all cases.

## 7. WFPC2 PHOTOMETRY

After the failure of ACS and the transfer of our program to WFPC2, we adopted the WFPC2 pipeline previously used by Holtzman et al. (2006) for their archival study of Local Group dwarfs. We briefly summarize the key features of the pipeline here, but refer the interested reader to the more extensive documentation in Holtzman et al. (2006).

The Holtzman et al. (2006) pipeline operates on images processed with the standard STScI baseline processing. Photometry is performed using HSTphot (Dolphin 2000), a predecessor of DOLPHOT that is optimized for WFPC2 images. HSTphot shares DOLPHOT’s basic strategy of using Tiny Tim PSFs supplemented with image-based aperture corrections to derive photometry from unstacked images that have not been distortion corrected or drizzled. HSTphot adopts the photometric calibration given in Holtzman et al. (1995), updated with improved calibrations from [http://purcell.as.arizona.edu/wfpc2\\_calib/](http://purcell.as.arizona.edu/wfpc2_calib/). Note that the WFPC2 photometric system is defined such that Vega has a magnitude in each WFPC2 filter corresponding to Vega’s magnitude in the nearest UBVRI filter; the different definition of the zeropoints in the WFPC2 and ACS photometric systems leads to offsets of 0.02–0.04 mag between the calibrated magnitudes of the two instruments (see §8.2 below).

The only significant difference from the Holtzman et al. (2006) pipeline is that the current version of HSTphot uses the latest (July 2008) CTE corrections derived by A. Dolphin ([http://purcell.as.arizona.edu/wfpc2\\_calib/](http://purcell.as.arizona.edu/wfpc2_calib/)). Compared to the Dolphin et al. (2002) prescription, the new CTE calibration no longer assumes that background and stellar brightness factors are independent, leading to somewhat fainter WFPC2 magnitudes than previous calibrations, and many fewer systemic offsets in the residuals. Using a typical ANGST wide field observation as a baseline, the switch to the new CTE correction changes the CTE correction for a  $V = 22$  magnitude star from 0.052 mag to 0.115 mag in  $F606W$  and from 0.067 mag to 0.123 mag in  $F814W$ , for a background sky level of  $\sim 100$  cts/pixel in both filters. For a fainter  $V = 28$  magnitude star, the CTE changes from 0.328 mag to 0.214 mag in  $F606W$  and from 0.438 mag to 0.238 mag in  $F814W$ . The much lower level of residuals in the new CTE calibration suggests accuracy in the bright end of 0.01 – 0.02 magnitudes. At the fainter end, it is much more difficult to assess any systematic offsets, as they are much smaller than the photometric uncertainties.

After processing by the Holtzman et al. (2006) pipeline, we integrate the photometry into the database shared by the main ACS pipeline. Slight differences in the WFPC2 and ACS keywords used the released data tables are described below in §10.

## 8. PHOTOMETRIC TESTS

The photometric pipeline produces catalogs of multi-filter photometry and estimates of the photometric uncertainty for each measurement. These uncertainties include Poisson flux errors, uncertainties in the sky determination, and uncertainties in the subtraction of neighboring objects. They do not include systematic errors

due to spatial and temporal variation of the point spread function (i.e., Jee et al. (2007); Rhodes et al. (2006), ACS ISR 07-12, ACS-ISR 06-01), in the absolute calibration of the photometric system, and in the accuracy of the adopted CTE corrections (which were in flux at the time that this data was released). To assess the degree of systematic errors, and the accuracy of the reported uncertainties, we have performed a series of consistency checks to measure shifts in the photometry of individual stars measured multiple times, in different portions of the field of view, and for different instruments. All tests use the conservative photometric catalogs, to allow the greatest sensitivity to systematic errors.

### 8.1. Repeated ACS Measurements

We first analyze the magnitude difference between stars measured in two individual single-orbit  $F814W$  ACS exposures from the M81 deep field. The exposures were taken during a single visit, which minimizes any temporal changes in the PSF. The exposures also had only modest (0.1–0.2”) dithers between them, allowing us to minimize systematic errors in modeling the spatial variations in the PSF. Crowding errors should likewise be minimal, given the low stellar density within the field. This test case therefore offers the “best case scenario” for agreement between repeated measurements, and sets a lower bound to our expected error distribution in less than optimal cases.

To measure magnitude differences closer to the “worst case scenario” for ACS, we also analyze repeated measurements of stars that fall in the overlap region in the wide field tiling of NGC 300, between WIDE1 and WIDE2. These stars lie in the most highly distorted regions of the ACS chip, and have close to the maximum possible offset in their locations on the chips between the two images, making them a highly sensitive test of the uncertainties produced by errors in the point-spread function that DOLPHOT adopts from Tiny Tim. The images were also taken two days apart in separate visits, making them somewhat sensitive to temporal changes in the PSF as well. However, as there was little change in the Y-position of the stars, this comparison has no sensitivity to systematic errors produced by CTE.

Finally, we measure the magnitude differences between the measured and the “true” magnitudes of artificial stars, added to the same overlap region analyzed above for NGC 300. In this case, the stars are recovered with a PSF that is identical to that used for generating the artificial stars. This case therefore minimizes effects due to PSF uncertainty. However, it remains sensitive to errors due to Poisson variations in the flux and the sky background, and due to contamination from nearby stars. Note that the error distributions are expected to be different from the previous two tests, which probed magnitude differences between repeated measurements of stars with identical crowding and sky backgrounds, not the magnitude differences from truth.

In Figure 7, we plot the cumulative distribution of magnitude differences between repeated measurements of individual stars, scaled by the quadrature sum of the uncertainties reported in the individual measurements (i.e.,  $\Delta m / \sigma_m$ , where  $\Delta m \equiv m_1 - m_2$  and  $\sigma_m^2 = \sigma_{m1}^2 + \sigma_{m2}^2$  and  $m_1$  and  $m_2$  refer to the measurements of a single star in two different images). The distributions are generated

for all stars in a limited magnitude range, in steps of 1 magnitude, with fainter bins plotted with darker lines. The distributions for brighter stars have insufficient numbers of stars to be reliable, and are not plotted. In red, we plot the distribution of scaled magnitude differences that would be expected if the magnitude differences were distributed as a Gaussian with width  $\sigma_m$ . The left panel contains only stars in the overlap region ( $\sim 600$  pixels wide), and the right panel contains stars for the whole frame.

The distributions of magnitude differences between repeated measurements show a number of features. First, even in the worst case scenario of large positional shifts, the magnitude differences are essentially unbiased. The median magnitude difference is less than 5% of the reported uncertainty in all cases, such that repeated measurements of given isochrone features will converge on the same magnitude, even when observed with different parts of chip, or with multiple exposures. There is a slight tendency, however, for the bias to be somewhat larger when large positional shifts are present, particularly for the brighter stars. This indicates that there are indeed small systematic errors in the assumed PSF that are more noticeable when the wings of the PSF are well-exposed. However, these biases will be swamped by the intrinsic random and crowding errors, as well as Poisson uncertainties, and thus can safely be neglected in almost all practical applications.

The second feature of the distributions is their tendency to be wider than a Gaussian whose width is set by the reported uncertainties. The true distributions are broader and more flat-topped than expected. This leads to larger numbers of stars at a given magnitude difference than one would predict for a perfect Gaussian error distribution. This difference is most pronounced for the brightest stars. However, even the largest shifts do not produce measurable tails beyond  $5\sigma_m$ , so while the shape of the error distribution differs from a Gaussian, we do not detect more than 1-2 stars with  $\Delta m > 5\sigma_m$  in our analysis regions.

We can get clues to the origin of the increased width by noting that the discrepancy from a Gaussian is larger for brighter stars, for which the distribution becomes closer to a uniform “top hat”. We believe that a significant fraction of this broadening is actually due to the limited precision of the errors and magnitudes reported by DOLPHOT. Catalog values of  $\Delta m$  and  $\sigma_m$  are quantized at the 0.001 mag level, rather than being true continuous variables. This quantization has the largest impact on the distribution of  $\Delta m/\sigma_m$  when errors and magnitude differences are close to the level of quantization, as they are for the brightest stars. Not until the faintest magnitude bins do the errors approach the distribution expected for a continuous variable.

In Figure 8 we show the distribution of magnitude differences between the true and the measured magnitudes ( $\Delta m \equiv m_{\text{true}} - m_{\text{measured}}$ , and  $\sigma_m \equiv \sigma_{m,\text{measured}}$ ) of artificial stars added to and recovered from the images, for a series of magnitude bins. These distributions are quite different than the distributions for repeated measurements, as would be expected. First, the distributions are highly skewed, producing a large tail towards measured magnitudes that are brighter than the true magnitude. This skewing results when artificial stars land

on or near a star that would otherwise be undetected. The flux from the previously undetected star adds to the artificial star, biasing the measured flux upwards. Such a bias would not be apparent in a repeated measurement, as both measurements would share the same bias. The skewing is most severe for the faintest stars, where the additional flux from undetected stars produces the largest fractional change in the detected flux. Moreover, the sample of faint recovered stars will be biased towards stars with heavily contaminated fluxes, given that such stars are preferentially detected; this effect is reduced for brighter stars, which are detectable whether or not an undetected companion falls within the PSF.

The second feature apparent in the comparison between true and measured magnitudes is that the distributions are systematically broader than a Gaussian with a standard deviation equal to the magnitude uncertainty reported for the measured star. This deviation is not surprising, given that the uncertainties are not due solely to Poisson counting statistics, and are thus unlikely to have distributions that approach a perfect Gaussian.

## 8.2. WFPC2-ACS Comparison

Due to the failure of ACS, we are releasing photometry both from WFPC2 and ACS. Differences between these two photometric systems are expected due to different instrumental responses, CTE corrections, and absolute photometric calibrations between the two photometric systems. We have made an initial assessment of the degree of possible systematic offsets using observations of the dwarf elliptical DDO 44, which was observed with WFPC2 (GO-8137) in January of 2001, and with ACS as part of ANGST in September of 2006. Both data sets were processed with the respective WFPC2 and ACS pipelines described above. Stars were automatically matched between the two catalogs using the closest positional match in right ascension and declination, after solving for shifts and rotation between the two fields. We consider only pairs of stars that agreed in magnitude to within  $10\sigma_m$ , where  $\sigma_m$  is the magnitude error from the quadrature sum of the error in each pair of stars; this procedure produced good matches for  $\gtrsim 90\%$  of the overlapping stars, though there are clearly occasional spurious matches as well. The resulting matched catalog was restricted further to include only stars above the approximate completeness limit of each data set ( $m_{F814W}$  brighter than 26.0 and 26.1 for the WFPC2 and ACS data sets, respectively). Comparisons were made in the F814W filter, which is the only overlapping filter between the two sets of observations.

Before comparing  $m_{F814W,WFPC2}$  to  $m_{F814W,ACS}$ , we need to account for the different zeropoint definitions in the ACS and WFPC2 photometric systems. Both systems are relative to Vega, but the ACS system defines Vega to have 0 magnitude in all ACS filters, while the WFPC2 system defines Vega to have a magnitude corresponding to Vega’s magnitude in the nearest UBVRI filter. For F814W, Vega has  $m_{F814W,WFPC2} = 0.035$ . As a result, 0.035 mag must be added to the ACS F814W photometry to compare the results on the same system<sup>21</sup>. The systems will also differ for stars of a different color than Vega to the extent that the system response

<sup>21</sup> Note that the Bedin et al. (2005) ACS calibration also as-

of the ACS F814W filter+camera+detector system differs from that of WFPC2.

We examined the resulting magnitude differences as a function of magnitude, color, and Y-position on the chip. At almost all magnitude levels, the systematic errors are dominated by the random errors in the photometry (which themselves are dominated by Poisson counting variations and residual flux from crowding). However, we do detect residual systematic errors at the few percent level, which vary steadily with Y on either instrument, indicating low level problems with the adopted CTE corrections in both WFPC2 and ACS. Updated CTE corrections for ACS are in progress at STScI, but these corrections were not ready in time for reducing the data for this release. Given that these corrections are typically swamped by random errors and are smaller than current uncertainties in the stellar isochrones that are used to interpret the CMDs, we decided to release the data as is. Subsequent releases will include the new CTE corrections as they become available. We also detected possible signs of a color-dependence in the magnitude differences between the WFPC2 and ACS F814W VEGAMAGS, which appear to be larger than expected based on synthetic filter curves. A definitive diagnosis of this dependence must wait until the improved CTE corrections for ACS are implemented, but should the effect persist, then there may be an additional few percent uncertainty in the instrumental response of either WFPC2 or ACS or both.

## 9. ASTROMETRY

Astrometry for the photometric catalogs was initially taken from the FITS headers of the original HST images, which have astrometry that is accurate to  $1 - 2''$ . Recently, the Hubble Legacy Archive (HLA) improved on the default astrometry using the Guide Star Catalog (GSC), the Sloan Digital Sky Survey (SDSS), and the Two Micron All Sky Survey (2MASS). The revised astrometric solutions have a typical RMS of  $0.1 - 0.3''$  in most cases. There are many cases in our data set where the RMS is much larger, due to using faint (or non-existent) sources in the GSC, or cosmic rays in the image during matching. In these cases, new astrometric positions will have to be derived by hand. Because this process is almost always limited by the lack of astrometric standards within nearby galaxies, in many cases  $1 - 2''$  uncertainties remain, and will have to be dealt with in future releases by using a system of secondary astrometric standards defined in wide-field ground-based imaging.

Relative photometry within a given field is usually accurate to a fraction of a pixel, and the absolute position is good to a few pixels in most cases. However, in applications requiring sub-arcsecond accuracy of the absolute astrometric position (e.g., such as slit masks or comparisons with multi-wavelength data), users should consider making an independent astrometric solution. We will continue to release improved astrometric solutions

sumes that  $m_{F814W,WFPC2} = 0.0$  (giving  $m_{zp,F814W,ACS} = 25.492$ ), so comparisons with this alternate calibration also require adding an  $+0.035$  offset; this correction was not made during the WFPC2-ACS comparison in Saviane et al. (2008), and thus their apparent agreement of  $m_{F814W,WFPC2} - m_{F814W,ACS} = 0.003 \pm 0.005$  actually implies that  $m_{F814W,WFPC2} - m_{F814W,ACS} = 0.038 \pm 0.005$  over the magnitude and color range of  $26 < m_{F814W,ACS} < 27.5$  and  $0 < m_{F606W,ACS} - m_{F814W,ACS} < 2$ .

as they become available, including time-dependent geometric distortion corrections as well.

## 10. DATA PRODUCTS

Binary FITS tables of photometry for the ANGST sample have been released through the Multimission Archive at STScI (MAST: <http://archive.stsci.edu/prepds/angst/>), and can also be accessed interactively through the project website (<http://www.nearbygalaxies.org>). File names and field names were taken from the image headers and are of the format PROPOSID-TARGNAME, where PROPOSID is the value of the header keyword "PROPOSID" and TARGNAME is the value of the header keyword "TARGNAME." The naming conventions and column names for the files are summarized below, and are contained in the headers of the fits files themselves.

**\*.param:** DOLPHOT parameter files: These files provide the parameters used by DOLPHOT when measuring the photometry, and are useful for interpreting the columns in the raw photometry files. These files are currently only available on the project website.

**\*.phot:** Raw photometry files: These large ASCII files contain the raw output from DOLPHOT. Descriptions of the columns can be found in the DOLPHOT manual (<http://purcell.as.arizona.edu/dolphot/>). The listing of individual columns can be found on the project web site.

**\*.st.fits:** Star files: these files contain the photometry of all objects classified as stars (object type  $\leq 2$ ) with  $S/N > 4$  and data flag  $< 8$ . Compared to the \*.gst files described below, these files will contain more objects and have higher completeness in crowded regions, at the expense of producing less well defined CMDs with more potential contamination from background galaxies. Columns are X, Y, RA, DEC, MAG1\_ACS (or MAG1\_WFPC2 in WFPC2 files), MAG1\_STD, MAG1\_ERR, CHI1, SHARP1, CROWD1, SNR1, FLAG1 (or CHIP in WFPC2 files), MAG2\_ACS (or MAG2\_WFPC2 in WFPC2 files), MAG2\_STD, MAG2\_ERR, CHI2, SHARP2, CROWD2, SNR2, FLAG2 (or FLAG in WFPC2 files). These values are defined as follows. X and Y positions are relative to positions on the drizzled reference image. The MAG1 and MAG2 values refer to the filters given in the file name and in the FITS header. ACS magnitudes are VEGAMAGs, which are calibrated by setting the zeropoint of each filter so that the magnitude of Vega is 0.0 (Sirianni et al. 2005). WFPC2 magnitudes are VEGAMAGs, which are calibrated by setting the zeropoint of each filter so that the magnitude of Vega is 0.035 in most ANGST filters (Holtzman et al. 1995). STD magnitudes have been converted from VEGAMAGs to standard Johnson-Cousins magnitudes for the nearest Johnson-Cousins filter (B, V, or I) using the transformation equations of Sirianni et al. (2005; ACS) and Holtzman et al. (1995; WFPC2). The DOLPHOT CHI value indicates the goodness of the PSF fit, with values of  $< 1.5 - 2.5$  being reasonable for uncrowded well-exposed stars, and values of up to 4-5 being expected for either blended but unresolved stars, or for stars in crowded regions. The SHARP parameter indicates the deviation from a perfect PSF profile, with positive values indicating profiles that are too sharp (such as cosmic rays), and negative values indicating profiles that are too broad (such as unresolved blends, clusters, or background galaxies).

The SNR value gives the signal-to-noise with which the star was detected. The CROWD parameter is in magnitudes, and indicates how much brighter the star would have been if flux from nearby stars had not been subtracted. FLAG1 and FLAG2 are the DOLPHOT quality flags for each filter as described in the manual. FLAG is the Holtzman et al. (2006) quality flag used in the Local Group Stellar Populations Archive. Further details can be found in the DOLPHOT manual.

**\*.gst.fits:** “Good” star files: These files contain the stars that pass the conservative ANGST quality cuts for sharpness and crowding ( $\text{sharp}_1 + \text{sharp}_2)^2 \leq 0.075$  and  $\text{crowd}_1 + \text{crowd}_2 \leq 0.1$ ), in addition to the S/N and flag criteria. Columns and header information are the same as for the **\*.st.fits** files.

The field names, number of stars, and 50% completeness limits can be found in Table 4.

The MAST archive for ANGST also includes copies of the reference images to which all  $X - Y$  positions are tied. For ACS, the reference image is a single dithered image in the deepest filter. For WFPC2, there are four reference images, one for each chip on the camera.

## 11. COLOR-MAGNITUDE DIAGRAMS

In Figures 9-22 we present color magnitude diagrams (CMDs) for all of the fields listed in Tables 2 & 3. The plotted photometry is drawn from the high-quality (**\*.gst.fits**) catalogs. As described above, these quality cuts produce the most well-defined features in the CMD, at the expense of completeness in high-crowding regions (such as the densest stellar clusters). In regions of high stellar density on the CMD, data are plotted as contoured Hess diagrams, with contours drawn at levels of 1,1.5,2,2.5,3,4,6,8,12,16,20  $\times 10^4$  stars  $\text{mag}^{-2}$ . Characteristic photometric uncertainties are shown with error bars on the left side of the CMDs in Figures 9-22.

The ANGST CMDs show a richness of detail, thanks to their depth, high photometric accuracy, and large number of stars. As a guide to interpreting the many features visible in these CMDs, in Figure 23 we plot simulated CMDs that show the locations of different stellar populations, as a function of age (right) and metallicity (left). The plots show the CMDs expected for a constant star formation rate color-coded by age (left) and for an early burst of star formation color-coded by metallicity (right), assuming photometric uncertainties typical for our data at the inner (left panel) and the outer (right) distances of the ANGST target galaxies.

As has been discussed extensively elsewhere (e.g., Gallart et al. 2005, and references therein), the simulated CMDs show how young stellar populations are found primarily in the upper left of the CMD, older stellar populations are found at lower luminosities and redder colors along the red giant branch (RGB) and asymptotic giant branch (AGB), and metal rich stars are found at redder colors for older stellar populations. We do not plot the metallicity dependence of younger stars, since the color of the main sequence has essentially no metal dependence for the filters used in this data release.

Also overlaid on Figure 23 are tracks indicating the typical locations of young main sequence stars, of blue and red core helium burning stars (BHeB and RHeB), and asymptotic giant branch stars. Among these features, the blue and red core helium burning sequences

are the least widely known, since they are only visible when the CMD is well populated. We note that the HeB sequences can produce potentially confusing features in the CMD. In particular, the upper end of the blue core helium burning sequence can be easily mistaken for a “double” main sequence. Additional vertical sequences sometimes appear where BHeB stars pass through the instability strip, leading to a nearly vertical spread in magnitude for variable stars observed only at a single epoch.

## 12. MAGNITUDE OF THE TIP OF THE RED GIANT BRANCH

In Table 5 we list the  $F814W$  magnitude of the tip of the red giant branch (TRGB) for each galaxy. TRGB magnitudes were determined using the edge-detection filter described in Méndez et al. (2002) applied to a Gaussian-smoothed luminosity function as in Sakai et al. (1996) and Seth et al. (2005b). Although more sophisticated techniques exist (e.g., Makarov et al. 2006; Frayn & Gilmore 2003), the TRGB in our sample is typically well-populated and falls well above the photometric limit of the data, making our use of the widely used and calibrated edge-detection technique adequate for an initial distance measurement.

The reported  $F814W$  TRGB magnitude  $m_{TRGB}$  and the associated uncertainty were determined by running 500-750 Monte Carlo trials with bootstrap resampling of the stars. In each trial, additional Gaussian random errors are added to the stars, scaled to the magnitude of each star’s photometric error. Each trial returned the magnitude corresponding to the peak of the edge-detection response filter within a 1 magnitude interval around the likely TRGB. We generated a histogram of the returned magnitudes, and fit the peak at  $m_{TRGB}$  in the histogram with a Gaussian. We take the mean and width of the Gaussian to be the magnitude of the TRGB and its uncertainty. Although the Monte Carlo process artificially increases the photometric error (during randomization of magnitudes) and potentially biases  $m_{TRGB}$  by scattering stars preferentially above the tip, in practice the effect of the added noise is negligible, since the photometric uncertainties are extremely small at  $m_{TRGB}$  in almost every case. Furthermore, we have verified visually that the method above converges on a consistent part of the luminosity function, and thus preserves the accuracy of the relative distances.

In some Monte Carlo trials, there are additional peaks in the edge-detection response function that clearly do not correspond to the TRGB (see Figure 25). These spurious peaks are most prevalent when there are a smaller number of stars, or an old population of AGB stars with a well-defined peak luminosity. In these cases, we initialized the Gaussian fit with a mean chosen to be centered on the peak corresponding most closely to the true TRGB. Examples of the luminosity function, edge-detection response, histogram of Monte Carlo TRGB magnitudes, and the CMD of the analyzed stars are presented in Figures 24 & 25.

Uncertainties in the measured value of  $m_{TRGB}$  can include random errors (due to small numbers of stars and to photometric errors) and systematic errors (due to contamination from stars on the red helium burning sequence, to uncertainties in the MW foreground extinc-

tion, and to the unknown internal extinction). We attempted to reduce our systematic errors by considering only stars likely to be RGB or AGB stars. To do so, we selected stars that fell within model RGB isochrones from Girardi et al. (2008) in the appropriate HST filter set, extrapolated up into the region populated by AGB stars. This process was automated by first shifting the stars in magnitude and color based on the estimated foreground extinction from Schlegel et al. (1998)<sup>22</sup>, assuming  $R_V = 3.1$ ,  $A_{F435W}/A_V = 1.30$ ,  $A_{F475W}/A_V = 1.15$ ,  $A_{F555W}/A_V = 1.00$ ,  $A_{F606W}/A_V = 0.87$ , and  $A_{F814W}/A_V = 0.57$ , based upon Girardi et al. (2008) for typical temperatures of RGB stars. We used triangular interpolation of the isochrones to generate a regular grid of metallicities as a function of color and magnitude for a uniform, intermediate age population (4 Gyr). We then interpolated the observed stars onto this grid to assign metallicities to each star, and rejected stars with unphysical metallicities. This process is equivalent to assigning each star to a particular RGB isochrone, and rejecting stars that are inconsistent with all plausible isochrones. For the remaining stars, we used a robust bi-weight to find the peak and width of the distribution of the logarithms of the inferred metallicities. We selected all stars whose metallicities fell within  $1.5\sigma$  of the peak in  $\log([Fe/H])$ . We further excluded stars with metallicities outside of the range 0.0002 and 0.006 (for 4 Gyr isochrones); within this metallicity range, the  $F814W$  magnitude of the TRGB varies by less than  $\pm 0.05$  mag, but outside it, the TRGB becomes steadily fainter by several tenths of a magnitude, blurring the TRGB discontinuity and introducing systematic errors when converting  $m_{TRGB}$  to distance. We expect little dependence of the TRGB absolute magnitude  $M_{TRGB}$  on age or metallicity; the predicted absolute magnitude of the TRGB depends primarily on the color of the RGB, and more weakly upon the particular age+metallicity combination that generated a particular RGB isochrone. The final isochrone fitting procedure cleanly isolated the bulk of RGB and AGB stars, while significantly reducing contamination from non-RGB features (Figures 24 & 25)<sup>23</sup>.

We further reduced systematic biases due to internal extinction and photometric errors by restricting our analysis to stars in regions of low crowding within an individual field, when sufficient numbers of stars were available ( $>30,000$ ). We chose a density threshold such that at least 25% of the area and 50% of the stars were included in the analysis. This cut eliminated stars in the most crowded regions with the highest internal extinction, while still preserving large numbers of stars. For galaxies with multiple pointings, the TRGB was measured in whichever fields had the least crowding and low-

est probability of high internal or differential reddening, while still having large numbers of stars. When multiple clean fields were available, we analyzed both, to compare our internal systematics and to constrain the variation in internal extinction. The resulting TRGB magnitudes were frequently several tenths of a magnitude brighter than those measured within the main body of a galaxy. Beyond field placement, however, we make no further attempt to correct for internal extinction, although extinctions of several tenths of a magnitude are certainly possible in the outer regions of massive galaxies (e.g., Holwerda et al 2008).

To transfer the measured TRGB magnitudes into initial distance estimates, we used the measured mean color within  $0.2m$  of the TRGB to pick a Girardi et al. (2008) isochrone with similar colors, from which we then find the absolute magnitude  $M_{TRGB}$  of the TRGB. However, due to the uncertain state of the ACS CTE correction, there are likely to be systematic uncertainties present in the data that limit the accuracy of the inferred distance to a few percent. The likely systematic uncertainties in the adopted value of  $M_{TRGB}$  are even larger, with different theoretical models and empirical calibrations differing by as much as 0.2 mag (e.g., see Figure 8 of Gallart et al. 2005). The reported distances are thus best used as relative distances, rather than absolute ones. The uncertainties listed in Table 5 do not include these systematic errors, and include only the Poisson uncertainties captured by bootstrap resampling. Thus, while the Gaussian fitting procedure described above (and seen in the upper left panels of Figures 24 & 25) frequently reports formal distance errors of a few percent, the true uncertainties are undoubtedly larger.

The resulting data in Table 5 includes: the number of stars within 1 magnitude of the TRGB ( $N_{stars}$ ); the adopted foreground extinction  $A_V$ ; the mean color (within 0.2 mag of the TRGB) of the stars used to measure the TRGB, for the particular filter combination used; the predicted absolute magnitude of the TRGB at that color, based on isochrones from Girardi et al. (2008); the apparent magnitude of the TRGB in  $F814W$ , uncorrected for extinction ( $m_{TRGB}(raw)$ ); the extinction corrected TRGB magnitude ( $m_{TRGB}$ ) and its uncertainty; the resulting extinction corrected distance modulus  $(m - M)_0$ ; and the inferred distance  $D$  in Mpc. The resulting spatial configuration of galaxies is shown in Figure 2.

Figure 26 plots the differences between the new distance moduli and those inferred from distances in Table 1, which had been used for initial sample selection, as a function of increasing distance (left) and luminosity (right). The revised distances agree well with previously published values. The median change in distance modulus is only  $-0.02$  mag for the entire sample, indicating that there is little systematic deviation between our adopted TRGB scale and those used in the literature. There is however, a modest tendency for past distances to be systematically overestimated for the most massive galaxies. If we split the sample into galaxies that are brighter or fainter than  $M_B = -17$ , the median offset is only  $-0.012$  for the faint galaxies, but increases to  $-0.074$  for the more luminous galaxies. We believe that that offset is most likely due to past TRGB determinations using stars closer to the galaxies' centers, where the extinction

<sup>22</sup> The one exception is M82, for which the Schlegel et al. (1998) value is clearly contaminated by point source emission from M82 itself, leading to an erroneously high foreground extinction ( $A_B = 0.685$ ). Instead, we took  $A_B = 0.25$ , based upon regions immediately adjacent to M82.

<sup>23</sup> Note that although we derived the "metallicity" of each star, we do not treat these as actual measurements of the metallicity due to the likely presence of mixed stellar ages on the RGB; instead, we only use the inferred metallicity as a label for the RGB isochrone on which a star lies. Likewise, the mean color that we report for the TRGB stars includes only those stars that made the various metallicity cuts, and does not reflect the color of the RGB as a whole.



of dust is larger, leading the TRGB magnitude to appear fainter. In contrast, our measurements use the outskirts of galaxies, where the internal extinction is small, producing a brighter TRGB. On the other hand, many of the published distance estimates have made corrections for internal extinction, unlike those we present in Table 5

Because the most luminous galaxies tend to be found in the M81 group, the left panel shows a hint of correlation between distance and the offset in the distance modulus. However, the Spearman rank correlation coefficient is much smaller when using distance instead of luminosity ( $-0.09$  vs  $0.30$ ), indicating that the variation in luminosity is the principal driver of the trend.

The dispersion about the mean difference is  $0.05$  mag, comparable to the precision of distances in Table 1 and to their published uncertainties. There is no difference in the dispersion for brighter and fainter galaxies. Multiple observations of the same galaxy (connected with a solid line in Figure 26) show differences of typically less than  $0.1$  mag (i.e. 10% in distance). Because these measurements were made in different regions of these galaxies, some of this variation is likely to be due to differences in internal extinction within the galaxy. In such cases, the outermost distance measurement is likely to be the least affected by dust, although the reduced numbers of stars in such fields leads to larger Poisson uncertainties. We also found no systematic offsets between distances determined with ACS and those measured with WFPC2 data.

We see no evidence that the revised distances would have changed our initial sample selection. The largest change in distance is for UGCA 292, which is nearly 40% further away than previously estimated from its brightest stars (Makarova et al. 1998). The distance to MCG9-20-131 also appeared to decrease significantly; however, there is some ambiguity as to whether or not the apparent TRGB is due to RGB or AGB stars, or potentially even red supergiants. Thus, the distance may have a systematic offset, even though the formal error on the magnitude of the tip is relatively small. With the new distances, NGC 247 and NGC 253 are much closer to each other. The morphology of the other groups remain essentially unchanged.

### 13. CONCLUSIONS

The ACS Nearby Galaxy Survey Treasury is the now the largest repository of uniform stellar photometry for nearby galaxies. The resulting catalogs contain millions of measurements that can be used for studies of ancient and recent star formation histories (Williams et al. 2008; Weisz et al. 2008) and comparisons with multi-wavelength data (Gogarten et al. 2008; Ott et al. 2008). The raw images are a resource for searches for stellar clusters, HII region nebosity, and background light sources.

We are happy to acknowledge the consistently professional and helpful assistance from the staff at STSCI, including Alison Vick, Marco Sirianni, Howard Bond, and Neill Reid. We also are pleased to thank Jay Anderson, Brent Tully, Abi Saha, Stan Vlcek, Pat Taylor, Sarah Garner, and Richard Coffey for assistance at various times during the project. We also thank the referee for constructive comments. JJD acknowledges partial support from the Wyckoff Faculty Fellowship during this work, and the hospitality of the MPIA and Carnegie Observatories during some of the writing of this paper. LG acknowledges financial support from contract ASI-NAF I/016/07/0. IK and VK were partially supported by RFFI grant 07-02-00005 and grant DFG-RFBR 06-02-04017.

This work is based on observations made with the NASA/ESA Hubble Space Telescope, obtained from the data archive at the Space Telescope Science Institute. Support for this work was provided by NASA through grant number GO-10915 from the Space Telescope Science Institute, which is operated by AURA, Inc., under NASA contract NAS 5-26555. This research has made use of the NASA/IPAC Infrared Science Archive and the NASA/IPAC Extragalactic Database (NED), which are both operated by the Jet Propulsion Laboratory, California Institute of Technology, under contract with the National Aeronautics and Space Administration. This research has made extensive use of NASA's Astrophysics Data System Bibliographic Services.

*Facilities:* HST (ACS), HST (WFPC2)

### REFERENCES

- Aparicio, A., & Tikhonov, N. 2000, *AJ*, 119, 2183  
 Bedin, L. R., Cassisi, S., Castelli, F., Piotto, G., Anderson, J., Salaris, M., Momany, Y., & Pietrinferni, A. 2005, *MNRAS*, 357, 1038  
 Begum, A., & Chengalur, J. N. 2005, *MNRAS*, 362, 609  
 Bertin, E., & Arnouts, S. 1996, *A&AS*, 117, 393  
 Butler, D. J., Martínez-Delgado, D., & Brandner, W. 2004, *AJ*, 127, 1472  
 Caldwell, N., Armandroff, T. E., Da Costa, G. S., & Seitzer, P. 1998, *AJ*, 115, 535  
 Chiboucas, K., Karachentsev, I. D., & Tully, R. B. 2008, *ArXiv e-prints*, 0805.1250  
 del Río, M. S., Brinks, E., & Cepa, J. 2004, *AJ*, 128, 89  
 Dohm-Palmer, R. C., et al. 1997, *AJ*, 114, 2514  
 Dohm-Palmer, R. C., Skillman, E. D., Mateo, M., Saha, A., Dolphin, A., Tolstoy, E., Gallagher, J. S., & Cole, A. A. 2002, *AJ*, 123, 813  
 Dolphin, A. E. 2000, *PASP*, 112, 1383  
 Dolphin, A. E. et al. 2001, *MNRAS*, 324, 249  
 Dolphin, A. E. 2002, *MNRAS*, 332, 91  
 —. 2002, *AJ*, 123, 3154  
 Dolphin, A. E., et al. 2003, *AJ*, 126, 187  
 Drozdovsky, I. O., Schulte-Ladbeck, R. E., Hopp, U., Greggio, L., & Crone, M. M. 2002, *AJ*, 124, 811  
 Frayn, C. M., & Gilmore, G. F. 2003, *MNRAS*, 339, 887  
 Freedman, W. L., et al. 1994, *ApJ*, 427, 628  
 Gallart, C., Zoccali, M., & Aparicio, A. 2005, *ARA&A*, 43, 387  
 Gieren, W., et al. 2004, *AJ*, 128, 1167  
 Gieren, W., Pietrzyński, G., Soszyński, I., Bresolin, F., Kudritzki, R.-P., Minniti, D., & Storm, J. 2005, *ApJ*, 628, 695  
 Girardi, L. et al. 2008, *PASP*, 120, 583  
 Gogarten, S. M. et al. 2008, *ApJ*, submitted  
 Holtzman, J. A., Afonso, C., & Dolphin, A. 2006, *ApJS*, 166, 534  
 Holtzman, J. A., Burrows, C. J., Casertano, S., Hester, J. J., Trauger, J. T., Watson, A. M., & Worthey, G. 1995, *PASP*, 107, 1065  
 Izotov, Y. I., & Thuan, T. X. 2002, *ApJ*, 567, 875  
 Jarrett, T. H., Chester, T., Cutri, R., Schneider, S. E., & Huchra, J. P. 2003, *AJ*, 125, 525  
 Jee, M. J., Blakeslee, J. P., Sirianni, M., Martel, A. R., White, R. L., & Ford, H. C. 2007, *PASP*, 119, 1403  
 Karachentsev, I. D. 2005, *AJ*, 129, 178  
 Karachentsev, I. D. et al. 2006, *AJ*, 131, 1361  
 —. 2002a, *A&A*, 383, 125  
 —. 2003, *A&A*, 404, 93

- Karachentsev, I. D., Karachentseva, V. E., Huchtmeier, W. K., & Makarov, D. I. 2004, *AJ*, 127, 2031
- Karachentsev, I. D. et al. 2001, *A&A*, 379, 407
- . 2002b, *A&A*, 385, 21
- . 2002c, *A&A*, 389, 812
- Kennicutt, R. et al. 2007, in *American Astronomical Society Meeting Abstracts*, Vol. 211, American Astronomical Society Meeting Abstracts, 95.02–+
- Koekemoer, A. M., Fruchter, A. S., Hook, R. N., & Hack, W. 2002, in *The 2002 HST Calibration Workshop : Hubble after the Installation of the ACS and the NICMOS Cooling System*, ed. S. Arribas, A. Koekemoer, & B. Whitmore, 337–+
- Krist, J. 1995, in *Astronomical Society of the Pacific Conference Series*, Vol. 77, *Astronomical Data Analysis Software and Systems IV*, ed. R. A. Shaw, H. E. Payne, & J. J. E. Hayes, 349–+
- Maíz-Apellániz, J., Cieza, L., & MacKenty, J. W. 2002, *AJ*, 123, 1307
- Makarov, D., Makarova, L., Rizzi, L., Tully, R. B., Dolphin, A. E., Sakai, S., & Shaya, E. J. 2006, *AJ*, 132, 2729
- Makarova, L., Karachentsev, I., Takalo, L. O., Heinaemaeki, P., & Valtonen, M. 1998, *A&AS*, 128, 459
- Mannucci, F., Basile, F., Poggianti, B. M., Cimatti, A., Daddi, E., Pozzetti, L., & Vanzani, L. 2001, *MNRAS*, 326, 745
- Méndez, B., Davis, M., Moustakas, J., Newman, J., Madore, B. F., & Freedman, W. L. 2002, *AJ*, 124, 213
- Minniti, D., Zijlstra, A. A., & Alonso, M. V. 1999, *AJ*, 117, 881
- Mouhcine, M., Ferguson, H. C., Rich, R. M., Brown, T. M., & Smith, T. E. 2005, *ApJ*, 633, 810
- Mutchler, M. et al. 2007, *PASP*, 119, 1
- Olsen, K. A. G., Blum, R. D., & Rigaut, F. 2003, *AJ*, 126, 452
- Ott, J., Skillman, E., Dalcanton, J., Walter, F., Stilp, A., Koribalski, B., West, A., & Warren, S. 2008, *ArXiv e-prints*, 0805.4605
- Rekola, R., Richer, M. G., McCall, M. L., Valtonen, M. J., Kotilainen, J. K., & Flynn, C. 2005, *MNRAS*, 361, 330
- Rhodes, J. D., Massey, R., Albert, J., Taylor, J. E., Koekemoer, A. M., & Leauthaud, A. 2006, in *The 2005 HST Calibration Workshop: Hubble After the Transition to Two-Gyro Mode*, ed. A. M. Koekemoer, P. Goudfrooij, & L. L. Dressel, 21–+
- Rizzi, L., Bresolin, F., Kudritzki, R.-P., Gieren, W., & Pietrzyński, G. 2006, *ApJ*, 638, 766
- Sakai, S., Madore, B. F., & Freedman, W. L. 1996, *ApJ*, 461, 713
- Sakai, S., & Madore, B. F. 1999, *ApJ*, 526, 599
- Sakai, S., & Madore, B. F. 2001, *ApJ*, 555, 280
- Saviane, I., Momany, Y., da Costa, G. S., Rich, R. M., & Hibbard, J. E. 2008, *ApJ*, 678, 179
- Schlegel, D. J., Finkbeiner, D. P., & Davis, M. 1998, *ApJ*, 500, 525
- Seth, A. C., Dalcanton, J. J., & de Jong, R. S. 2005a, *AJ*, 129, 1331
- . 2005b, *AJ*, 130, 1574
- Sirianni, M. et al. 2005, *PASP*, 117, 1049
- Tikhonov, N. A., Galazutdinova, O. A., & Aparicio, A. 2003, *A&A*, 401, 863
- Tikhonov, N. A., Galazutdinova, O. A., & Drozdovsky, I. O. 2005, *A&A*, 431, 127
- Tully, R. B. et al. 2006, *AJ*, 132, 729
- Vaduvescu, O., McCall, M. L., Richer, M. G., & Fingerhut, R. L. 2005, *AJ*, 130, 1593
- van den Bergh, S. 2000, *PASP*, 112, 529
- Weisz, D. R., Skillman, E. D., Cannon, J. M., Dolphin, A. E., Kennicutt, R. C., Lee, J., & Walter, F. 2008, *ApJ*, in press
- Williams, B. F. et al. 2008, *AJ*, submitted
- Windhorst, R. A., Cohen, S. H., Hathi, N. P., Jansen, R. A., & Ryan, R. E. 2008, *The Evolution of Galaxies Through the Neutral Hydrogen Window*, 1035, 318

TABLE 1  
ANGST SAMPLE GALAXIES & PLANNED OBSERVATIONS

Galaxy	Alt. Names	Dist. (Mpc)	RA (J2000)	Dec (J2000)	Diam. ( $\nu$ )	$M_B$	$m_K$	T	$W_{50}$ $\text{km s}^{-1}$	Group	# Fields	Deep?	3 Filt?	Arch?
Antlia		1.3	10:04:04.0	-27:19:55	2.0	-9.38		10	22	14+12	1	Y		10210
SexA	DDO75	1.3	10:11:00.8	-04:41:34	5.5	-13.71		10	63	14+12				7496 <sup>a</sup>
N3109	DDO236	1.3	10:03:07.2	-26:09:36	17.0	-15.18	9.3	9	116	14+12	3	Y	Y	
SexB	U5373	1.4	10:00:00.1	05:19:56	5.1	-13.88		10	38	14+12	1	Y	Y	
KKR25		1.9	16:13:47.6	54:22:16	1.1	-9.94		10		M31(p)?	1	Y		8601 <sup>a</sup>
KK230	KKR3	1.9	14:07:10.7	35:03:37	0.6	-8.49		10	21	M31(p)?	1	Y		9771
E410-005		1.9	00:15:31.4	-32:10:48	1.3	-11.49		-1		14+13				10503
E294-010		1.9	00:26:33.3	-41:51:20	1.1	-10.86		-3		14+13				10503
N55		2.1	00:15:08.5	-39:13:13	32.4	-17.77	6.3	8	172	14+13	5	Y	Y	(9765)
I5152		2.1	22:02:41.9	-51:17:43	5.2	-15.55	9.3	10	91	14+13	1	Y	Y	
GR8	U8091	2.1	12:58:40.4	14:13:03	1.1	-12.00	12.9	10	26		1	Y		
N300		2.1	00:54:53.5	-37:40:57	21.9	-17.66	6.4	7	149	14+13	4	Y	Y	(9492)
UA438	E407-18	2.2	23:26:27.5	-32:23:26	1.5	-12.85		10	34	14+13	1	Y		8192 <sup>a</sup>
DDO187	U9128	2.3	14:15:56.5	23:03:19	1.7	-12.43	12.5	10	34		1	Y		10210
KKH98		2.5	23:45:34.0	38:43:04	1.1	-10.29		10	22	M31(p)?	1			
DDO125	U7577	2.5	12:27:41.8	43:29:38	4.3	-14.04		10	30	14+07	1		Y	8601 <sup>a</sup>
U8508	IZw60	2.6	13:30:44.4	54:54:36	1.7	-12.95	12.0	10	49	14+07	1			
KKH86		2.6	13:54:33.6	04:14:35	0.7	-10.19		10	14		1			8601 <sup>a</sup>
DDO99	U6817	2.6	11:50:53.0	38:52:50	4.1	-13.37		10	37	14+07	1			8601 <sup>a</sup>
DDO190	U9240	2.8	14:24:43.5	44:31:33	1.8	-14.14		10	45	14+08	1		Y	
DDO113	UA276	2.9	12:14:57.9	36:13:08	1.5	-11.61		10		14+07	1			
N4214	U7278	2.9	12:15:38.9	36:19:39	8.5	-17.07	7.9	10	62	14+07	1	Y	Y	
DDO181	U8651	3.0	13:39:53.8	40:44:21	2.3	-12.94		10	39	14+08	1			10210
N3741	U6572	3.0	11:36:06.4	45:17:07	2.0	-13.01	12.2	10	81	14+07	1			
N4163	U7199	3.0	12:12:08.9	36:10:10	1.9	-13.76	10.9	10	18	14+07	1		Y	
N404	U718	3.1	01:09:26.9	35:43:03	2.5	-16.25	8.6	-1	78		1	Y	Y	
UA292	CVnI-dwA	3.1	12:38:40.0	32:46:00	1.0	-11.36		10	27		1			(10905)
U8833		3.1	13:54:48.7	35:50:15	0.9	-12.31		10	28	14+08	1			10210
DDO183	U8760	3.2	13:50:51.1	38:01:16	2.2	-13.08		9		14+08	1			
N2366	U3851	3.2	07:28:52.0	69:12:19	7.3	-15.85	10.6	10	96	M81(p)				10605
DDO44	UA133	3.2	07:34:11.3	66:53:10	3.0	-11.89		-3		M81(p)	1			
E321-014		3.2	12:13:49.6	-38:13:53	1.4	-12.31		10	25	CenA(p)	1			8601 <sup>a</sup>
U4483		3.2	08:37:03.0	69:46:31	1.2	-12.58		10	33	M81				8769 <sup>a</sup>
N2403	U3918	3.3	07:36:54.4	65:35:58	21.9	-18.77	6.2	6	231	M81	4	Y	Y	10182,10579,10523
DDO6	UA15	3.3	00:49:49.3	-21:00:58	1.7	-12.40		10	22	Scl	1			
KKH37		3.4	06:47:45.8	80:07:26	1.2	-11.26		10	20		1			9771
HoII	U4305	3.4	08:19:05.9	70:42:51	7.9	-16.57	8.8	10	66	M81		Y	Y	10605
KDG2	E540-030,KK9	3.4	00:49:21.1	-18:04:28	1.2	-11.29		-1		Scl				10503
MCG9-20-131		3.4	12:15:46.7	52:23:15	1.2	-12.36		10		M81?	1			10905 <sup>b</sup>
E540-032		3.4	00:50:24.6	-19:54:25	1.3	-11.22		-3		Scl				10503
FM1	F6D1	3.4	09:45:25.6	68:45:27	0.9	-10.16		-3		M81				9884
KK77	F12D1	3.5	09:50:10.0	67:30:24	2.4	-11.42		-3		M81				9884
KDG63	U5428,DDO71	3.5	10:05:07.3	66:33:18	1.7	-11.71		-3	19	M81				9884
N4190	U7232	3.5	12:13:44.6	36:38:00	1.7	-14.20	10.8	10	46		1		Y	10905 <sup>b</sup>
M82	N3034,U5322	3.5	09:55:53.9	69:40:57	11.2	-18.66	4.7	8	147	M81	1	Y	Y	(10776)
KDG52	M81-Dwarf-A	3.5	08:23:56.0	71:01:46	1.3	-11.37		10	22	M81				10605
DDO53	U4459	3.5	08:34:06.5	66:10:45	1.6	-13.23		10	25	M81				10605
N2976	U5221	3.6	09:47:15.6	67:54:49	5.9	-16.77	7.5	5	97	M81	1	Y	Y	
KDG61		3.6	09:57:02.7	68:35:30	2.4	-12.54		-1		M81				9884
M81	N3031,U5318	3.6	09:55:33.5	69:04:00	26.9	-20.09	3.8	3	422	M81	1	Y	Y	(10250,10584,10523)
N247	UA11	3.6	00:47:08.3	-20:45:36	15.4	-17.92	7.4	7	210	Scl	4	Y	Y	(9771)
HoIX	U5336,DDO66,KDG62	3.7	09:57:32.4	69:02:35	2.5	-13.31		10	69	M81				10605
KDG64	U5442	3.7	10:07:01.9	67:49:39	1.9	-12.32		-3		M81				9884
IKN		3.7	10:08:05.9	68:23:57	2.7	-10.84		-3		M81				9771

TABLE 1 — *Continued*

Galaxy	Alt. Names	Dist. (Mpc)	RA (J2000)	Dec (J2000)	Diam. ( $\iota$ )	$M_B$	$m_K$	T	$W_{50}$ $\text{km s}^{-1}$	Group	# Fields	Deep?	3 Filt?	Arch?
KDG73		3.7	10:52:55.3	69:32:45	0.6	-10.75		10	18	M81	1			
DDO78		3.7	10:26:27.9	67:39:24	2.0	-12.04		-3		M81	1			
F8D1		3.8	09:44:47.1	67:26:19	5.5	-12.20		-3		M81				5898 <sup>a</sup>
BK5N		3.8	10:04:40.3	68:15:20	0.8	-10.37		-3		M81	-			5898 <sup>b</sup> ,6964 <sup>a</sup>
N3077	U5398	3.8	10:03:21.0	68:44:02	5.4	-17.44	7.3	10	65	M81	2	Y	Y	(9381)
HoI	U5139,DDO63	3.8	09:40:28.2	71:11:11	3.6	-14.26		10	29	M81	-		Y	10605
BK6N		3.8	10:34:31.9	66:00:42	1.1	-11.06		-3		M81	1			
A0952+69		3.9	09:57:29.0	69:16:20	1.8	-11.16		10		M81	1			
KKH57		3.9	10:00:16.0	63:11:06	0.6	-10.09		-3		M81	1			
N253	UA13	3.9	00:47:34.3	-25:17:32	26.7	-20.04	3.8	5	410	Scl	6	Y	Y	
HS117		4.0	10:21:25.2	71:06:58	1.5	-11.51		10	13	M81	1			9771
DDO82	U5692	4.0	10:30:35.0	70:37:10	3.4	-14.44		9		M81	1		Y	
BK3N		4.0	09:53:48.5	68:58:09	0.5	-9.23		10	15	M81	1			
I2574	U5666,DDO81	4.0	10:28:22.4	68:24:58	13.2	-17.17	10.7	9	115	M81				9755,10605
Sc22	Sc-dE1	4.2	00:23:51.7	-24:42:18	0.9	-10.39		10		Scl				10503

NOTE. — Distances,  $M_B$ ,  $W_{50}$ , and T-type taken from CNG; values for  $m_K$  are total  $K$  magnitudes from either the 2MASS Large Galaxy Atlas (Jarrett et al. 2003) or from Vaduvescu et al. (2005) for dwarfs; Group membership from Karachentsev (2005) or Tully et al. (2006); # of ANGST Pointings includes any planned deep fields; Deep column indicates planned observations that would reach high completeness in red clump; Note that not all planned observations were executed, due to ACS failure – actual observations are given in Table 2; 3 Filter column indicates observations made in  $F475W+F606W+F814W$ , rather than default  $F475W+F606W$  for dwarfs; Archival lists Proposal ID of archival data to be used, with entries in parentheses indicating that archival data will be supplemented with new observations; HI detection for KKR25 in the CNG was not confirmed in later GMRT observations (Begum & Chengalur 2005); (a) WFPC2 Archival data.

TABLE 2  
ANGST OBSERVATIONS

Field Name	RA (J2000)	Dec (J2000)	V3 PA (deg)	Aperture	Date Range	Instr.	Filter	Exptime (s)
NGC3109-WIDE1	10 02 41.8	-26 08 58	95.001	WFALL-FIX	2007-11-02	WFPC2	F606W F814W	2700 3900
NGC3109-WIDE2	10 02 49.9	-26 09 07	95.001	WFALL-FIX	2007-11-08	WFPC2	F606W F814W	2700 3900
NGC3109-WIDE3	10 02 57.81	-26 09 16.4	95.001	WFALL-FIX	2007-11-06	WFPC2	F606W F814W	2400 2400
NGC3109-WIDE4	10 03 05.81	-26 09 25.6	95.001	WFALL-FIX	2007-11-10	WFPC2	F606W F814W	2400 2400
NGC3109-DEEP	10 02 34.1	-26 09 23	123.658	WFALL-FIX	2007-12-20	WFPC2	F606W F814W	2700 3900
SEXB-DEEP	10 00 03.9	+05 19 29	112.614	WFALL-FIX	2007-12-12	WFPC2	F606W F814W	2700 3900
NGC0055-WIDE1	00 14 15.4	-39 09 45	101.142	WFALL	2007-07-28	WFPC2	F606W F814W	900 2600
					2008-07-06	WFPC2	F606W F814W	1100 1100
NGC0055-WIDE2	00 14 20.0	-39 09 56	101.141	WFALL	2008-07-04	WFPC2	F606W F814W	1800 2600
NGC0055-WIDE3	00 14 28.9	-39 10 18	101.142	WFALL	2007-08-07	WFPC2	F606W F814W	2700 3900
NGC0055-WIDE4	00 14 37.2	-39 10 42	104.002	WFALL	2007-08-09	WFPC2	F606W F814W	2700 3900
NGC0055-WIDE5	00 15 10.4	-39 12 58	101.142	WFALL	2007-08-06	WFPC2	F606W F814W	2700 3900
NGC0055-DEEP	00 13 44.4	-39 07 43	58.335	WFALL-FIX	2007-06-02	WFPC2	F606W F814W	4800 9600
IC5152-DEEP	22 03 12.0	-51 18 33	76.003	WFALL-FIX	2007-06-19 2007-06-20	WFPC2	F606W F814W	4800 9600
GR8	12 58 40.94	+14 13 00.6	112.560	WFC1-FIX	2007-01-03	ACS	F475W F814W	2244 2259
NGC0300-WIDE1	00 54 21.5	-37 37 58	209.925	WFCENTER	2006-11-10	ACS	F475W F606W F814W	1488 1515 1542
NGC0300-WIDE2	00 54 34.8	-37 39 27	209.925	WFCENTER	2006-11-08	ACS	F475W F606W F814W	1488 1515 1542
NGC0300-WIDE3	00 54 47.8	-37 40 53	209.925	WFCENTER	2006-11-09	ACS	F475W F606W F814W	1488 1515 1542
KKH98	23 45 34.19	+38 43 10.1	230.070	WFC1-FIX	2007-01-02	ACS	F475W F814W	2265 2280
UGC8508	13 30 44.95	+54 54 37.1	122.276	WFC1-FIX	2006-12-21	ACS	F475W F814W	2280 2349
DDO190	14 24 43.72	+44 31 35.2	158.711	WFC1-FIX	2006-11-21 2006-11-22	ACS	F475W F606W F814W	2274 2301 2265
DDO113	12 14 58.28	+36 13 03.1	137.247	WFC1-FIX	2006-11-03	ACS	F475W F814W	2265 2280
NGC4214-DEEP	12 15 22.9	+36 21 50	119.879	WFALL-FIX	2007-12-04 2007-12-23	WFPC2	F606W F814W	15600 31200
NGC3741	11 36 06.46	+45 17 03.4	134.012	WFC1-FIX	2006-11-01	ACS	F475W F814W	2262 2331
NGC4163	12 12 09.57	+36 10 07.0	116.647	WFC1-FIX	2006-12-08	ACS	F475W F814W F606W	2265 2250 2292
NGC0404-DEEP	01 09 16.9	+35 44 51	49.998	WFALL-FIX	2007-08-08 2007-09-19	WFPC2	F606W F814W	39000 75400
UGCA292	12 38 40.43	+32 45 58.5	121.996	WFC1-FIX	2007-01-01	ACS	F475W F814W	2250 2274
DDO44	07 34 12.48	+66 53 08.4	112.749	WFC-FIX	2006-09-21	ACS	F475W F814W	2361 2430
NGC2403-DEEP	07 38 05.5	+65 30 16.0	69.995	WFALL-FIX	2007-11-26 2007-12-01	WFPC2	F606W F814W	32400 62100
DDO6	00 49 49.69	-21 01 00.5	121.489	WFC1-FIX	2006-09-19	ACS	F475W F814W	2250 2268
KKH37	06 47 47.64	+80 07 29.7	58.707	WFC1-FIX	2006-11-10	ACS	F475W F814W	2469 2541
NGC2976-WIDE1	09 47 17.0	+67 53 58	52.756	WFCENTER	2006-12-30	ACS	F475W F606W F814W	1570 1596 1622
NGC2976-DEEP	09 47 36.6	+67 51 25	51.353	WFCENTER	2006-12-27 2007-01-10	ACS	F475W F606W F814W	2418 18816 27191
M81-DEEP	09 54 34.7	+69 16 50	89.814	WFCENTER	2006-11-16 2006-11-20	ACS	F475W F606W	2418 24232

TABLE 2 — *Continued*

Field Name	RA (J2000)	Dec (J2000)	V3 PA (deg)	Aperture	Date Range	Instr.	Filter	Exptime (s)
NGC0247-WIDE1	00 47 19.06	-20 52 12.2	167.978	WFCENTER	2006-09-22	ACS	F814W	29953
							F475W	2253
							F606W	2280
							F814W	2250
NGC0247-WIDE2	00 47 12.5	-20 49 14	167.979	WFCENTER	2006-09-20	ACS	F475W	1480
							F606W	1507
							F814W	1534
NGC0247-WIDE3	00 47 10.4	-20 46 09	167.979	WFCENTER	2006-09-21	ACS	F475W	1480
							F606W	1507
							F814W	1534
KDG73	10 52 58.54	+69 32 52.1	71.609	WFC1-FIX	2007-01-01	ACS	F475W	2250
							F814W	2274
DDO78	10 26 29.17	+67 39 12.1	130.158	WFC1-FIX	2006-10-18	ACS	F475W	2274
							F814W	2292
NGC3077-WIDE1	10 03 28.4	+68 43 53	153.086	WFCENTER	2006-09-21	ACS	F475W	1570
							F606W	1596
							F814W	1622
A0952+69	09 57 36.08	+69 16 59.5	148.862	WFC1-FIX	2006-09-22	ACS	F475W	2250
							F814W	2265
NGC0253-WIDE1	00 48 19.59	-25 08 51.2	144.990	WFCENTER	2006-09-19	ACS	F475W	2256
							F606W	2283
							F814W	2253
NGC0253-WIDE2	00 48 08.7	-25 10 48	139.995	WFCENTER	2006-09-08	ACS	F475W	1482
							F606W	1508
							F814W	1534
NGC0253-WIDE3	00 47 57.9	-25 12 48	159.219	WFCENTER	2006-09-15	ACS	F475W	1482
							F606W	1508
							F814W	1534
NGC0253-WIDE4	00 47 47.2	-25 14 46	140.893	WFCENTER	2006-09-09	ACS	F475W	1482
							F606W	1508
							F814W	1534
NGC0253-WIDE5	00 47 36.4	-25 16 46	139.995	WFCENTER	2006-09-13	ACS	F475W	1482
							F606W	1508
							F814W	1534
DDO82	10 30 37.80	+70 37 13.0	157.574	WFC-FIX	2006-09-22	ACS	F475W	2400
							F606W	2454
							F814W	2442
BK3N	09 53 47.81	+68 58 06.7	148.844	WFC1-FIX	2006-09-20	ACS	F475W	2250
							F814W	2265

NOTE. — All data is from GO-10915, except NGC 55 and NGC 3109 wide fields, which are from DD-11307. Entries with reduced precision in the listings for RA and Dec indicate a representative center for dithered observations. Multiple dates for a given field indicate the start times for the earliest and the latest observations of that field. Note that many fine guidance sensor problems occurred during observations for GO-10915, and that not all data in the archive under this PID is useable; only high quality observations are included in this table.

TABLE 3  
ARCHIVAL OBSERVATIONS

Catalog Name	Target Name	PID	RA (J2000)	Dec (J2000)	Ang. Sep. (')	V3 PA (deg)	Aperture	Date Range	Instr.	Filter	Exptime (s)	Literature CMD
Antlia	ANTLIA	10210	10 04 03.77	-27 19 47.2	0.14	247.479	WFC1	2005-04-02	ACS	F814W F606W	1174 985	1
SexA	DDO75	7496	10 10 56.9	-04 41 30	0.983	287.891	WF3-FIX	1999-04-05 1999-04-08	WFPC2	F555W F814W	19200 38400	2
KKR25	KKR25	8601	16 13 47.47	+54 21 27.7	0.83	358.523	WF3-FIX	2001-05-28	WFPC2	F606W F814W	600 600	9
KK230	KK230	9771	14 07 10.70	+35 03 37.0	0.00	18.337	WFC	2004-04-06	ACS	F606W F814W	1200 900	3
E410-005	ESO410-005	10503	00 15 31.4	-32 10 47	0.02	~44	WFC	2006-05-05 2006-05-10	ACS	F606W F814W	26880 53760	
E294-010	ESO294-010	10503	00 26 33.4	-41 51 19	0.03	~37	WFC	2006-05-03 2006-05-05	ACS	F606W F814W	27840 55680	
N55	NGC0055	9765	00 14 53.60	-39 11 48.0	3.21	174.052	WFCENTER	2003-09-23	ACS	F606W F814W	400 676	5
N55	NGC0055-DISK	9765	00 15 31.03	-39 14 12.0	4.47	245.349	WFCENTER	2003-12-16	ACS	F606W F814W	676 700	5
N300	NGC300-1	9492	00 55 34.12	-37 41 25.4	8.05	80.254	WFC	2002-07-17	ACS	F435W F555W F814W	1080 1080 1440	6,7
N300	NGC300-2	9492	00 54 51.93	-37 38 56.1	2.04	92.050	WFC	2002-07-19	ACS	F435W F555W F814W	1080 1080 1440	6,7
N300	NGC300-3	9492	00 54 55.32	-37 41 48.9	0.94	171.953	WFC	2002-09-28	ACS	F435W F555W F814W	1080 1080 1440	6,7
N300	NGC300-4	9492	00 54 23.12	-37 34 19.9	8.94	80.060	WFC	2002-07-21	ACS	F435W F555W F814W	1080 1080 1440	6,7
N300	NGC300-5	9492	00 54 28.11	-37 38 56.8	5.41	240.928	WFC	2002-12-25	ACS	F435W F555W F814W	1080 1080 1440	6,7
N300	NGC300-6	9492	00 54 26.95	-37 44 11.2	6.17	168.956	WFC	2002-09-26	ACS	F435W F555W F814W	1080 1080 1440	6,7
UA438	E407-G18	8192	23 26 30.92	-32 22 44.4	0.926	224.243	WF3-FIX	1999-10-23	WFPC2	F606W F814W	600 600	10
DDO187	UGC9128	10210	14 15 56.57	+23 03 24.6	0.09	286.046	WFC1	2004-07-28	ACS	F606W F814W	985 1174	1
DDO125	UGC7577	8601	12 27 45.64	+43 29 17.0	0.779	293.217	WF3-FIX	2001-06-19	WFPC2	F606W F814W	600 600	10
KKH86	KKH71	8601	13 54 36.15	+04 14 08.1	0.786	301.415	WF3-FIX	2001-06-10	WFPC2	F606W F814W	600 600	10
DDO99	UGC6817	8601	11 50 56.60	+38 52 30.7	0.809	292.285	WF3-FIX	2001-06-12	WFPC2	F606W F814W	600 600	10
DDO181	UGC8651	10210	13 39 53.82	+40 44 20.7	0.01	269.263	WFC1	2004-08-06	ACS	F606W F814W	1016 1209	1
UA292	UGCA-292	10905	12 38 40.01	+32 46 01.0	0.02	121.995	WFC1	2006-12-14	ACS	F606W	926	
U8833	UGC8833	10210	13 54 48.67	+35 50 14.7	0.01	279.439	WFC	2004-07-31	ACS	F606W F814W	998 1189	1
DDO183	UGC8760	10210	13 50 50.98	+38 01 08.0	0.14	274.638	WFC1	2004-08-03	ACS	F606W F814W	998 1189	1
N2366	NGC-2366-1	10605	07 28 43.5	+69 11 22	1.19	74.02	WFC	2006-11-10	ACS	F555W F814W	9560 9560	4
N2366	NGC-2366-2	10605	07 29 00.0	+69 14 05.2	1.91	95.85	WFC	2006-11-11	ACS	F555W	9560	4

ANGST

TABLE 3 — *Continued*

Catalog Name	Target Name	PID	RA (J2000)	Dec (J2000)	Ang. Sep. (')	V3 PA (deg)	Aperture	Date Range	Instr.	Filter	Exptime (s)	Literature CMD
E321-014	PGC39032	8601	12 13 51.38	-38 14 33.8	0.780	330.277	WF3-FIX	2000-09-01	WFPC2	F814W	9560	11
U4483	UGC4483	8769	08 37 05.40	+69 46 13.6	0.357	164.556	PC1	2000-08-12	WFPC2	F606W	600	
N2403	SN-NGC2403-PR	10182	07 36 57.22	+65 36 21.5	0.49	140.028	WFC	2004-08-17	ACS	F814W	600	12, 13
N2403	NGC2403-X1	10579	07 36 25.56	+65 35 40.1	2.99	95.661	WFC1	2005-10-17	ACS	F555W	9500	
N2403	NGC2403-HALO-1	10523	07 37 52.70	+65 31 31.0	7.854	107.68	WFC	2005-09-29	ACS	F814W	6000	3
N2403	NGC2403-HALO-6	10523	07 37 29.37	+65 40 29.1	5.78	97.839	WFC	2005-10-14	ACS	F475W	1200	
KKH37	KKH37	9771	06 47 46.90	+80 07 26.0	0.05	319.556	WFC	2004-02-07	ACS	F606W	700	4
HoII	UGC-4305-1	10605	08 18 59.0	+70 42 05	0.92	30.76	WFC	2006-12-30	ACS	F814W	700	
HoII	UGC-4305-2	10605	08 19 20.6	+70 43 45	1.53	30.67	WFC	2006-12-30	ACS	F435W	1248	4
E540-030	ESO540-030	10503	00 49 21.2	-18 04 33	0.10	~74	WFC	2006-07-11	ACS	F606W	1248	
MCG9-20-131	CGCG-269-049	10905	12 15 44.0	+52 23 58			WF3	2007-10-31	WFPC2	F814W	710	3
E540-032	ESO540-032	10503	00 50 24.5	-19 54 23	0.04	104.385	WFC	2006-09-03	ACS	F606W	720	
E540-032	ESO540-032	10503	00 50 24.51	-19 54 23	0.04	69.516	WFC	2006-07-07	ACS	F814W	720	3
FM1	M81F6D1	9884	09 45 20.55	+68 45 26.5	1.06	312.999	WFC	2006-07-10	ACS	F606W	720	
KK77	M81F12D1	9884	09 50 09.28	+67 29 50.1	0.57	6.202	WFC	2004-04-06	ACS	F814W	900	4
KDG63	DDO71	9884	10 05 15.74	+66 33 16.5	0.84	316.241	WFC	2004-02-09	ACS	F555W	9320	
N4190 <sup>a</sup>	NGC-4190	10905	12 13 44.40	+36 37 14	0.80	4.237	WF3	2008-03-21	WFPC2	F814W	9320	4
M82	M82-POS1	10776	09 56 06.7	+69 44 17	3.50	310.02	WFCENTER	2006-07-11	ACS	F606W	17200	
M82	M82-POS2	10776	09 55 42.0	+69 41 54	1.39	310.02	WFCENTER	2004-04-05	ACS	F814W	9000	4
M82	M82-POS3	10776	09 55 17.0	+69 39 32	3.48	310.02	WFCENTER	2004-04-05	ACS	F606W	9000	
M82	M82-POS4	10776	09 55 46.7	+69 37 33	3.44	310.02	WFCENTER	2006-03-27	ACS	F814W	9000	4
M82	M82-POS5	10776	09 56 11.8	+69 39 55	1.84	310.02	WFCENTER	2006-03-28	ACS	F606W	9000	
M82	M82-POS6	10776	09 56 36.0	+69 42 18	3.89	310.02	WFCENTER	2006-03-29	ACS	F814W	9000	4
KDG52	MESSIER-081-DWARF-A	10605	08 23 55.8	+71 01 46	0.05	297.84	WFC	2006-03-29	ACS	F606W	9000	
										F814W	2200	
										F555W	1360	
										F814W	700	
										F435W	1800	
										F555W	1360	
										F814W	700	
										F435W	1800	
										F555W	1360	
										F814W	700	
										F435W	1800	
										F555W	1360	
										F814W	700	
										F555W	11828	



TABLE 3 — *Continued*

Catalog Name	Target Name	PID	RA (J2000)	Dec (J2000)	Ang. Sep. (')	V3 PA (deg)	Aperture	Date Range	Instr.	Filter	Exptime (s)	Literature CMD
DDO53	UGC-04459	10605	08 34 07.0	+66 10 55	0.17	302.57	WFC	2006-03-25	ACS	F814W	11872	4
KDG61	M81K61	9884	09 56 58.78	+68 35 49.6	0.48	15.578	WFC	2004-02-10	ACS	F555W	9536	
M81	NGC3031-HALO-1	10523	09 57 17.23	+69 06 29.3	9.58	117.087	WFC	2005-10-31	ACS	F814W	9536	
M81	NGC3031-HALO-2	10523	09 58 04.50	+69 08 52.1	14.37	117.321	WFC	2005-10-31	ACS	F606W	17800	
M81	M81-X-9	9796	09 57 54.30	+69 03 46.4	12.61	14.181	WFC1	2004-02-07	ACS	F814W	9000	
M81	M81-X-9	9796	09 57 54.30	+69 03 46.4	12.61	323.352	WFC	2004-03-25	ACS	F606W	710	
M81	M81-FIELD-1	10584	09 54 16.49	+69 13 42.3	11.93	329.925	WFCENTER	2006-03-23	ACS	F814W	710	
M81	M81-FIELD-2	10584	09 54 52.27	+69 14 54.3	11.57	59.748	WFCENTER	2006-12-30	ACS	F606W	735	
M81	M81-FIELD-3	10584	09 54 09.18	+69 09 49.5	9.51	64.655	WFCENTER	2005-12-10	ACS	F555W	1160	
M81	M81-FIELD-4	10584	09 54 41.78	+69 11 06.7	8.47	68.571	WFCENTER	2005-12-06	ACS	F814W	1160	
M81	M81-FIELD-5	10584	09 55 13.52	+69 12 25.1	8.60	329.926	WFCENTER	2006-03-22	ACS	F435W	2520	
M81	M81-FIELD-6	10584	09 55 46.09	+69 13 42.4	9.77	329.926	WFCENTER	2006-03-23	ACS	F555W	1160	
M81	M81-FIELD-7	10584	09 54 17.45	+69 08 27.4	8.115	64.984	WFCENTER	2005-12-15	ACS	F814W	1160	
M81	M81-FIELD-7	10584	09 54 22.89	+69 06 56.8	6.95	329.926	WFCENTER	2006-03-23	ACS	F435W	2400	
M81	M81-FIELD-8	10584	09 54 55.47	+69 08 14.2	5.43	329.926	WFCENTER	2006-03-22	ACS	F555W	2400	
M81	M81-FIELD-9	10584	09 55 11.57	+69 08 49.8	5.21	329.862	WFCENTER	2006-03-22	ACS	F606W	1565	
M81	M81-FIELD-9	10584	09 55 28.04	+69 09 31.5	5.55	329.926	WFCENTER	2006-03-20	ACS	F814W	1580	
M81	M81-FIELD-10	10584	09 56 00.66	+69 10 49.0	7.23	334.924	WFCENTER	2006-03-25	ACS	F435W	1595	
M81	M81-FIELD-11	10584	09 54 32.00	+69 05 33.9	5.71	65.041	WFCENTER	2005-12-15	ACS	F606W	1580	
M81	M81-FIELD-11	10584	09 54 38.25	+69 04 02.3	4.94	67.905	WFCENTER	2005-12-08	ACS	F814W	1595	
M81	M81-FIELD-12	10584	09 55 09.99	+69 05 20.6	2.49	329.927	WFCENTER	2006-03-26	ACS	F435W	1200	
M81	M81-FIELD-13	10584	09 55 26.13	+69 05 56.4	2.05	329.919	WFCENTER	2006-03-22	ACS	F555W	1200	
M81	M81-FIELD-13	10584	09 55 43.41	+69 06 37.0	2.76	69.764	WFCENTER	2005-12-07	ACS	F606W	1200	
M81	M81-FIELD-14	10584	09 56 15.18	+69 07 55.5	5.41	334.980	WFCENTER	2006-03-26	ACS	F435W	1200	
M81	M81-FIELD-15	10584	09 54 35.17	+69 00 33.4	6.25	333.265	WFCENTER	2006-03-23	ACS	F555W	1200	
M81	M81-FIELD-15	10584	09 54 52.01	+69 01 10.0	4.67	338.616	WFCENTER	2006-03-20	ACS	F606W	1200	

TABLE 3 — *Continued*

Catalog Name	Target Name	PID	RA (J2000)	Dec (J2000)	Ang. Sep. (')	V3 PA (deg)	Aperture	Date Range	Instr.	Filter	Exptime (s)	Literature CMD
M81	M81-FIELD-16	10584	09 55 25.11	+69 02 22.0	1.80	159.951	WFCENTER	2006-09-08	ACS	F435W	1200	
M81	M81-FIELD-17	10584	09 55 40.69	+69 03 02.7	1.15	329.863	WFCENTER	2006-03-27	ACS	F606W	1200	
M81	M81-FIELD-17	10584	09 55 57.09	+69 03 44.5	2.12	329.927	WFCENTER	2006-03-21	ACS	F435W	465	
M81	M81-FIELD-18	10584	09 56 30.51	+69 05 00.8	5.19	69.765	WFCENTER	2005-12-07	ACS	F606W	470	
M81	M81-FIELD-19	10584	09 54 49.72	+68 57 40.0	7.45	333.321	WFCENTER	2006-03-23	ACS	F435W	1200	
M81	M81-FIELD-19	10584	09 55 07.30	+68 58 15.2	6.21	69.766	WFCENTER	2005-12-06	ACS	F606W	1200	
M81	M81-FIELD-20	10584	09 55 39.04	+68 59 33.5	4.47	329.927	WFCENTER	2006-03-22	ACS	F435W	400	
M81	M81-FIELD-21	10584	09 55 55.25	+69 00 09.3	4.31	329.920	WFCENTER	2006-03-27	ACS	F606W	450	
M81	M81-FIELD-21	10584	09 56 11.62	+69 00 50.9	4.64	329.927	WFCENTER	2006-03-25	ACS	F435W	1200	
M81	M81-FIELD-22	10584	09 56 45.03	+69 02 07.3	6.66	69.765	WFCENTER	2005-12-09	ACS	F606W	1200	
M81	M81-FIELD-23	10584	09 55 21.82	+68 55 21.6	8.70	69.767	WFCENTER	2005-12-09	ACS	F435W	1200	
M81	M81-FIELD-24	10584	09 55 53.57	+68 56 40.0	7.55	329.927	WFCENTER	2006-03-22	ACS	F606W	1200	
M81	M81-FIELD-25	10584	09 56 26.98	+68 57 56.4	7.72	69.766	WFCENTER	2005-12-05	ACS	F435W	1200	
M81	M81-FIELD-26	10584	09 56 59.55	+68 59 13.8	9.06	68.603	WFCENTER	2005-12-10	ACS	F606W	1200	
M81	M81-FIELD-27	10584	09 55 59.05	+68 53 27.4	10.72	63.395	WFCENTER	2006-12-26	ACS	F435W	1565	
M81	M81-FIELD-28	10584	09 56 29.23	+68 54 42.5	10.49	69.769	WFCENTER	2005-12-09	ACS	F606W	1580	
M81	M81-FIELD-29	10584	09 57 01.91	+68 55 56.2	11.26	69.768	WFCENTER	2005-12-06	ACS	F814W	1595	
N247	NGC247	9771	00 47 06.10	-20 39 04.0	6.55	263.664	WFC	2004-02-02	ACS	F435W	1565	3
HoIX	UGC-5336	10605	09 57 31.8	+69 02 46	0.22	325.36	WFC	2006-03-23	ACS	F606W	1200	4
KDG64	M81K64	9884	10 07 09.85	+67 49 57.9	0.81	78.806	WFC	2003-12-20	ACS	F814W	900	
IKN	IKN	9771	10 08 05.90	+68 23 57.0	0.00	187.352	WFC	2003-08-17	ACS	F555W	9536	3
F8D1	GAL-094447+672619	5898	09 44 44	+67 26 41	0.5	~320	PC1	1996-02-23	WFPC2	F814W	900	8
BK5N	GAL-100441+681522	5898	10 04 40.3	+68 15 52.7	0.544	355.514	PC1	1996-04-17	WFPC2	F555W	18360	
BK5N	GAL-100441+681522	6964	10 04 35.7	+68 15 17.2	0.432	264.979	PC1	1996-02-22	WFPC2	F814W	27140	8
N3077	NGC3077-PHOENIX	9381	10 03 51.6	+68 41 26	3.80	335.19	WFC	1996-06-09	WFPC2	F555W	17559	8
HoI	UGC-5139	10605	09 40 32.1	+71 11 15	0.33	9.156	WFC	2003-03-12	ACS	F814W	5400	4
								2003-03-14		F555W	11400	
										F814W	12000	
										F555W	19200	
										F814W	38400	
										F555W	8892	4

TABLE 3 — *Continued*

Catalog Name	Target Name	PID	RA (J2000)	Dec (J2000)	Ang. Sep. (')	V3 PA (deg)	Aperture	Date Range	Instr.	Filter	Exptime (s)	Literature CMD
HS117	HS117	9771	10 21 25.20	+71 06 58.0	0.00	127.715	WFC	2003-10-25	ACS	F814W F606W	11872 1200	3
I2574	IC-2574-1-COPY	10605	10 28 22.9	+68 24 37	0.33	336.13	WFC	2006-03-20	ACS	F814W F555W	900 9568	4
I2574	IC2574-SGS	9755	10 28 43.2	+68 27 06	2.84	21.49	WFC	2004-02-06	ACS	F814W F435W F555W	9568 12000 12800	4
I2574	IC-2574-2	10605	10 27 50.1	+68 22 57	3.57	32.67	WFC	2006-01-27	ACS	F814W F555W	12800 9568	4
Sc22	SCL-DE1	10503	00 23 51.7	-24 42 18	0.00	50.4	WFC	2006-05-13	ACS	F814W F606W F814W	9568 44800 35840	

NOTE. — Entries with reduced precision in the listings for RA and Dec indicate a representative center for dithered observations. Multiple dates for a given field indicate the start times for the earliest and the latest observations of that field. Angular separation refers to separation between the aperture position and the catalog coordinates in Table 1. Field names indicate the titles given in the archive. Observations lacking multiple filters at nearly the same position and alignment are not included. [a] Observations for N4190 were proprietary at the time this paper was submitted; their photometry will be added to the data release when it becomes public. References for published CMDs from the associated data are given in the last column: 1 = Tully et al. (2006); 2 = Dohm-Palmer et al. (2002); 3 = Karachentsev et al. (2006); 4 = Weisz et al. (2008); 5 = Seth et al. (2005a); 6 = Butler et al. (2004); 7 = Rizzi et al. (2006); 8 = Caldwell et al. (1998); 9 = Karachentsev et al. (2001); 10 = Karachentsev et al. (2002c); 11 = Karachentsev et al. (2002b); 12 = Dolphin et al. (2001); 13 = Izotov & Thuan (2002);

TABLE 4  
PHOTOMETRY

Catalog Name	Proposal ID	Target name	Instrument	Filter	Exposure Time (s)	$N_{stars}$	50% Completeness (mag)
Antlia/P29194	10210	ANTLIA	ACS	F606W	985	19207	28.03
Antlia/P29194	10210	ANTLIA	ACS	F814W	1174	19207	27.30
SexA/DDO75	7496	DDO75	WFPC2	F555W	19200	33251	27.34
SexA/DDO75	7496	DDO75	WFPC2	F814W	38400	33251	26.50
N3109	10915	NGC3109-DEEP	WFPC2	F606W	2700	13329	26.76
N3109	10915	NGC3109-DEEP	WFPC2	F814W	3900	13329	26.00
N3109	11307	NGC3109-WIDE1	WFPC2	F606W	2700	21868	26.61
N3109	11307	NGC3109-WIDE1	WFPC2	F814W	3900	21868	25.65
N3109	11307	NGC3109-WIDE2	WFPC2	F606W	2700	30477	26.56
N3109	11307	NGC3109-WIDE2	WFPC2	F814W	3900	30477	25.59
N3109	11307	NGC3109-WIDE3	WFPC2	F606W	2400	34176	26.32
N3109	11307	NGC3109-WIDE3	WFPC2	F814W	2400	34176	25.34
N3109	11307	NGC3109-WIDE4	WFPC2	F606W	2400	42536	26.03
N3109	11307	NGC3109-WIDE4	WFPC2	F814W	2400	42536	25.11
SexB/DDO70	10915	SEXB-DEEP	WFPC2	F606W	2700	29752	26.46
SexB/DDO70	10915	SEXB-DEEP	WFPC2	F814W	3900	29752	25.76
KKR25	8601	KKR25	WFPC2	F606W	600	923	26.13
KKR25	8601	KKR25	WFPC2	F814W	600	923	24.98
KK230	9771	KK230	ACS	F606W	1200	4678	28.20
KK230	9771	KK230	ACS	F814W	900	4678	27.09
E410-005/KK3	10503	ESO410-005	ACS	F606W	8960	92713	28.87
E410-005/KK3	10503	ESO410-005	ACS	F814W	22400	92713	28.18
E294-010	10503	ESO294-010	ACS	F606W	13920	144605	29.09
E294-010	10503	ESO294-010	ACS	F814W	27840	144605	28.25
N55	9765	NGC0055	ACS	F606W	400	436413	25.70
N55	9765	NGC0055	ACS	F814W	676	436413	25.04
N55	9765	NGC0055-DISK	ACS	F606W	676	381466	26.93
N55	9765	NGC0055-DISK	ACS	F814W	700	381466	26.17
N55	10915	NGC0055-DEEP	WFPC2	F606W	6000	17269	27.34
N55	10915	NGC0055-DEEP	WFPC2	F814W	10800	17269	26.38
N55	11307	NGC0055-WIDE1	WFPC2	F606W	2000	37013	26.64
N55	11307	NGC0055-WIDE1	WFPC2	F814W	3700	37013	25.74
N55	11307	NGC0055-WIDE2	WFPC2	F606W	1800	36914	26.17
N55	11307	NGC0055-WIDE2	WFPC2	F814W	2600	36914	25.40
N55	11307	NGC0055-WIDE3	WFPC2	F606W	2700	47547	25.90
N55	11307	NGC0055-WIDE3	WFPC2	F814W	3900	47547	25.13
N55	11307	NGC0055-WIDE4	WFPC2	F606W	2700	55721	25.54
N55	11307	NGC0055-WIDE4	WFPC2	F814W	3900	55721	24.77
N55	11307	NGC0055-WIDE5	WFPC2	F606W	2700	54410	25.52
N55	11307	NGC0055-WIDE5	WFPC2	F814W	3900	54410	24.62
I5152/E237-27	10915	IC5152-DEEP	WFPC2	F606W	4800	325	27.34
I5152/E237-27	10915	IC5152-DEEP	WFPC2	F814W	9600	325	26.45
GR8/DDO155	10915	GR8	ACS	F475W	2244	22146	28.27
GR8/DDO155	10915	GR8	ACS	F814W	2259	22146	27.41
N300	10915	NGC0300-WIDE1	ACS	F475W	1488	201766	27.84
N300	10915	NGC0300-WIDE1	ACS	F606W	1515	224218	27.79
N300	10915	NGC0300-WIDE1	ACS	F814W	1542	224218	27.00
N300	10915	NGC0300-WIDE2	ACS	F475W	1488	314481	27.33
N300	10915	NGC0300-WIDE2	ACS	F606W	1515	363777	27.05
N300	10915	NGC0300-WIDE2	ACS	F814W	1542	363777	26.60
N300	10915	NGC0300-WIDE3	ACS	F475W	1488	407390	26.68
N300	10915	NGC0300-WIDE3	ACS	F606W	1515	453255	26.36
N300	10915	NGC0300-WIDE3	ACS	F814W	1542	453255	25.78
N300	9492	NGC300-1	ACS	F435W	1080	94879	27.51
N300	9492	NGC300-1	ACS	F555W	1080	127007	27.46
N300	9492	NGC300-1	ACS	F814W	1440	127007	27.12
N300	9492	NGC300-2	ACS	F435W	1080	254713	26.99
N300	9492	NGC300-2	ACS	F555W	1080	385059	26.84
N300	9492	NGC300-2	ACS	F814W	1440	385059	26.22
N300	9492	NGC300-3	ACS	F435W	1080	253701	26.71
N300	9492	NGC300-3	ACS	F555W	1080	384389	26.50
N300	9492	NGC300-3	ACS	F814W	1440	384389	25.73
N300	9492	NGC300-4	ACS	F435W	1080	72656	27.52
N300	9492	NGC300-4	ACS	F555W	1080	95916	27.49
N300	9492	NGC300-4	ACS	F814W	1440	95916	27.17
N300	9492	NGC300-5	ACS	F435W	1080	159598	27.30
N300	9492	NGC300-5	ACS	F555W	1080	246163	27.23
N300	9492	NGC300-5	ACS	F814W	1440	246163	26.82
N300	9492	NGC300-6	ACS	F435W	1080	72479	27.46
N300	9492	NGC300-6	ACS	F555W	1080	111786	27.42
N300	9492	NGC300-6	ACS	F814W	1440	111786	27.09
UA438	8192	E407-G18	WFPC2	F606W	600	5016	26.04
UA438	8192	E407-G18	WFPC2	F814W	600	5016	24.98
DDO187	10210	UGC9128	ACS	F606W	985	27608	28.02

TABLE 4 — *Continued*

Catalog Name	Proposal ID	Target name	Instrument	Filter	Exposure Time (s)	$N_{stars}$	50% Completeness (mag)
DDO187	10210	UGC9128	ACS	F814W	1174	27608	27.12
KKH98	10915	KKH98	ACS	F475W	2265	10915	28.28
KKH98	10915	KKH98	ACS	F814W	2280	10915	27.48
DDO125/U7577	8601	UGC7577	WFPC2	F606W	600	11520	26.01
DDO125/U7577	8601	UGC7577	WFPC2	F814W	600	11520	24.96
U8508	10915	UGC8508	ACS	F475W	2280	45938	28.04
U8508	10915	UGC8508	ACS	F814W	2349	45938	27.45
KKH86	8601	KKH71	WFPC2	F606W	600	727	26.22
KKH86	8601	KKH71	WFPC2	F814W	600	727	25.06
DDO99/U6817	8601	UGC6817	WFPC2	F606W	600	6536	26.16
DDO99/U6817	8601	UGC6817	WFPC2	F814W	600	6536	25.00
DDO190/U9240	10915	DDO190	ACS	F475W	2274	95311	28.01
DDO190/U9240	10915	DDO190	ACS	F606W	2301	105886	28.25
DDO190/U9240	10915	DDO190	ACS	F814W	2265	105886	27.22
DDO113/KDG90	10915	DDO113	ACS	F475W	2265	21120	28.27
DDO113/KDG90	10915	DDO113	ACS	F814W	2280	21120	27.43
N4214	10915	NGC4214-DEEP	WFPC2	F606W	15600	16781	27.85
N4214	10915	NGC4214-DEEP	WFPC2	F814W	31200	16781	26.93
DDO181/U8651	10210	UGC8651	ACS	F606W	1016	41869	28.04
DDO181/U8651	10210	UGC8651	ACS	F814W	1209	41869	27.18
N3741	10915	NGC3741	ACS	F475W	2262	29511	28.06
N3741	10915	NGC3741	ACS	F814W	2331	29511	27.31
N4163	10915	NGC4163	ACS	F475W	2265	81531	28.04
N4163	10915	NGC4163	ACS	F606W	2292	97645	28.14
N4163	10915	NGC4163	ACS	F814W	2250	97645	27.24
N4163	9771	NGC4163	ACS	F606W	1200	76156	27.91
N4163	9771	NGC4163	ACS	F814W	900	76156	26.94
N404	10915	NGC0404-DEEP	WFPC2	F606W	39000	40663	27.19
N404	10915	NGC0404-DEEP	WFPC2	F814W	75400	40663	26.55
UA292	10915	UGCA292	ACS	F475W	2250	9451	28.34
UA292	10915	UGCA292	ACS	F606W	926	8919	27.89
UA292	10915	UGCA292	ACS	F814W	2274	8919	27.42
U8833	10210	UGC8833	ACS	F606W	998	19441	27.93
U8833	10210	UGC8833	ACS	F814W	1189	19441	27.22
DDO183/U8760	10210	UGC8760	ACS	F606W	998	36824	27.86
DDO183/U8760	10210	UGC8760	ACS	F814W	1189	36824	27.08
N2366	10605	NGC-2366-1	ACS	F555W	4780	250218	28.01
N2366	10605	NGC-2366-1	ACS	F814W	4780	250218	27.38
N2366	10605	NGC-2366-2	ACS	F555W	4780	237663	28.10
N2366	10605	NGC-2366-2	ACS	F814W	4780	237663	27.49
DDO44/KK61	10915	DDO44	ACS	F475W	2361	34602	28.35
DDO44/KK61	10915	DDO44	ACS	F814W	2430	34602	27.61
DDO44/KK61	8137	DDO44	WFPC2	F555W	12800	10687	27.58
DDO44/KK61	8137	DDO44	WFPC2	F814W	11900	10687	26.46
DDO44/KK61	8192	KK061	WFPC2	F606W	600	1794	26.04
DDO44/KK61	8192	KK061	WFPC2	F814W	600	1794	24.86
E321-014	8601	PGC39032	WFPC2	F606W	600	1745	26.01
E321-014	8601	PGC39032	WFPC2	F814W	600	1745	24.88
U4483	8769	UGC4483	WFPC2	F555W	9500	6634	27.66
U4483	8769	UGC4483	WFPC2	F814W	6900	6634	26.43
N2403	10182	SN-NGC2403-PR	ACS	F475W	1200	317104	26.41
N2403	10182	SN-NGC2403-PR	ACS	F606W	700	405516	26.18
N2403	10182	SN-NGC2403-PR	ACS	F814W	700	405516	25.54
N2403	10579	NGC2403-X1	ACS	F435W	1248	154761	26.91
N2403	10579	NGC2403-X1	ACS	F606W	1248	154761	26.44
N2403	10523	NGC2403-HALO-1	ACS	F606W	710	101951	27.65
N2403	10523	NGC2403-HALO-1	ACS	F814W	710	101951	26.80
N2403	10523	NGC2403-HALO-6	ACS	F606W	720	25350	27.60
N2403	10523	NGC2403-HALO-6	ACS	F814W	720	25350	26.92
N2403	10915	NGC2403-DEEP	WFPC2	F606W	32400	30452	27.81
N2403	10915	NGC2403-DEEP	WFPC2	F814W	62100	30452	27.01
DDO6	10915	DDO6	ACS	F475W	2250	23825	28.36
DDO6	10915	DDO6	ACS	F814W	2268	23825	27.57
HoIX/DDO66	10605	UGC-5336	ACS	F555W	4768	57578	28.46
HoIX/DDO66	10605	UGC-5336	ACS	F814W	4768	57578	27.92
HoI/DDO63	10605	UGC-5139	ACS	F555W	4446	124090	28.38
HoI/DDO63	10605	UGC-5139	ACS	F814W	5936	124090	27.88
KKH37/Mai16	10915	KKH37	ACS	F475W	2469	15359	28.35
KKH37/Mai16	10915	KKH37	ACS	F814W	2541	15359	27.69
KKH37/Mai16	9771	KKH37	ACS	F606W	1200	12677	27.95
KKH37/Mai16	9771	KKH37	ACS	F814W	900	12677	27.03
HoII/DDO50	10605	UGC-4305-1	ACS	F555W	4660	248026	27.99
HoII/DDO50	10605	UGC-4305-1	ACS	F814W	4660	248026	27.33
HoII/DDO50	10605	UGC-4305-2	ACS	F555W	4660	228107	28.01

TABLE 4 — *Continued*

Catalog Name	Proposal ID	Target name	Instrument	Filter	Exposure Time (s)	$N_{stars}$	50% Completeness (mag)
HoII/DDO50	10605	UGC-4305-2	ACS	F814W	4660	228107	27.44
KDG2/E540-030	10503	ESO540-030	ACS	F606W	6720	18333	28.79
KDG2/E540-030	10503	ESO540-030	ACS	F814W	6720	18333	27.93
MCG9-20-131	10905	CGCG-269-049	WFPC2	F606W	2200	2505	26.99
MCG9-20-131	10905	CGCG-269-049	WFPC2	F814W	2400	2505	25.93
E540-032/FG24	10503	ESO540-032	ACS	F606W	8960	35910	28.97
E540-032/FG24	10503	ESO540-032	ACS	F814W	4480	35910	27.83
FM1	9884	M81F6D1	ACS	F606W	17200	19390	28.92
FM1	9884	M81F6D1	ACS	F814W	9000	19390	27.85
KK77	9884	M81F12D1	ACS	F606W	17200	58994	29.04
KK77	9884	M81F12D1	ACS	F814W	9000	58994	28.03
KDG63/KK83	9884	DDO71	ACS	F606W	17200	57160	29.04
KDG63/KK83	9884	DDO71	ACS	F814W	9000	57160	28.05
M82	10776	M82-POS1	ACS	F435W	1800	8523	27.48
M82	10776	M82-POS1	ACS	F555W	1360	33232	27.28
M82	10776	M82-POS1	ACS	F814W	700	33232	26.48
M82	10776	M82-POS2	ACS	F435W	1800	54178	26.63
M82	10776	M82-POS2	ACS	F555W	1360	137107	26.42
M82	10776	M82-POS2	ACS	F814W	700	137107	25.95
M82	10776	M82-POS3	ACS	F435W	1800	55872	27.19
M82	10776	M82-POS3	ACS	F555W	1360	156710	26.81
M82	10776	M82-POS3	ACS	F814W	700	156710	26.11
M82	10776	M82-POS4	ACS	F435W	1800	8177	27.50
M82	10776	M82-POS4	ACS	F555W	1360	31893	27.32
M82	10776	M82-POS4	ACS	F814W	700	31893	26.41
M82	10776	M82-POS5	ACS	F435W	1800	36981	27.06
M82	10776	M82-POS5	ACS	F555W	1360	104935	26.57
M82	10776	M82-POS5	ACS	F814W	700	104935	25.99
M82	10776	M82-POS6	ACS	F435W	1800	46755	27.21
M82	10776	M82-POS6	ACS	F555W	1360	129659	26.95
M82	10776	M82-POS6	ACS	F814W	700	129659	26.16
KDG52	10605	MESSIER-081-DWARF-A	ACS	F555W	5914	20435	28.55
KDG52	10605	MESSIER-081-DWARF-A	ACS	F814W	5936	20435	28.05
DDO53	10605	UGC-04459	ACS	F555W	4768	80119	28.34
DDO53	10605	UGC-04459	ACS	F814W	4768	80119	27.74
N2976	10915	NGC2976-DEEP	ACS	F475W	2418	27361	28.23
N2976	10915	NGC2976-DEEP	ACS	F606W	18716	105461	29.17
N2976	10915	NGC2976-DEEP	ACS	F814W	27091	105461	28.59
N2976	10915	NGC2976-WIDE1	ACS	F475W	1570	188324	27.35
N2976	10915	NGC2976-WIDE1	ACS	F606W	1596	316439	27.11
N2976	10915	NGC2976-WIDE1	ACS	F814W	1622	316439	26.54
KDG61/KK81	9884	M81K61	ACS	F606W	17200	80821	29.09
KDG61/KK81	9884	M81K61	ACS	F814W	9000	80821	28.05
M81	10523	NGC3031-HALO-1	ACS	F606W	710	10375	27.83
M81	10523	NGC3031-HALO-1	ACS	F814W	710	10375	26.87
M81	10523	NGC3031-HALO-2	ACS	F606W	735	2680	27.85
M81	10523	NGC3031-HALO-2	ACS	F814W	735	2680	26.93
M81	9796	M81-X-9	ACS	F435W	2520	4848	28.08
M81	9796	M81-X-9	ACS	F555W	1160	5197	27.70
M81	9796	M81-X-9	ACS	F814W	1160	5197	27.22
M81	10584	M81-FIELD-1	ACS	F435W	1565	9534	27.72
M81	10584	M81-FIELD-1	ACS	F606W	1580	84602	28.01
M81	10584	M81-FIELD-1	ACS	F814W	1595	84602	27.19
M81	10584	M81-FIELD-2	ACS	F435W	1565	19150	27.81
M81	10584	M81-FIELD-2	ACS	F606W	1580	119824	28.09
M81	10584	M81-FIELD-2	ACS	F814W	1595	119824	27.19
M81	10584	M81-FIELD-3	ACS	F435W	1200	12825	27.67
M81	10584	M81-FIELD-3	ACS	F606W	1200	12825	27.56
M81	10584	M81-FIELD-4	ACS	F435W	1200	42735	27.53
M81	10584	M81-FIELD-4	ACS	F606W	1200	42735	27.39
M81	10584	M81-FIELD-5	ACS	F435W	1200	58025	27.51
M81	10584	M81-FIELD-5	ACS	F606W	1200	58025	27.39
M81	10584	M81-FIELD-6	ACS	F435W	1200	19854	27.57
M81	10584	M81-FIELD-6	ACS	F606W	1200	19854	27.35
M81	10584	M81-FIELD-7	ACS	F435W	1200	25519	27.51
M81	10584	M81-FIELD-7	ACS	F606W	1200	25519	27.38
M81	10584	M81-FIELD-8	ACS	F435W	1200	120692	27.34
M81	10584	M81-FIELD-8	ACS	F606W	1200	120692	26.99
M81	10584	M81-FIELD-9	ACS	F435W	1200	103579	27.34
M81	10584	M81-FIELD-9	ACS	F606W	1200	103579	27.03
M81	10584	M81-FIELD-10	ACS	F435W	1200	23952	27.53
M81	10584	M81-FIELD-10	ACS	F606W	1200	23952	27.37
M81	10584	M81-FIELD-11	ACS	F435W	1200	64075	27.46
M81	10584	M81-FIELD-11	ACS	F606W	1200	64075	27.19
M81	10584	M81-FIELD-12	ACS	F435W	1200	95023	27.19

TABLE 4 — *Continued*

Catalog Name	Proposal ID	Target name	Instrument	Filter	Exposure Time (s)	$N_{stars}$	50% Completeness (mag)
M81	10584	M81-FIELD-12	ACS	F606W	1200	95023	26.76
M81	10584	M81-FIELD-13	ACS	F435W	1200	100686	27.24
M81	10584	M81-FIELD-13	ACS	F606W	1200	100686	26.79
M81	10584	M81-FIELD-14	ACS	F435W	1200	44962	27.54
M81	10584	M81-FIELD-14	ACS	F606W	1200	44962	27.37
M81	10584	M81-FIELD-15	ACS	F435W	1200	48598	27.39
M81	10584	M81-FIELD-15	ACS	F606W	1200	48598	27.21
M81	10584	M81-FIELD-16	ACS	F435W	1200	117662	27.14
M81	10584	M81-FIELD-16	ACS	F606W	1200	117662	26.45
M81	10584	M81-FIELD-17	ACS	F435W	1200	121250	27.12
M81	10584	M81-FIELD-17	ACS	F606W	1200	121250	26.51
M81	10584	M81-FIELD-18	ACS	F435W	1200	71560	27.43
M81	10584	M81-FIELD-18	ACS	F606W	1200	71560	27.21
M81	10584	M81-FIELD-19	ACS	F435W	1200	46881	27.52
M81	10584	M81-FIELD-19	ACS	F606W	1200	46881	27.14
M81	10584	M81-FIELD-20	ACS	F435W	1200	73677	27.31
M81	10584	M81-FIELD-20	ACS	F606W	1200	73677	26.95
M81	10584	M81-FIELD-21	ACS	F435W	1200	68530	27.29
M81	10584	M81-FIELD-21	ACS	F606W	1200	68530	26.91
M81	10584	M81-FIELD-22	ACS	F435W	1200	28643	27.57
M81	10584	M81-FIELD-22	ACS	F606W	1200	28643	27.42
M81	10584	M81-FIELD-23	ACS	F435W	1200	27747	27.59
M81	10584	M81-FIELD-23	ACS	F606W	1200	27747	27.49
M81	10584	M81-FIELD-24	ACS	F435W	1200	65543	27.53
M81	10584	M81-FIELD-24	ACS	F606W	1200	65543	27.35
M81	10584	M81-FIELD-25	ACS	F435W	1200	66215	27.47
M81	10584	M81-FIELD-25	ACS	F606W	1200	66215	27.23
M81	10584	M81-FIELD-26	ACS	F435W	1200	13045	27.65
M81	10584	M81-FIELD-26	ACS	F606W	1200	13045	27.36
M81	10584	M81-FIELD-27	ACS	F435W	1565	18484	27.53
M81	10584	M81-FIELD-27	ACS	F606W	1580	135993	27.98
M81	10584	M81-FIELD-27	ACS	F814W	1595	135993	27.26
M81	10584	M81-FIELD-28	ACS	F435W	1565	25018	27.67
M81	10584	M81-FIELD-28	ACS	F606W	1580	189968	28.00
M81	10584	M81-FIELD-28	ACS	F814W	1595	189968	27.16
M81	10584	M81-FIELD-29	ACS	F435W	1565	7337	27.67
M81	10584	M81-FIELD-29	ACS	F606W	1580	80917	28.07
M81	10584	M81-FIELD-29	ACS	F814W	1595	80917	27.33
M81	10915	M81-DEEP	ACS	F475W	2418	24403	28.38
M81	10915	M81-DEEP	ACS	F606W	24132	171085	29.78
M81	10915	M81-DEEP	ACS	F814W	29853	171085	29.06
N247	10915	NGC0247-WIDE1	ACS	F475W	2253	127347	28.18
N247	10915	NGC0247-WIDE1	ACS	F606W	2280	193375	28.05
N247	10915	NGC0247-WIDE1	ACS	F814W	2250	193375	27.23
N247	10915	NGC0247-WIDE2	ACS	F475W	1480	256673	27.59
N247	10915	NGC0247-WIDE2	ACS	F606W	1507	365102	27.41
N247	10915	NGC0247-WIDE2	ACS	F814W	1534	365102	26.75
N247	10915	NGC0247-WIDE3	ACS	F475W	1480	313441	27.25
N247	10915	NGC0247-WIDE3	ACS	F606W	1507	428443	26.99
N247	10915	NGC0247-WIDE3	ACS	F814W	1534	428443	26.35
HoIX/DDO66	10605	UGC-5336	ACS	F555W	4768	57578	28.46
HoIX/DDO66	10605	UGC-5336	ACS	F814W	4768	57578	27.92
KDG64/KK85	9884	M81K64	ACS	F606W	17200	68437	29.26
KDG64/KK85	9884	M81K64	ACS	F814W	9000	68437	28.42
IKN	9771	IKN	ACS	F606W	1200	24617	28.03
IKN	9771	IKN	ACS	F814W	900	24617	26.97
KDG73	10915	KDG73	ACS	F475W	2250	7915	28.42
KDG73	10915	KDG73	ACS	F814W	2274	7915	27.65
DDO78/KK89	10915	DDO78	ACS	F475W	2274	36488	28.23
DDO78/KK89	10915	DDO78	ACS	F814W	2292	36488	27.55
F8D1	5898	GAL-094447+672619	WFPC2	F555W	9000	14226	27.84
F8D1	5898	GAL-094447+672619	WFPC2	F814W	15200	14226	27.05
F8D1	5898	GAL-094447+672619	WFPC2	F555W	9000	11274	27.78
F8D1	5898	GAL-094447+672619	WFPC2	F814W	11400	11274	26.92
BK5N	5898	GAL-100441+681522	WFPC2	F555W	5400	2602	27.67
BK5N	5898	GAL-100441+681522	WFPC2	F814W	11400	2602	27.02
BK5N	6964	GAL-100441+681522	WFPC2	F555W	15600	2332	27.78
BK5N	6964	GAL-100441+681522	WFPC2	F814W	21340	2332	26.95
N3077	9381	NGC3077-PHOENIX	ACS	F435W	6000	64463	28.72
N3077	9381	NGC3077-PHOENIX	ACS	F555W	9600	170978	28.87
N3077	9381	NGC3077-PHOENIX	ACS	F814W	19200	170978	28.35
N3077	10915	NGC3077-WIDE1	ACS	F475W	1570	260710	27.25
N3077	10915	NGC3077-WIDE1	ACS	F606W	1596	441992	26.91
N3077	10915	NGC3077-WIDE1	ACS	F814W	1622	441992	26.04
HoII/DDO50	10605	UGC-4305-1	ACS	F555W	4660	248026	27.99

TABLE 4 — *Continued*

Catalog Name	Proposal ID	Target name	Instrument	Filter	Exposure Time (s)	$N_{stars}$	50% Completeness (mag)
HoII/DDO50	10605	UGC-4305-1	ACS	F814W	4660	248026	27.33
HoII/DDO50	10605	UGC-4305-2	ACS	F555W	4660	228107	28.01
HoII/DDO50	10605	UGC-4305-2	ACS	F814W	4660	228107	27.44
HoIX/DDO66	10605	UGC-5336	ACS	F555W	4768	57578	28.46
HoIX/DDO66	10605	UGC-5336	ACS	F814W	4768	57578	27.92
HoI/DDO63	10605	UGC-5139	ACS	F555W	4446	124090	28.38
HoI/DDO63	10605	UGC-5139	ACS	F814W	5936	124090	27.88
A0952+69	10915	A0952+69	ACS	F475W	2250	7829	28.39
A0952+69	10915	A0952+69	ACS	F814W	2265	7829	27.66
N253	10915	NGC0253-WIDE1	ACS	F475W	2256	172461	28.13
N253	10915	NGC0253-WIDE1	ACS	F606W	2283	293245	28.03
N253	10915	NGC0253-WIDE1	ACS	F814W	2253	293245	27.26
N253	10915	NGC0253-WIDE2	ACS	F475W	1482	295259	27.40
N253	10915	NGC0253-WIDE2	ACS	F606W	1508	435887	27.19
N253	10915	NGC0253-WIDE2	ACS	F814W	1534	435887	26.50
N253	10915	NGC0253-WIDE3	ACS	F475W	1482	242556	26.75
N253	10915	NGC0253-WIDE3	ACS	F606W	1508	427580	26.63
N253	10915	NGC0253-WIDE3	ACS	F814W	1534	427580	25.83
N253	10915	NGC0253-WIDE4	ACS	F475W	1482	285492	26.39
N253	10915	NGC0253-WIDE4	ACS	F606W	1508	418057	26.24
N253	10915	NGC0253-WIDE4	ACS	F814W	1534	418057	25.37
N253	10915	NGC0253-WIDE5	ACS	F475W	1482	232863	25.71
N253	10915	NGC0253-WIDE5	ACS	F606W	1508	348386	25.65
N253	10915	NGC0253-WIDE5	ACS	F814W	1534	348386	24.66
N253	10523	NGC0253-HALO-11	ACS	F606W	680	28390	27.50
N253	10523	NGC0253-HALO-11	ACS	F814W	680	28390	26.62
HS117	9771	HS117	ACS	F606W	1200	7308	28.03
HS117	9771	HS117	ACS	F814W	900	7308	27.10
DDO82	10915	DDO82	ACS	F475W	2400	106760	28.18
DDO82	10915	DDO82	ACS	F606W	2454	172897	28.21
DDO82	10915	DDO82	ACS	F814W	2442	172897	27.58
BK3N	10915	BK3N	ACS	F475W	2250	8180	28.43
BK3N	10915	BK3N	ACS	F814W	2265	8180	27.61
I2574	10605	IC-2574-1-COPY	ACS	F555W	4784	285585	27.95
I2574	10605	IC-2574-1-COPY	ACS	F814W	4784	285585	27.34
I2574	10605	IC-2574-2	ACS	F555W	4784	157937	28.26
I2574	10605	IC-2574-2	ACS	F814W	4784	157937	27.74
I2574	9755	IC2574-SGS	ACS	F435W	6000	292177	28.29
I2574	9755	IC2574-SGS	ACS	F555W	6400	358327	28.23
I2574	9755	IC2574-SGS	ACS	F814W	6400	358327	27.63
Sc22	10503	SCL-DE1	ACS	F606W	17920	77241	29.10
Sc22	10503	SCL-DE1	ACS	F814W	17920	77241	28.41

NOTE. — Exposure times may differ from those in Table 3 when individual fields were unusable.



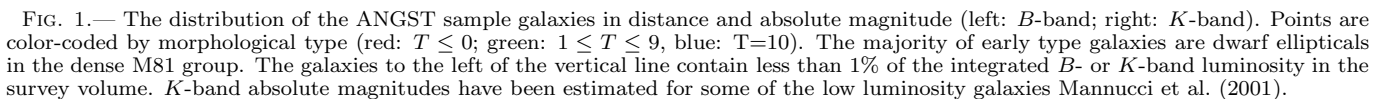
TABLE 5  
TRGB MEASUREMENTS

Catalog Name	Target Name	Filters	$N_{stars}$	$A_V$	Mean Color	$M_{TRGB}$ (F814W)	$m_{TRGB}$ (raw)	$m_{TRGB}$	$(m - M)_0$	$D$ (Mpc)
Antlia	ANTLIA	F606W,F814W	169	0.243	1.05	-4.04	21.642	$21.503 \pm 0.011$	25.546	$1.29 \pm 0.015$
SexA	DDO75	F555W,F814W	276	0.139	1.34	-3.95	21.835	$21.756 \pm 0.033$	25.705	$1.38 \pm 0.050$
N3109	NGC3109-WIDE1	F606W,F814W	355	0.201	1.04	-4.00	21.608	$21.493 \pm 0.018$	25.498	$1.26 \pm 0.025$
N3109	NGC3109-DEEP	F606W,F814W	263	0.201	1.01	-3.98	21.687	$21.572 \pm 0.014$	25.551	$1.29 \pm 0.019$
SexB	SEXB-DEEP	F606W,F814W	754	0.095	0.98	-3.95	21.824	$21.770 \pm 0.024$	25.720	$1.39 \pm 0.036$
KKR25	KKR25	F606W,F814W	80	0.027	1.00	-3.96	22.479	$22.464 \pm 0.022$	26.428	$1.93 \pm 0.047$
KK230	KK230	F606W,F814W	47	0.043	1.00	-4.00	22.492	$22.467 \pm 0.026$	26.472	$1.97 \pm 0.055$
E410-005	ESO410-005	F606W,F814W	194	0.042	1.06	-4.05	22.493	$22.469 \pm 0.042$	26.514	$2.01 \pm 0.090$
E294-010	ESO294-010	F606W,F814W	95	0.018	1.06	-4.05	22.397	$22.386 \pm 0.008$	26.434	$1.94 \pm 0.017$
N55	NGC0055-WIDE1	F606W,F814W	1075	0.041	1.11	-4.00	22.650	$22.626 \pm 0.013$	26.622	$2.11 \pm 0.029$
N55	NGC0055-WIDE2	F606W,F814W	1278	0.041	1.12	-3.99	22.658	$22.635 \pm 0.020$	26.629	$2.12 \pm 0.045$
N55	NGC0055-DEEP	F606W,F814W	323	0.041	1.06	-4.01	22.615	$22.591 \pm 0.011$	26.604	$2.09 \pm 0.025$
N55	NGC0055-DISK	F606W,F814W	7829	0.041	1.17	-4.02	22.590	$22.566 \pm 0.014$	26.586	$2.08 \pm 0.031$
GR8	GR8	F475W,F814W	367	0.080	2.27	-4.03	22.607	$22.561 \pm 0.010$	26.588	$2.08 \pm 0.022$
N300	NGC0300-WIDE1	F475W,F814W	865	0.039	2.67	-4.02	22.493	$22.471 \pm 0.035$	26.486	$1.98 \pm 0.076$
N300	NGC0300-WIDE1	F606W,F814W	1366	0.039	1.33	-4.02	22.519	$22.497 \pm 0.015$	26.518	$2.01 \pm 0.033$
N300	NGC300-5	F435W,F814W	829	0.039	3.40	-4.02	22.421	$22.399 \pm 0.014$	26.421	$1.92 \pm 0.029$
N300	NGC300-5	F555W,F814W	858	0.039	1.85	-4.02	22.437	$22.415 \pm 0.014$	26.435	$1.94 \pm 0.029$
N300	NGC300-6	F435W,F814W	760	0.039	3.41	-4.02	22.527	$22.505 \pm 0.014$	26.527	$2.02 \pm 0.031$
N300	NGC300-6	F555W,F814W	753	0.039	1.81	-4.02	22.531	$22.508 \pm 0.023$	26.531	$2.02 \pm 0.051$
UA438	E407-G18	F606W,F814W	715	0.045	1.05	-4.01	22.708	$22.683 \pm 0.038$	26.690	$2.18 \pm 0.091$
DDO187	UGC9128	F606W,F814W	459	0.071	1.03	-4.03	22.732	$22.692 \pm 0.028$	26.717	$2.21 \pm 0.068$
KKH98	KKH98	F475W,F814W	294	0.385	2.23	-4.04	23.207	$22.988 \pm 0.012$	27.023	$2.54 \pm 0.033$
DDO125	UGC7577	F606W,F814W	1990	0.064	1.07	-4.01	23.081	$23.045 \pm 0.023$	27.057	$2.58 \pm 0.065$
U8508	UGC8508	F475W,F814W	738	0.047	2.23	-4.03	23.050	$23.024 \pm 0.011$	27.058	$2.58 \pm 0.032$
KKH86	KKH71	F606W,F814W	108	0.083	1.01	-3.98	23.134	$23.087 \pm 0.068$	27.063	$2.59 \pm 0.189$
DDO99	UGC6817	F606W,F814W	668	0.081	0.99	-3.96	23.152	$23.106 \pm 0.059$	27.068	$2.59 \pm 0.166$
DDO190	DDO190	F606W,F814W	1267	0.038	1.06	-4.05	23.205	$23.184 \pm 0.014$	27.230	$2.79 \pm 0.042$
DDO113	DDO113	F475W,F814W	706	0.063	2.16	-4.05	23.337	$23.302 \pm 0.026$	27.349	$2.95 \pm 0.083$
N4214	NGC4214-DEEP	F606W,F814W	563	0.068	1.13	-3.99	23.464	$23.426 \pm 0.015$	27.414	$3.04 \pm 0.048$
DDO181	UGC8651	F606W,F814W	637	0.019	1.03	-4.03	23.472	$23.462 \pm 0.015$	27.487	$3.14 \pm 0.053$
N3741	NGC3741	F475W,F814W	987	0.077	2.18	-4.05	23.552	$23.509 \pm 0.037$	27.554	$3.24 \pm 0.130$
N4163	NGC4163	F475W,F814W	1650	0.062	2.39	-4.02	23.300	$23.264 \pm 0.014$	27.283	$2.86 \pm 0.043$
N4163	NGC4163	F606W,F814W	1513	0.062	1.11	-4.03	23.298	$23.263 \pm 0.013$	27.296	$2.88 \pm 0.040$
N404	NGC0404-DEEP	F606W,F814W	2104	0.181	1.25	-3.99	23.538	$23.434 \pm 0.013$	27.423	$3.05 \pm 0.042$
UA292	UGCA292	F475W,F814W	166	0.048	1.92	-3.98	23.841	$23.813 \pm 0.023$	27.792	$3.62 \pm 0.091$
UA292	UGCA292	F606W,F814W	112	0.048	0.98	-3.98	23.834	$23.806 \pm 0.019$	27.790	$3.61 \pm 0.076$
U8833	UGC8833	F606W,F814W	522	0.037	1.04	-4.04	23.431	$23.410 \pm 0.020$	27.446	$3.08 \pm 0.067$
DDO183	UGC8760	F606W,F814W	604	0.051	1.05	-4.04	23.527	$23.498 \pm 0.039$	27.542	$3.22 \pm 0.135$
N2366	NGC-2366-2	F555W,F814W	2566	0.113	1.50	-4.05	23.555	$23.490 \pm 0.014$	27.535	$3.21 \pm 0.048$
DDO44	DDO44	F475W,F814W	811	0.129	2.26	-4.03	23.499	$23.426 \pm 0.015$	27.454	$3.10 \pm 0.051$
E321-014	PGC39032	F606W,F814W	320	0.293	1.04	-4.00	23.672	$23.505 \pm 0.066$	27.509	$3.18 \pm 0.227$
U4483	UGC4483	F555W,F814W	302	0.105	1.34	-3.94	23.782	$23.722 \pm 0.032$	27.666	$3.41 \pm 0.117$
N2403	NGC2403-DEEP	F606W,F814W	629	0.124	1.11	-4.00	23.593	$23.522 \pm 0.009$	27.519	$3.19 \pm 0.029$
N2403	NGC2403-HALO-1	F606W,F814W	2369	0.124	1.21	-4.02	23.573	$23.503 \pm 0.039$	27.524	$3.20 \pm 0.134$
N2403	NGC2403-HALO-6	F606W,F814W	805	0.124	1.20	-4.02	23.497	$23.426 \pm 0.018$	27.447	$3.09 \pm 0.059$
DDO6	DDO6	F475W,F814W	647	0.053	2.17	-4.05	23.580	$23.550 \pm 0.017$	27.597	$3.31 \pm 0.059$
KKH37	KKH37	F475W,F814W	748	0.231	2.27	-4.03	23.671	$23.540 \pm 0.037$	27.566	$3.26 \pm 0.130$
HoII	UGC-4305-2	F555W,F814W	2461	0.098	1.53	-4.04	23.666	$23.610 \pm 0.013$	27.646	$3.38 \pm 0.047$
KDG2	E540-030	F606W,F814W	179	0.072	1.04	-4.04	23.613	$23.571 \pm 0.009$	27.612	$3.33 \pm 0.033$
MCG9-20-1	CGCG-269-049	F606W,F814W	46	0.076	1.05	-4.01	22.051	$22.007 \pm 0.025$	26.014	$1.60 \pm 0.043^a$
E540-032	E540-032	F606W,F814W	408	0.064	1.07	-4.05	23.733	$23.696 \pm 0.020$	27.743	$3.54 \pm 0.077$
FM1	M81F6D1	F606W,F814W	636	0.241	1.16	-4.02	23.855	$23.718 \pm 0.010$	27.737	$3.53 \pm 0.039$
KK77	M81F12D1	F606W,F814W	1061	0.442	1.16	-4.02	23.982	$23.730 \pm 0.013$	27.749	$3.55 \pm 0.051$

TABLE 5 — *Continued*

Catalog Name	Target Name	Filters	$N_{stars}$	$A_V$	Mean Color	$M_{TRGB}$ (F814W)	$m_{TRGB}$ (raw)	$m_{TRGB}$	$(m - M)_0$	$D$ (Mpc)
KDG63	DDO71	F606W,F814W	959	0.303	1.11	-4.03	23.881	$23.708 \pm 0.019$	27.740	$3.53 \pm 0.074$
M82	M82-POS4	F435W,F814W	203	0.191	3.62	-4.00	23.642	$23.533 \pm 0.023$	27.534	$3.21 \pm 0.078$
M82	M82-POS4	F555W,F814W	564	0.191	1.91	-4.01	23.831	$23.722 \pm 0.018$	27.737	$3.53 \pm 0.068$
KDG52	MESSIER-081-DWARF-A	F555W,F814W	330	0.063	1.45	-4.04	23.675	$23.639 \pm 0.024$	27.680	$3.44 \pm 0.090$
DDO53	UGC-04459	F555W,F814W	953	0.118	1.48	-4.05	23.806	$23.739 \pm 0.012$	27.786	$3.61 \pm 0.046$
N2976	N2976-DEEP	F475W,F814W	1334	0.224	2.65	-4.02	23.864	$23.736 \pm 0.009$	27.754	$3.55 \pm 0.033$
N2976	N2976-DEEP	F606W,F814W	1340	0.224	1.24	-4.02	23.865	$23.738 \pm 0.007$	27.762	$3.57 \pm 0.029$
KDG61	M81K61	F606W,F814W	1124	0.226	1.14	-4.02	23.823	$23.694 \pm 0.042$	27.716	$3.49 \pm 0.161$
M81	NGC3031-HALO-1	F606W,F814W	227	0.249	1.29	-4.02	23.833	$23.691 \pm 0.029$	27.715	$3.49 \pm 0.109$
M81	M81-FIELD-29	F435W,F814W	551	0.249	3.40	-4.02	23.899	$23.758 \pm 0.017$	27.780	$3.60 \pm 0.068$
M81	M81-FIELD-29	F606W,F814W	330	0.249	1.39	-4.01	23.896	$23.754 \pm 0.018$	27.768	$3.58 \pm 0.069$
M81	M81-DEEP	F606W,F814W	198	0.249	1.35	-4.02	23.890	$23.748 \pm 0.008$	27.767	$3.58 \pm 0.029$
N247	NGC0247-WIDE1	F475W,F814W	2640	0.056	2.64	-4.02	23.735	$23.703 \pm 0.036$	27.723	$3.50 \pm 0.138$
N247	NGC0247-WIDE1	F606W,F814W	3349	0.056	1.30	-4.02	23.753	$23.722 \pm 0.031$	27.745	$3.54 \pm 0.117$
HoIX	UGC-5336	F555W,F814W	273	0.244	1.78	-4.02	23.906	$23.767 \pm 0.037$	27.790	$3.61 \pm 0.144$
KDG64	M81K64	F606W,F814W	951	0.165	1.10	-4.04	23.907	$23.813 \pm 0.009$	27.852	$3.72 \pm 0.036$
IKN	IKN	F606W,F814W	1926	0.181	1.19	-4.02	23.869	$23.766 \pm 0.019$	27.786	$3.61 \pm 0.075$
KDG73	KDG73	F475W,F814W	345	0.056	2.08	-4.04	24.022	$23.991 \pm 0.020$	28.027	$4.03 \pm 0.086$
DDO78	DDO78	F475W,F814W	1494	0.066	2.38	-4.02	23.837	$23.799 \pm 0.017$	27.818	$3.66 \pm 0.069$
F8D1	GAL-094447+672619_302	F555W,F814W	1355	0.328	1.68	-3.99	24.018	$23.831 \pm 0.020$	27.817	$3.66 \pm 0.078$
BK5N	GAL-100441+681522_355	F555W,F814W	251	0.195	1.47	-4.01	23.814	$23.703 \pm 0.022$	27.715	$3.49 \pm 0.082$
N3077	NGC3077-PHOENIX	F555W,F814W	333	0.208	1.94	-4.01	24.026	$23.908 \pm 0.009$	27.919	$3.83 \pm 0.036$
HoI	UGC-5139	F555W,F814W	2086	0.153	1.54	-4.03	24.006	$23.918 \pm 0.012$	27.953	$3.90 \pm 0.050$
A0952+69	A0952+69	F475W,F814W	176	0.259	2.20	-4.04	23.994	$23.847 \pm 0.024$	27.888	$3.78 \pm 0.098$
N253	NGC0253-HALO-11	F606W,F814W	1193	0.058	1.23	-4.02	23.710	$23.677 \pm 0.064$	27.700	$3.47 \pm 0.239$
N253	NGC0253-WIDE1	F475W,F814W	2188	0.058	2.63	-4.02	23.712	$23.678 \pm 0.017$	27.698	$3.46 \pm 0.065$
N253	NGC0253-WIDE1	F606W,F814W	3269	0.058	1.26	-4.02	23.667	$23.634 \pm 0.025$	27.658	$3.40 \pm 0.091$
HS117	HS117	F606W,F814W	556	0.359	1.08	-4.05	24.066	$23.862 \pm 0.017$	27.908	$3.82 \pm 0.070$
DDO82	DDO82	F475W,F814W	4180	0.133	2.51	-4.02	23.952	$23.876 \pm 0.013$	27.899	$3.80 \pm 0.054$
DDO82	DDO82	F606W,F814W	4594	0.133	1.16	-4.02	23.956	$23.880 \pm 0.016$	27.899	$3.80 \pm 0.065$
BK3N	BK3N	F475W,F814W	235	0.246	2.50	-4.02	24.051	$23.911 \pm 0.013$	27.934	$3.86 \pm 0.054$
I2574	IC-2574-2	F555W,F814W	2425	0.112	1.58	-4.02	23.973	$23.909 \pm 0.014$	27.931	$3.86 \pm 0.057$
I2574	IC2574-SGS	F435W,F814W	5638	0.112	3.11	-4.02	23.936	$23.872 \pm 0.013$	27.892	$3.79 \pm 0.055$
I2574	IC2574-SGS	F555W,F814W	5100	0.112	1.61	-4.02	23.937	$23.874 \pm 0.013$	27.893	$3.79 \pm 0.052$
Sc22	SCL-DE1	F606W,F814W	124	0.046	1.02	-4.02	24.116	$24.090 \pm 0.023$	28.110	$4.19 \pm 0.105$

NOTE. — Color-dependent absolute magnitudes for the TRGB are taken from Girardi et al. (2008) isochrones. Mean colors are for the stars used to measure the TRGB, which are not necessarily all RGB stars, and include only stars within  $0.2^m$  of the TRGB.  $A_V$  values are as reported by IRSA for coordinates in Table 1, with the exception of M82. Extinction corrections from  $A_V$  to the observed filters are adopted from Girardi et al. (2008), as described in the text.  $m_{TRGB}$  was measured in the least crowded region of each galaxy. Measured distances for A0952+69, BK3N, and Holmberg IX are dominated by outer M81 stars, rather than RGB stars associated with the named galaxies. Listed uncertainties are dominated by photometric uncertainties and by stochasticity in the number of stars near the tip; systematic uncertainties (due to uncertainties in the assumed TRGB absolute magnitudes and extinction) are likely to be much larger, but are not included in the listed uncertainties. [a] The distance to MCG9-20-1 is ambiguous, as it was not clear if the observed tip was for the RGB or AGB; the true distance modulus may potentially be significantly fainter.



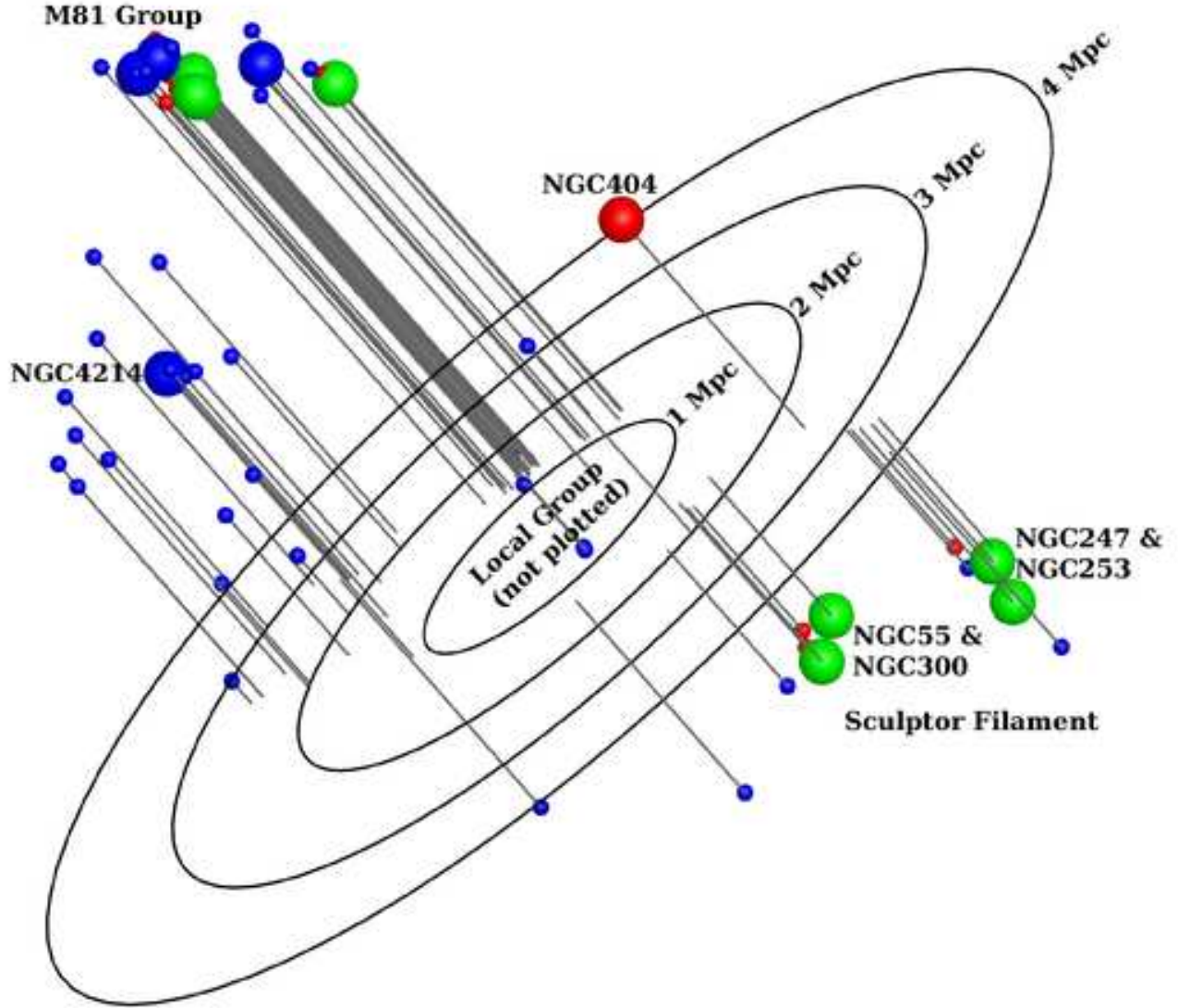


FIG. 2.— The 3-dimensional space distribution of the ANGST sample galaxies. Galaxies are color-coded by morphological type (red:  $T \leq 0$ ; green:  $1 \leq T \leq 9$ , blue:  $T=10$ ), as in Figure 1. Larger symbols indicate galaxies brighter than  $M_B = -16.0$ . The large clump of galaxies in the upper left is the rich M81 group. The two clumps under the plane along the right hand axis are the closer NGC 55/NGC 300 clump and the more distant NGC 247/NGC 253 subclump along the Sculptor filament. The bright galaxy at the center of the dwarf cloud on the left is NGC 4214, and the bright isolated early-type galaxy to the right is NGC 404. The circles are drawn at intervals of 1 Mpc, along the equatorial plane. Distances are taken from Table 5. Note that not all galaxies within 4 Mpc are plotted, due to ANGST's  $|b| > 20^\circ$  selection criteria.

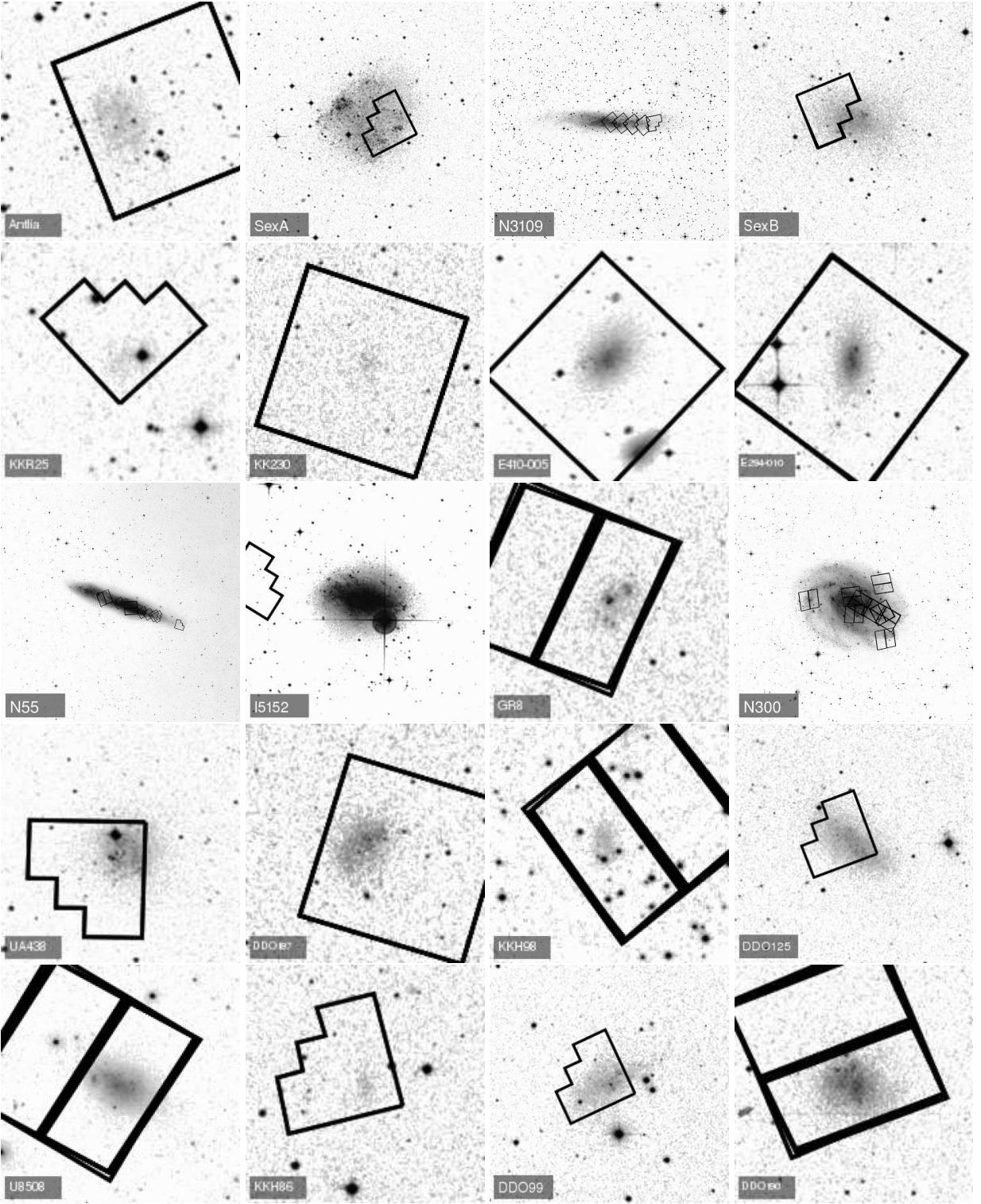


FIG. 3.— Field positions of images included in (Table 2 & 3). Figures are ordered from the upper left to the bottom right. (a) Antlia; (b) SexA; (c) N3109; (d) SexB; (e) KKR25; (f) KK230; (g) E410-005; (h) E294-010; (i) N55; (j) I5152; (k) GR8; (l) N300; (m) UA438; (n) DDO187; (o) KKH98; (p) DDO125; (q) U8508; (r) KKH86; (s) DDO99; (t) DDO190;

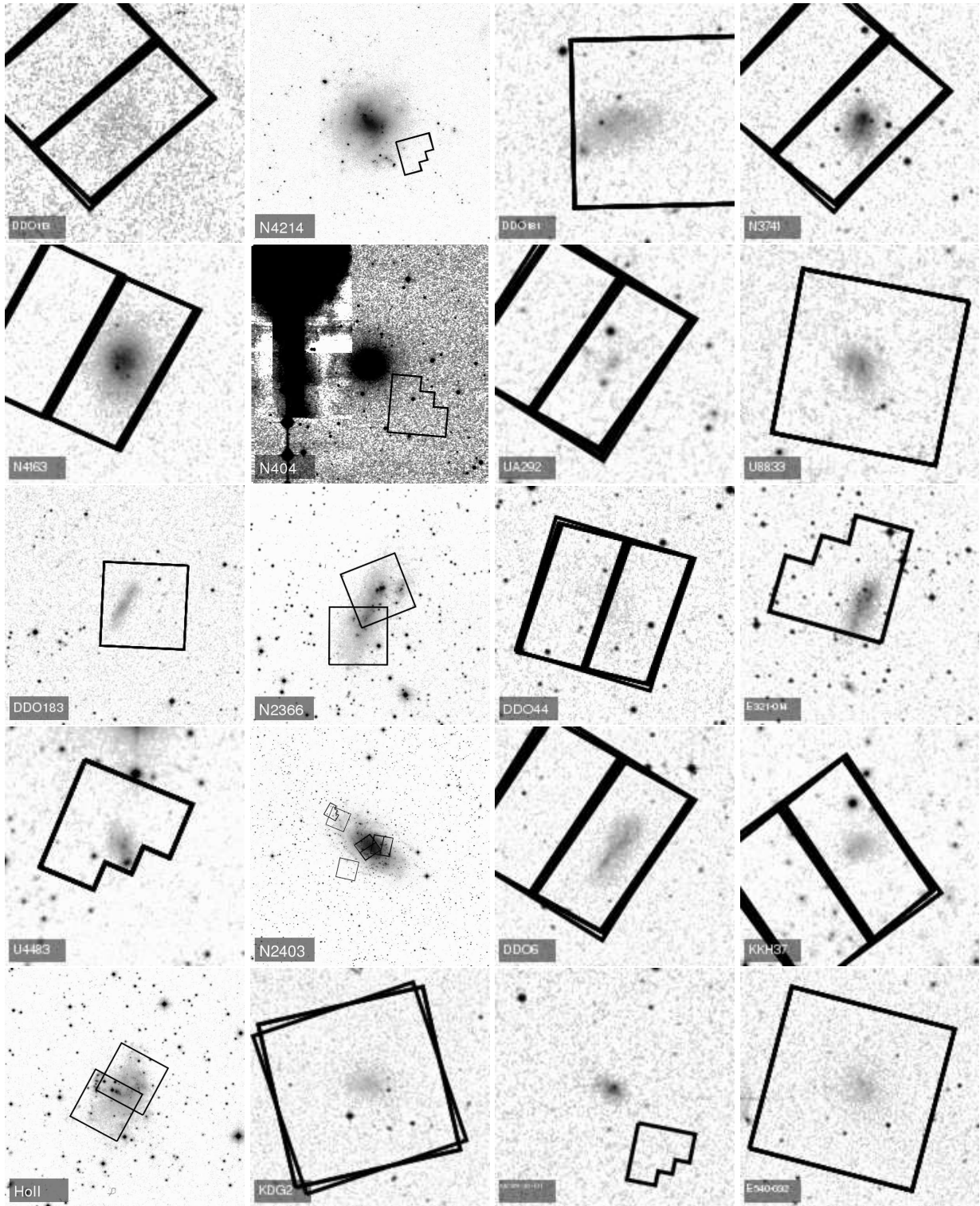


FIG. 4.— Field positions of images included in Table 2 & 3, as described in Figure 3. Figures are ordered from the upper left to the bottom right. (a) DDO113; (b) N4214; (c) DDO181; (d) N3741; (e) N4163; (f) N404; (g) UA292; (h) U8833; (i) DDO183; (j) N2366; (k) DDO44; (l) E321-014; (m) U4483; (n) N2403; (o) DDO6; (p) KKH37; (q) HoII; (r) KDG2; (s) MCG9-20-131; (t) E540-032;



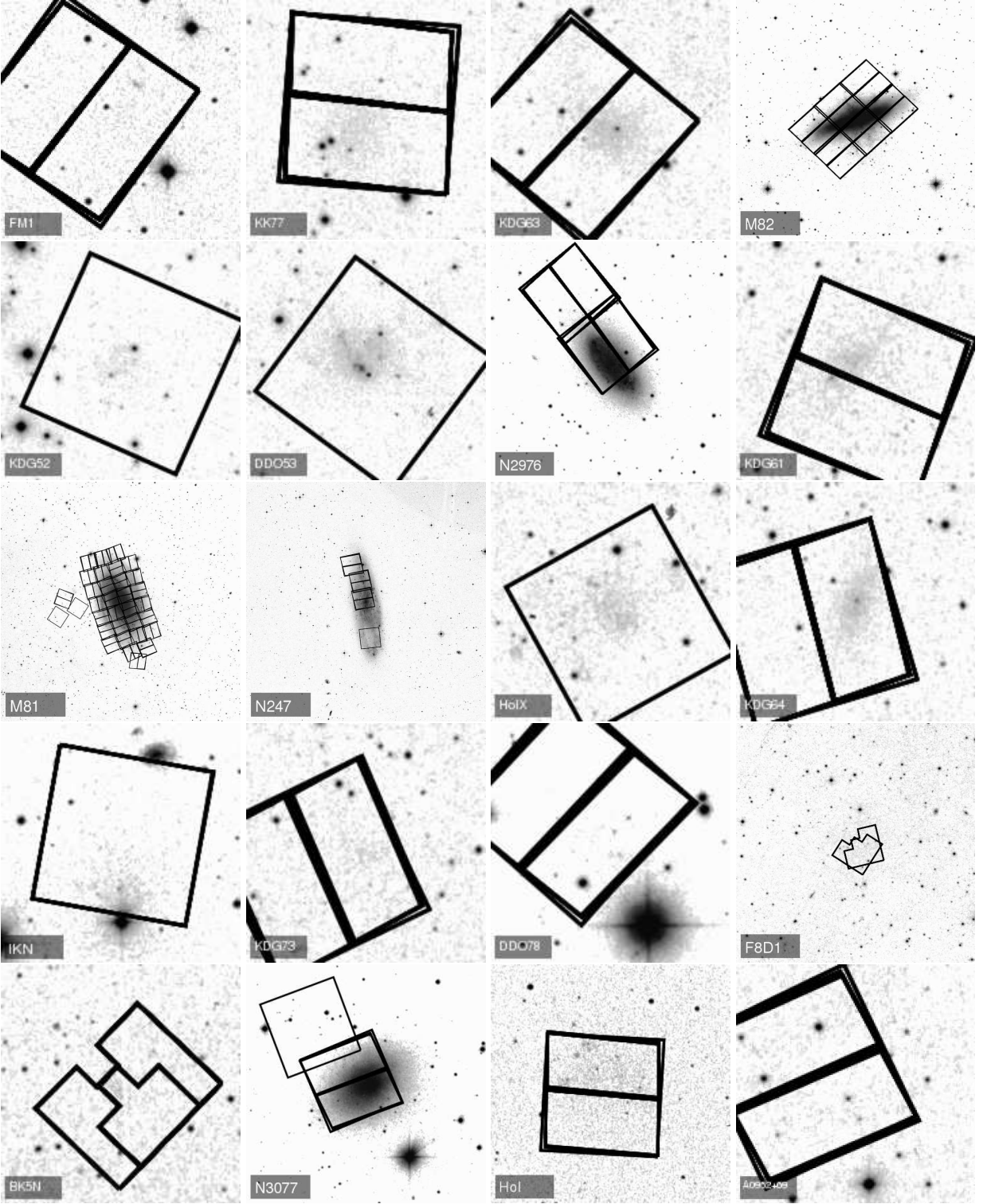


FIG. 5.— Field positions of images included in Table 2 & 3, as described in Figure 3. Figures are ordered from the upper left to the bottom right. (a) FM1; (b) KK77; (c) KDG63; (d) M82; (e) KDG52; (f) DDO53; (g) N2976; (h) KDG61; (i) M81; (j) N247; (k) HoIX; (l) KDG64; (m) IKN; (n) KDG73; (o) DDO78; (p) F8D1; (q) BK5N; (r) N3077; (s) HoI; (t) A0952+69;

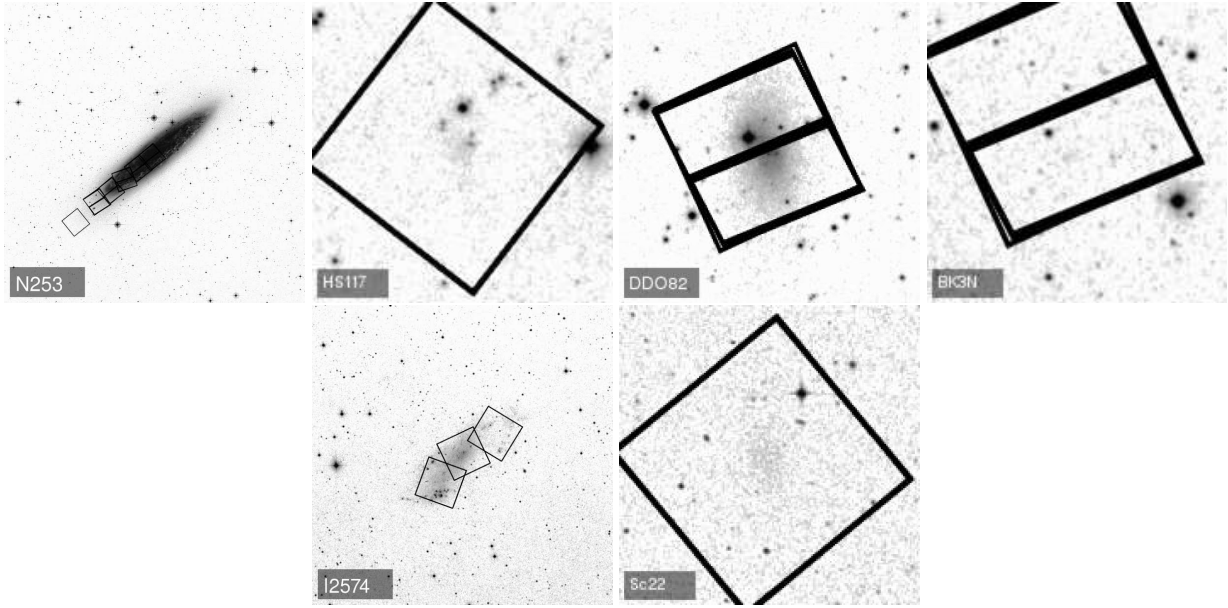


FIG. 6.— Field positions of images included in Table 2 & 3, as described in Figure 3. Figures are ordered from the upper left to the bottom right. (a) N253; (b) HS117; (c) DDO82; (d) BK3N; (e) I2574; (f) Sc22;

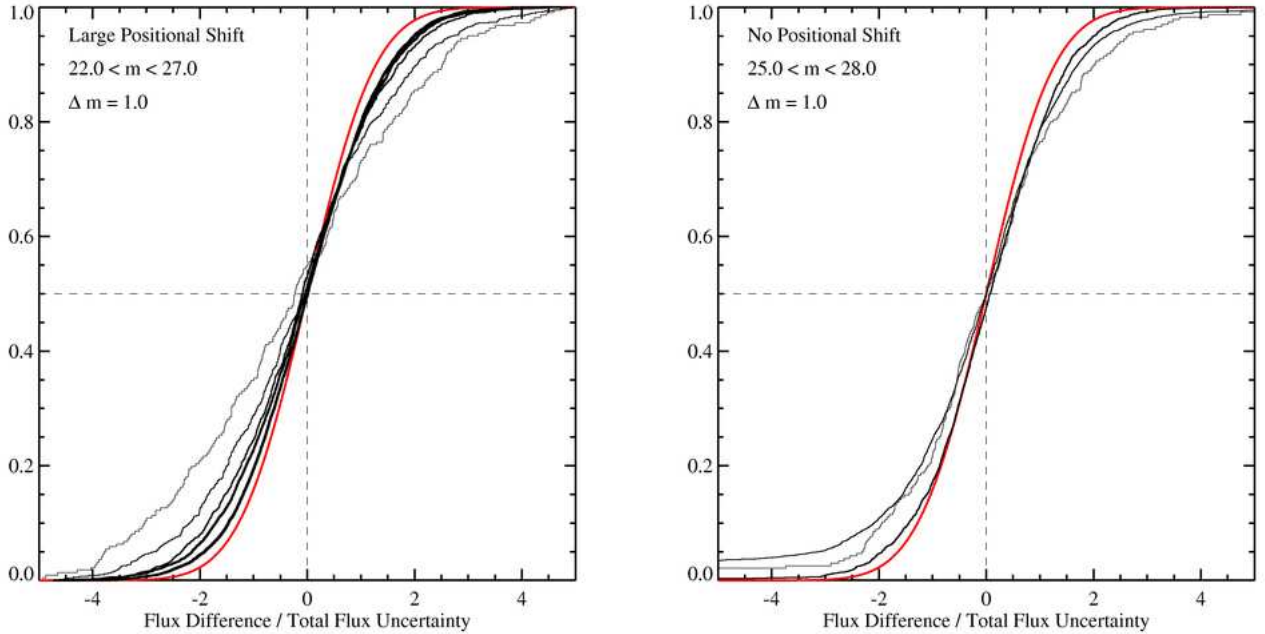


FIG. 7.— The cumulative distribution of  $F814W$  magnitude differences between stars measured in two widely separated but overlapping ACS exposures between NGC 300's WIDE1 and WIDE2 (left), and between stars measured in successive 1-orbit ACS exposures at the same pointing in M81's deep field (right). Magnitude differences are scaled by the reported magnitude error for each star, added in quadrature for the case of repeat measurements. The distributions are calculated in bins of 1 magnitude, with the heaviest line indicating the faintest bin. The red curve indicates the expectation for a perfect Gaussian error distribution. In both cases, the distribution of errors is only slightly broader than a Gaussian, and systematic errors are swamped by photometric uncertainties.



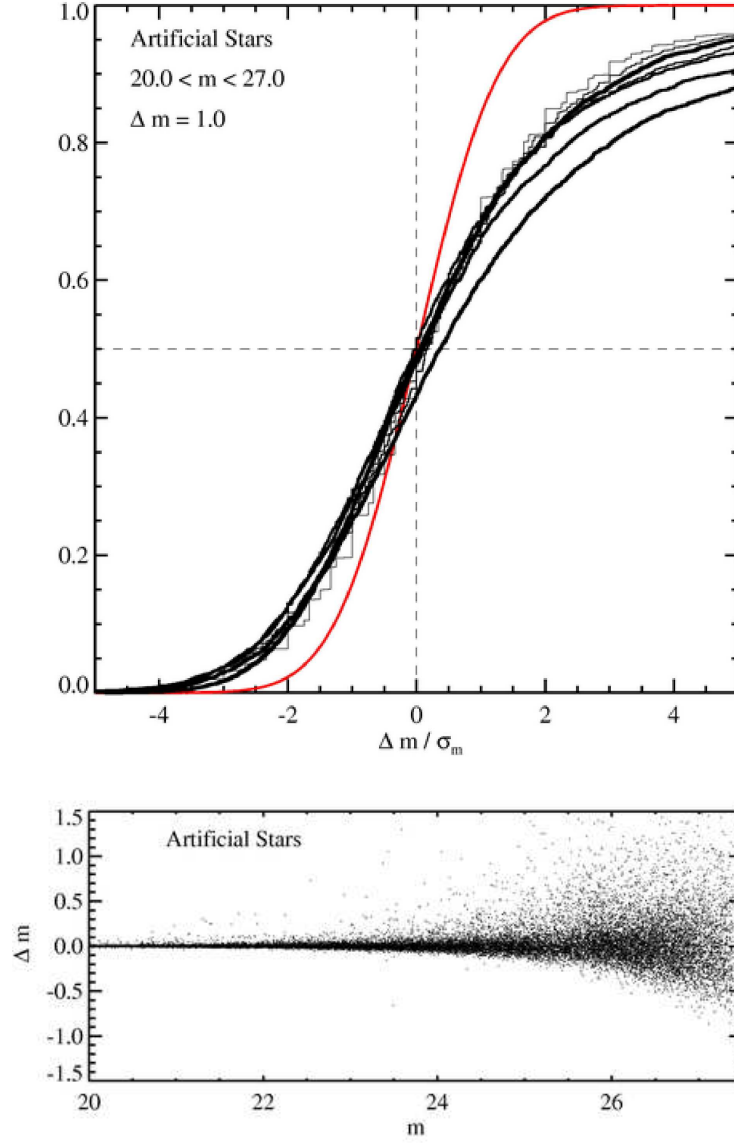


FIG. 8.— The cumulative distribution of  $F814W$  magnitude differences between the true and recovered magnitudes in artificial stars from the same overlap region from NGC 300's WIDE1. The top panel shows the cumulative distribution of magnitude differences, scaled by the reported magnitude error for each star, added in quadrature for the case of repeat measurements. The distributions are calculated in bins of 1 magnitude wide, with the heaviest line indicating the faintest bin. The red curve indicates the expectation for a perfect Gaussian error distribution. The bottom panel shows the the measured magnitude differences as a function of magnitude. Recovered magnitudes tend to be somewhat brighter than true magnitudes, due to blending with fainter unresolved sources.

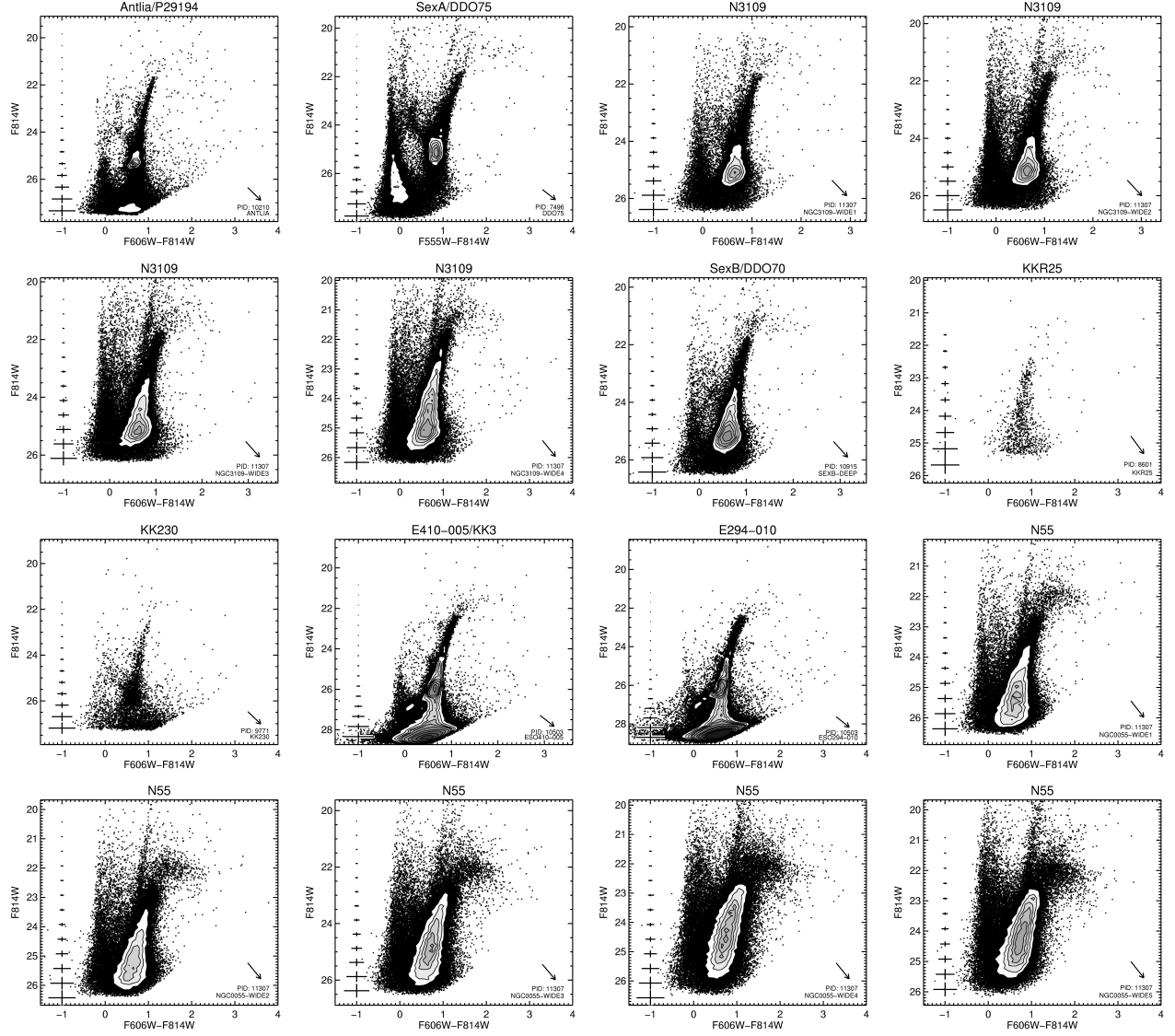


FIG. 9.— CMDs of galaxies in the ANGST data release (Table 2 & 3), using photometry from the conservative *\*\_gst* catalogs. Stars are plotted as individual points in regions of the CMD with few stars, and are plotted as a Hess diagram otherwise. The lower right of each plot shows the HST proposal ID and target name, and an arrow indicating the direction of the reddening vector. The ANGST/CNG Catalog name is given at the top of each plot. Error bars on the left indicate typical photometric errors in each magnitude bin, but do not include systematic errors derived from artificial star tests. Galaxies are ordered as in Table 1. Some fields have multiple CMDs, showing all possible filter combinations on the color axis (e.g.,  $F475W - F606W$ ,  $F475W - F814W$ ,  $F606W - F814W$ ). Figures are ordered from the upper left to the bottom right. (a) Antlia; (b) SexA; (c) N3109; (d) N3109; (e) N3109; (f) N3109; (g) SexB; (h) KKR25; (i) KK230; (j) E410-005; (k) E294-010; (l) N55; (m) N55; (n) N55; (o) N55; (p) N55;

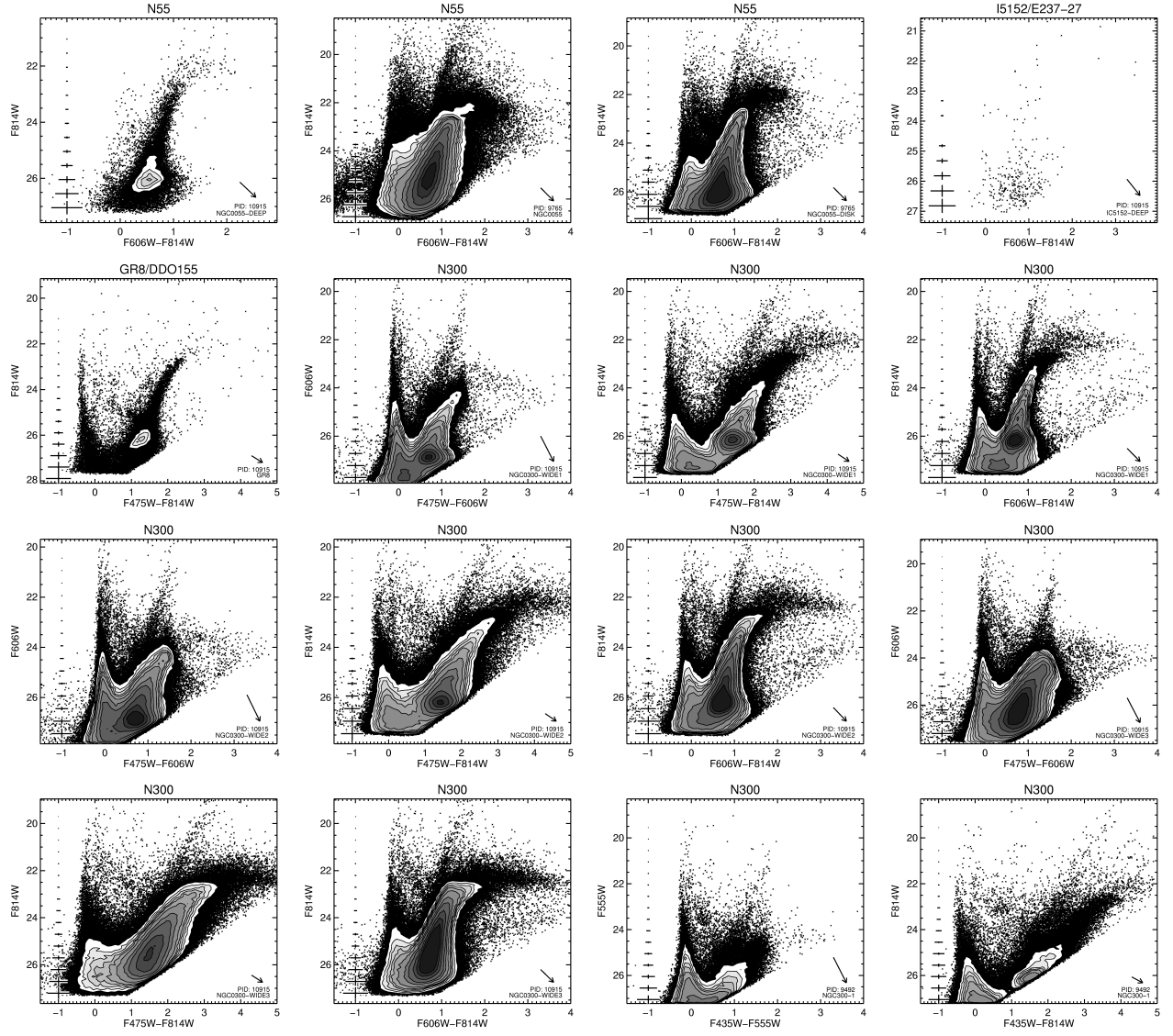


FIG. 10.— CMDs of galaxies in the ANGST data release, as described in Figure 9. Figures are ordered from the upper left to the bottom right. (a) N55; (b) N55; (c) N55; (d) I5152; (e) GR8; (f) N300; (g) N300; (h) N300; (i) N300; (j) N300; (k) N300; (l) N300; (m) N300; (n) N300; (o) N300; (p) N300;

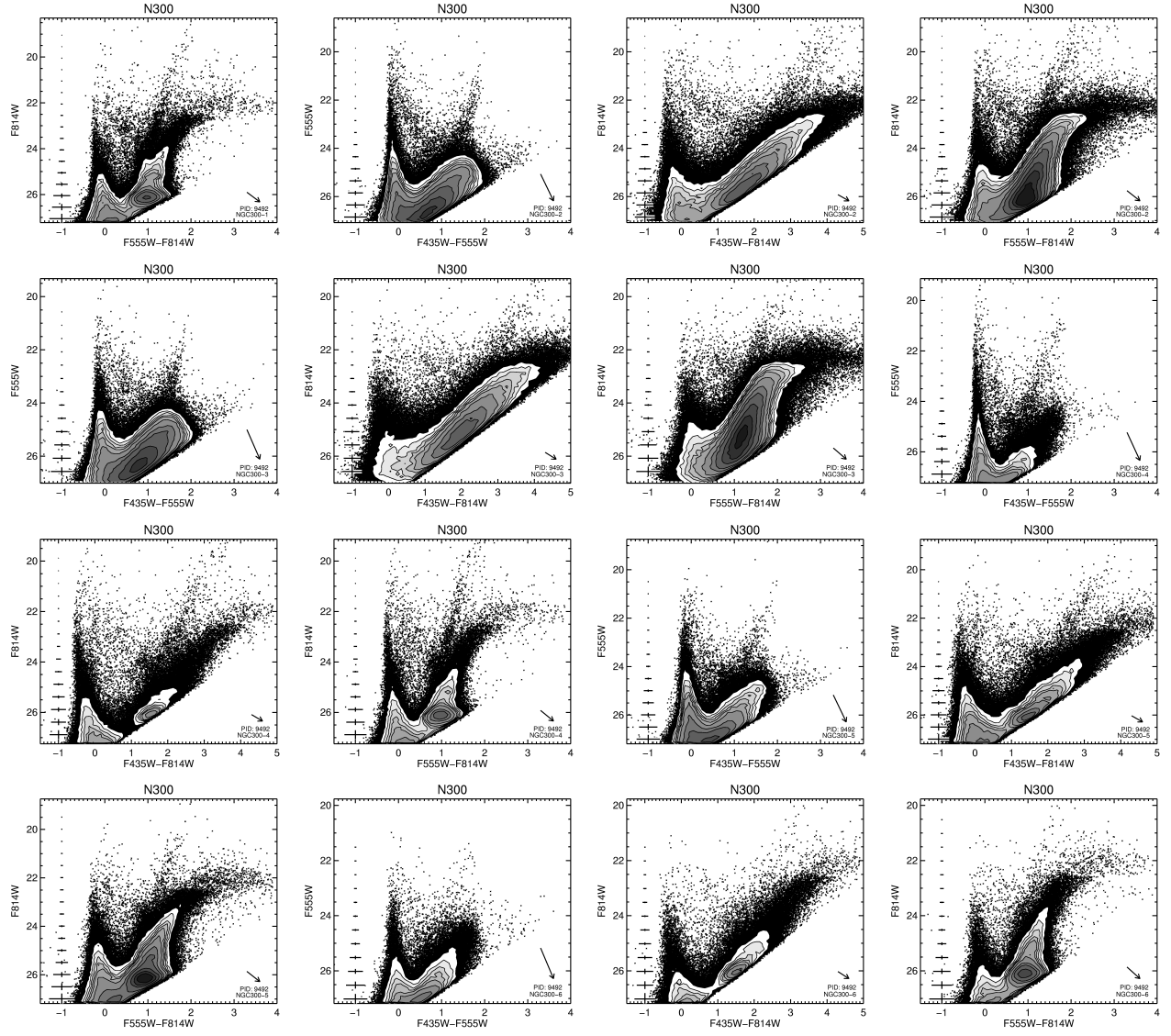


FIG. 11.— CMDs of galaxies in the ANGST data release, as described in Figure 9. Figures are ordered from the upper left to the bottom right. (a) N300; (b) N300; (c) N300; (d) N300; (e) N300; (f) N300; (g) N300; (h) N300; (i) N300; (j) N300; (k) N300; (l) N300; (m) N300; (n) N300; (o) N300; (p) N300;

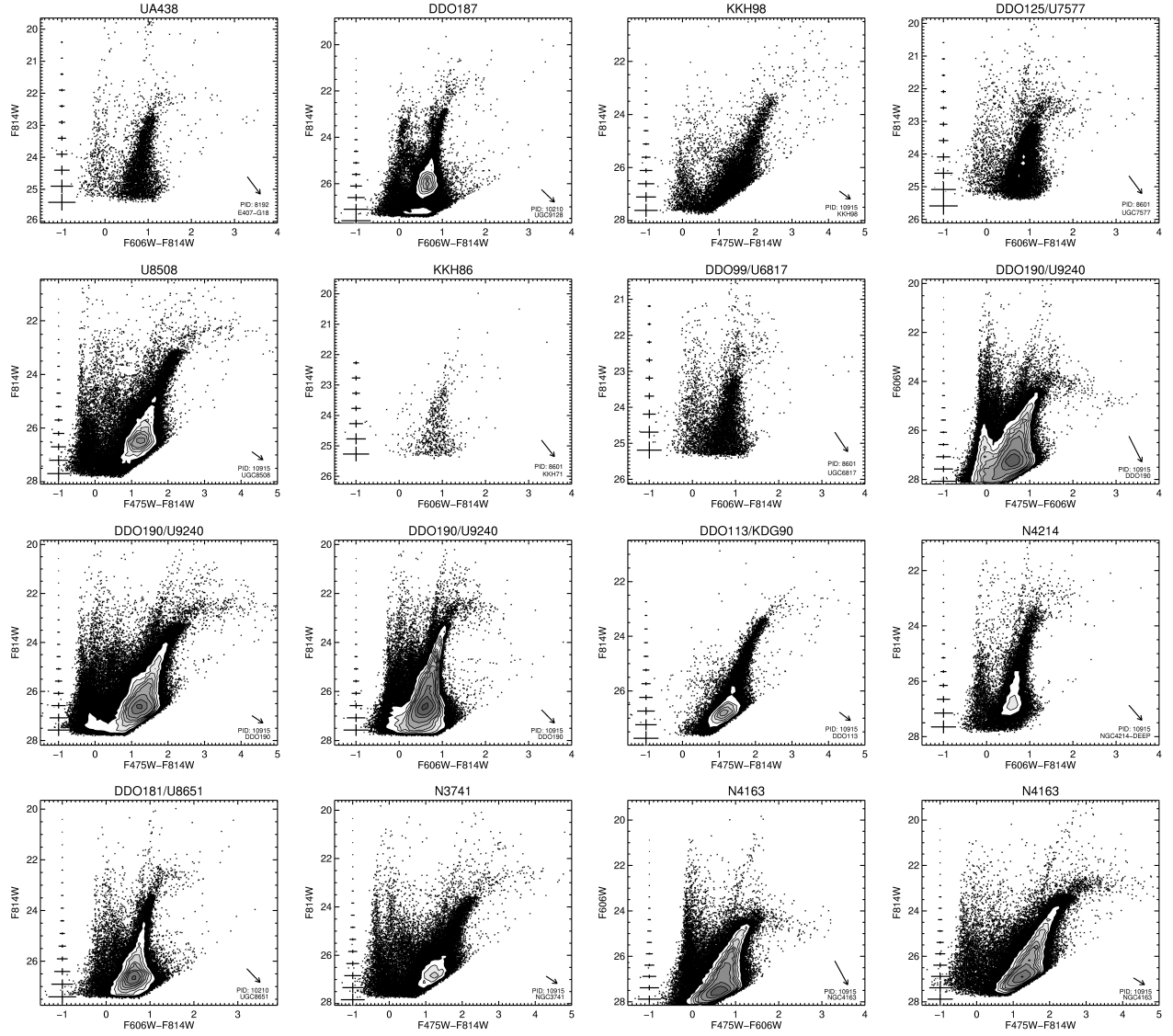


FIG. 12.— CMDs of galaxies in the ANGST data release, as described in Figure 9. Figures are ordered from the upper left to the bottom right. (a) UA438; (b) DDO187; (c) KKH98; (d) DDO125; (e) U8508; (f) KKH86; (g) DDO99; (h) DDO190; (i) DDO190; (j) DDO190; (k) DDO113; (l) N4214; (m) DDO181; (n) N3741; (o) N4163; (p) N4163;

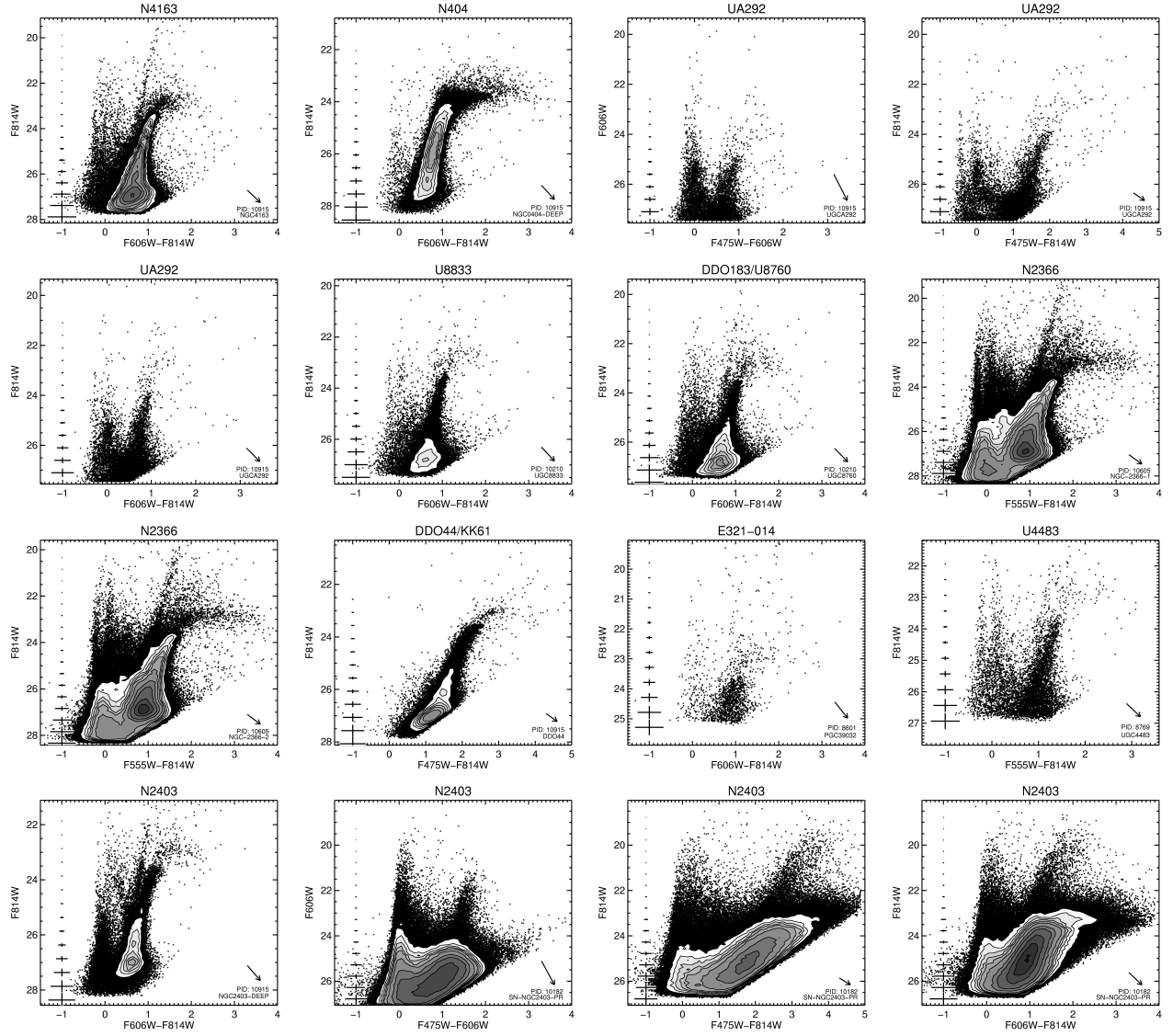


FIG. 13.— CMDs of galaxies in the ANGST data release, as described in Figure 9. Figures are ordered from the upper left to the bottom right. (a) N4163; (b) N404; (c) UA292; (d) UA292; (e) UA292; (f) U8833; (g) DDO183; (h) N2366; (i) N2366; (j) DDO44; (k) E321-014; (l) U4483; (m) N2403; (n) N2403; (o) N2403; (p) N2403;

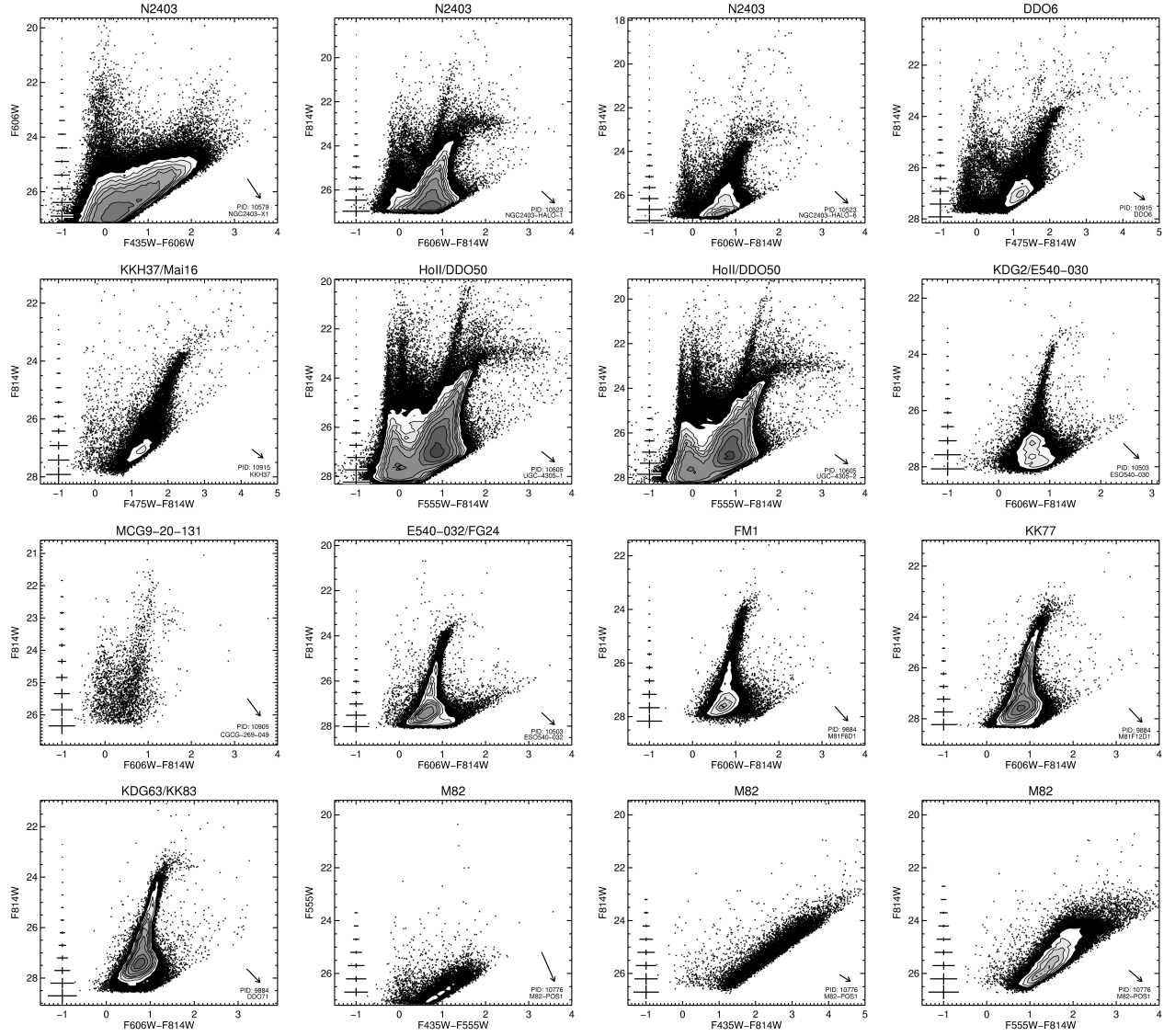


FIG. 14.— CMDs of galaxies in the ANGST data release, as described in Figure 9. Figures are ordered from the upper left to the bottom right. (a) N2403; (b) N2403; (c) N2403; (d) DDO6; (e) KKH37; (f) HolI; (g) HolI; (h) KDG2; (i) MCG9-20-131; (j) E540-032; (k) FM1; (l) KK77; (m) KDG63; (n) M82; (o) M82; (p) M82;

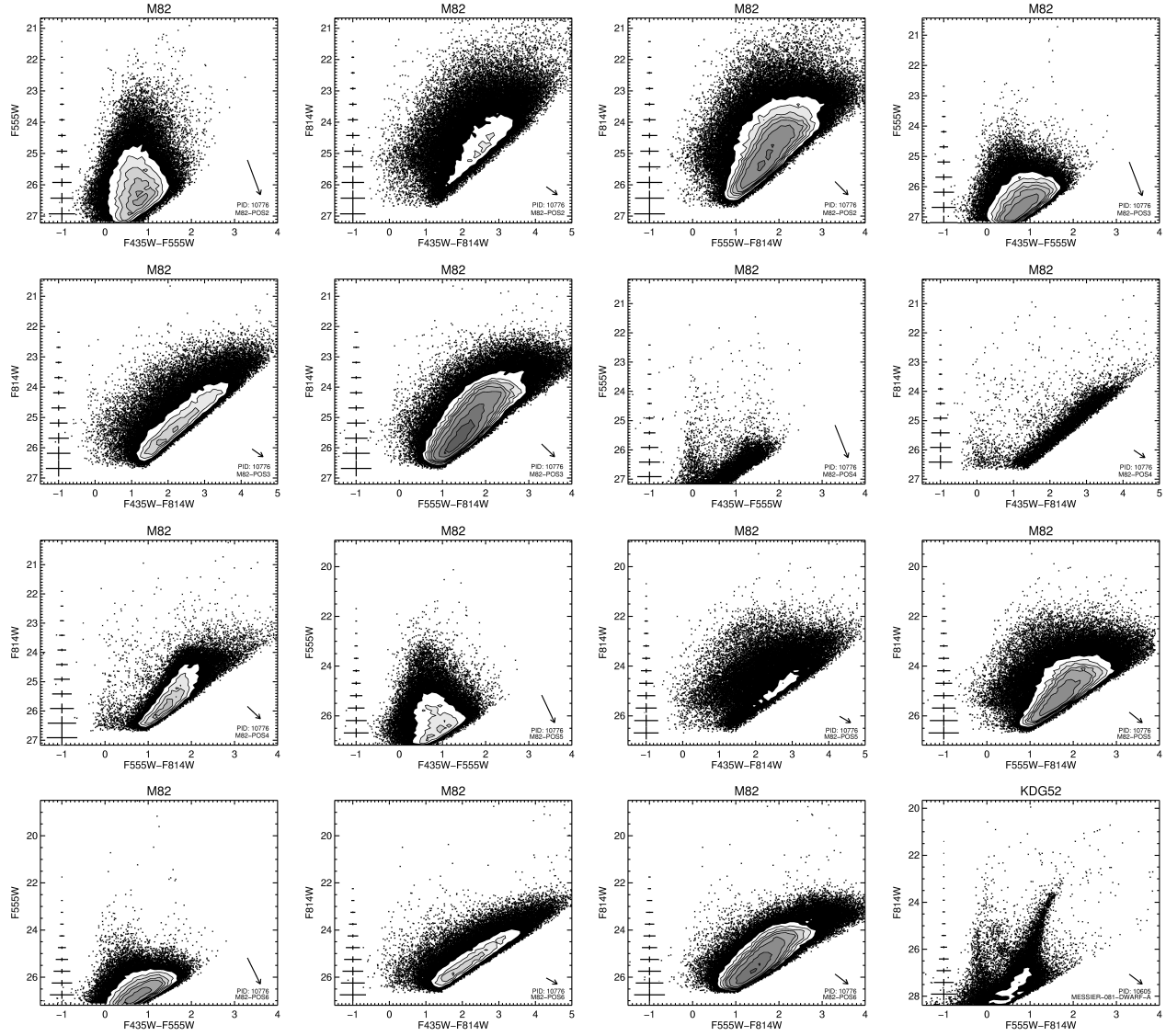


FIG. 15.— CMDs of galaxies in the ANGST data release, as described in Figure 9. Figures are ordered from the upper left to the bottom right. (a) M82; (b) M82; (c) M82; (d) M82; (e) M82; (f) M82; (g) M82; (h) M82; (i) M82; (j) M82; (k) M82; (l) M82; (m) M82; (n) M82; (o) M82; (p) KDG52;



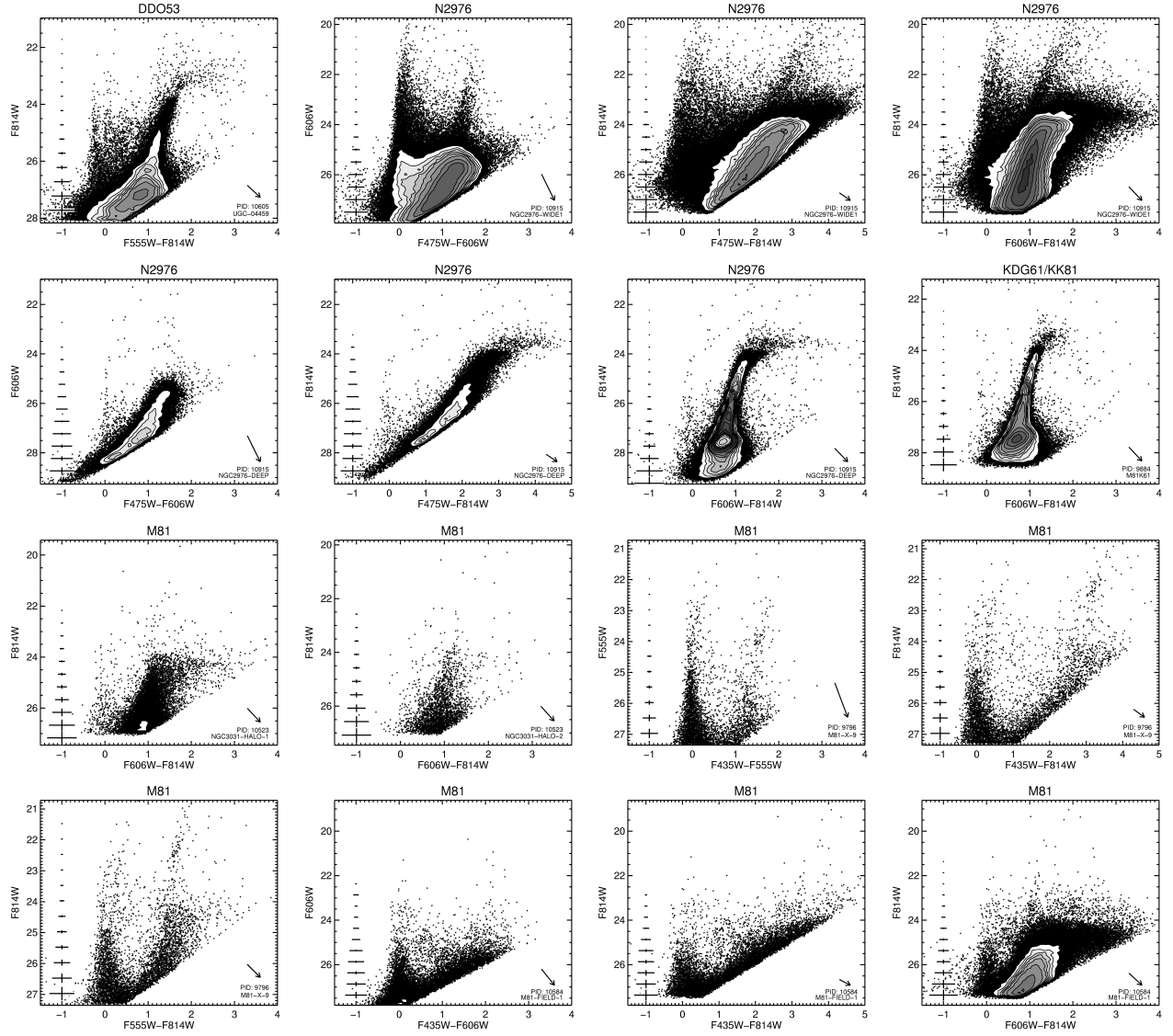


FIG. 16.— CMDs of galaxies in the ANGST data release, as described in Figure 9. Figures are ordered from the upper left to the bottom right. (a) DDO53; (b) N2976; (c) N2976; (d) N2976; (e) N2976; (f) N2976; (g) N2976; (h) KDG61; (i) M81; (j) M81; (k) M81; (l) M81; (m) M81; (n) M81; (o) M81; (p) M81;

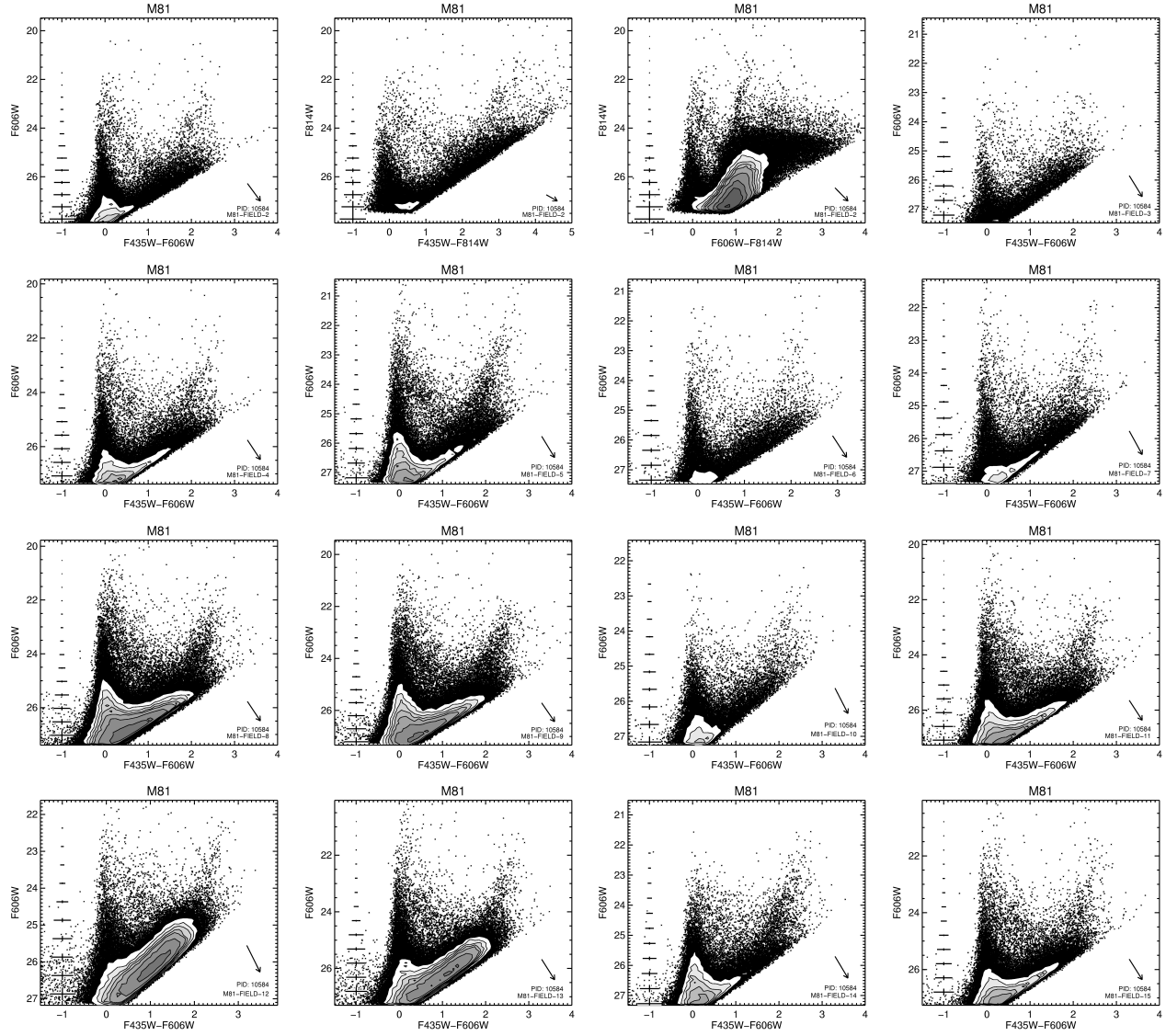


FIG. 17.— CMDs of galaxies in the ANGST data release, as described in Figure 9. Figures are ordered from the upper left to the bottom right. (a) M81; (b) M81; (c) M81; (d) M81; (e) M81; (f) M81; (g) M81; (h) M81; (i) M81; (j) M81; (k) M81; (l) M81; (m) M81; (n) M81; (o) M81; (p) M81;

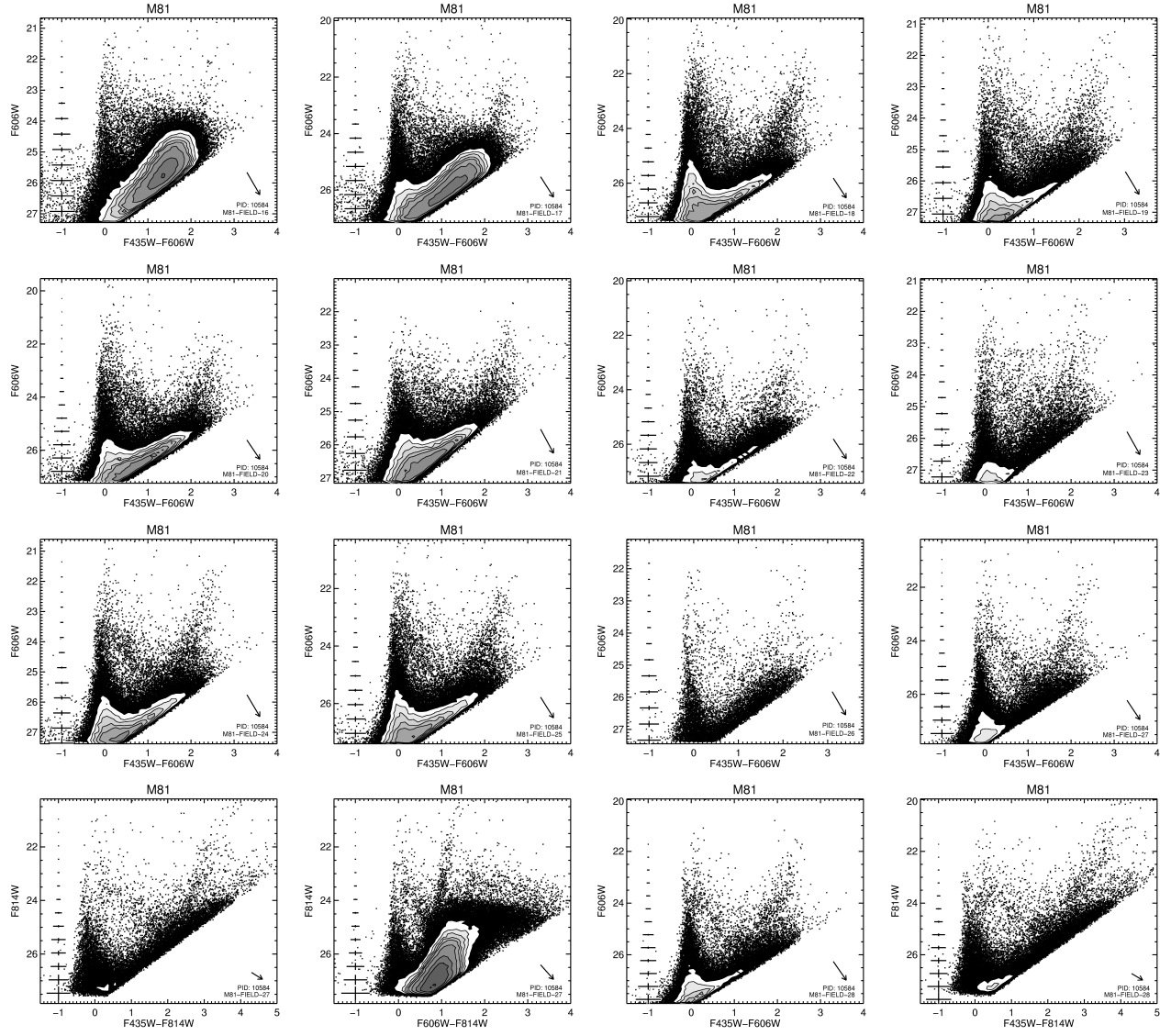


FIG. 18.— CMDs of galaxies in the ANGST data release, as described in Figure 9. Figures are ordered from the upper left to the bottom right. (a) M81; (b) M81; (c) M81; (d) M81; (e) M81; (f) M81; (g) M81; (h) M81; (i) M81; (j) M81; (k) M81; (l) M81; (m) M81; (n) M81; (o) M81; (p) M81;

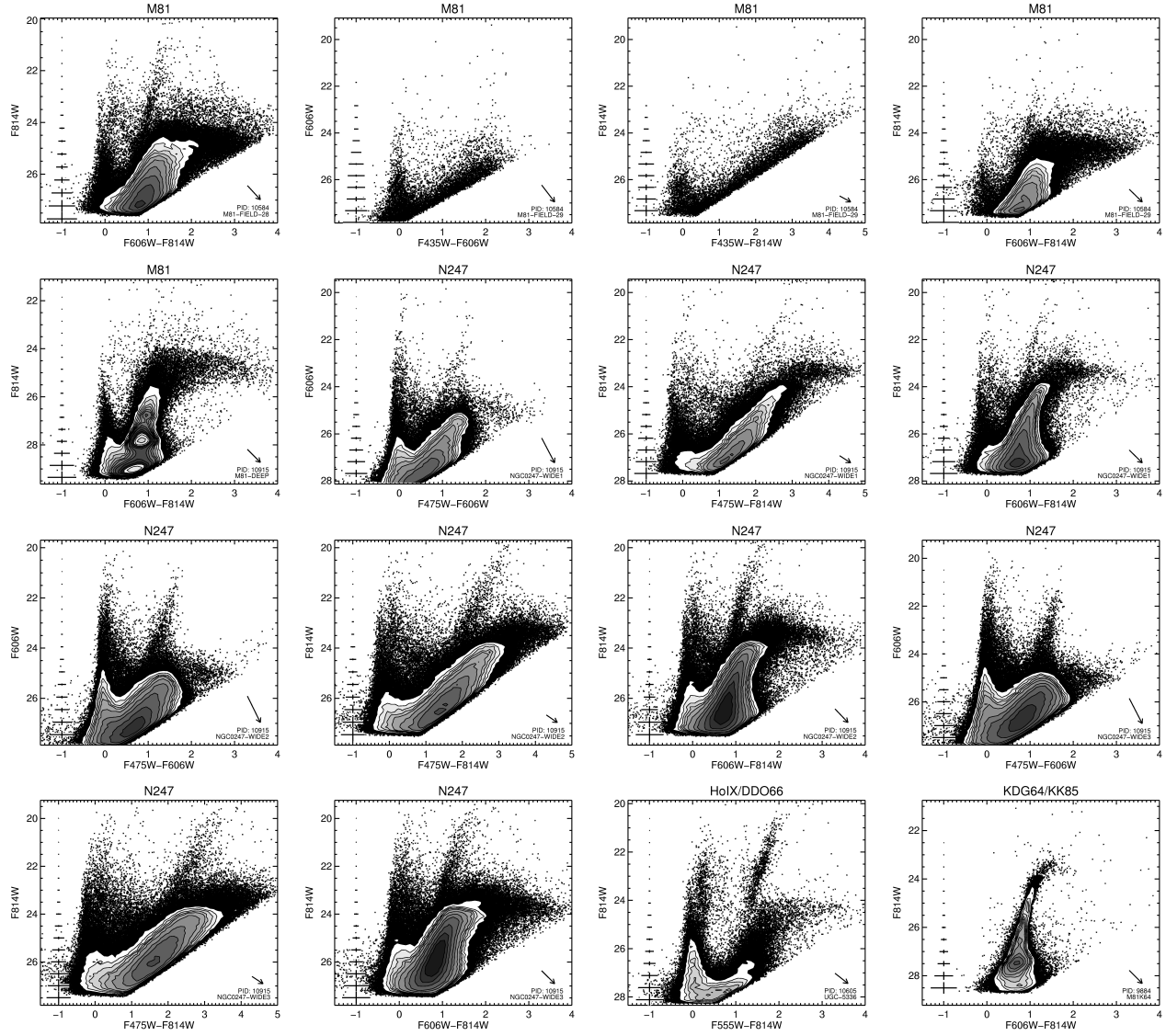


FIG. 19.— CMDs of galaxies in the ANGST data release, as described in Figure 9. Figures are ordered from the upper left to the bottom right. (a) M81; (b) M81; (c) M81; (d) M81; (e) M81; (f) N247; (g) N247; (h) N247; (i) N247; (j) N247; (k) N247; (l) N247; (m) N247; (n) N247; (o) HoIX; (p) KDG64;

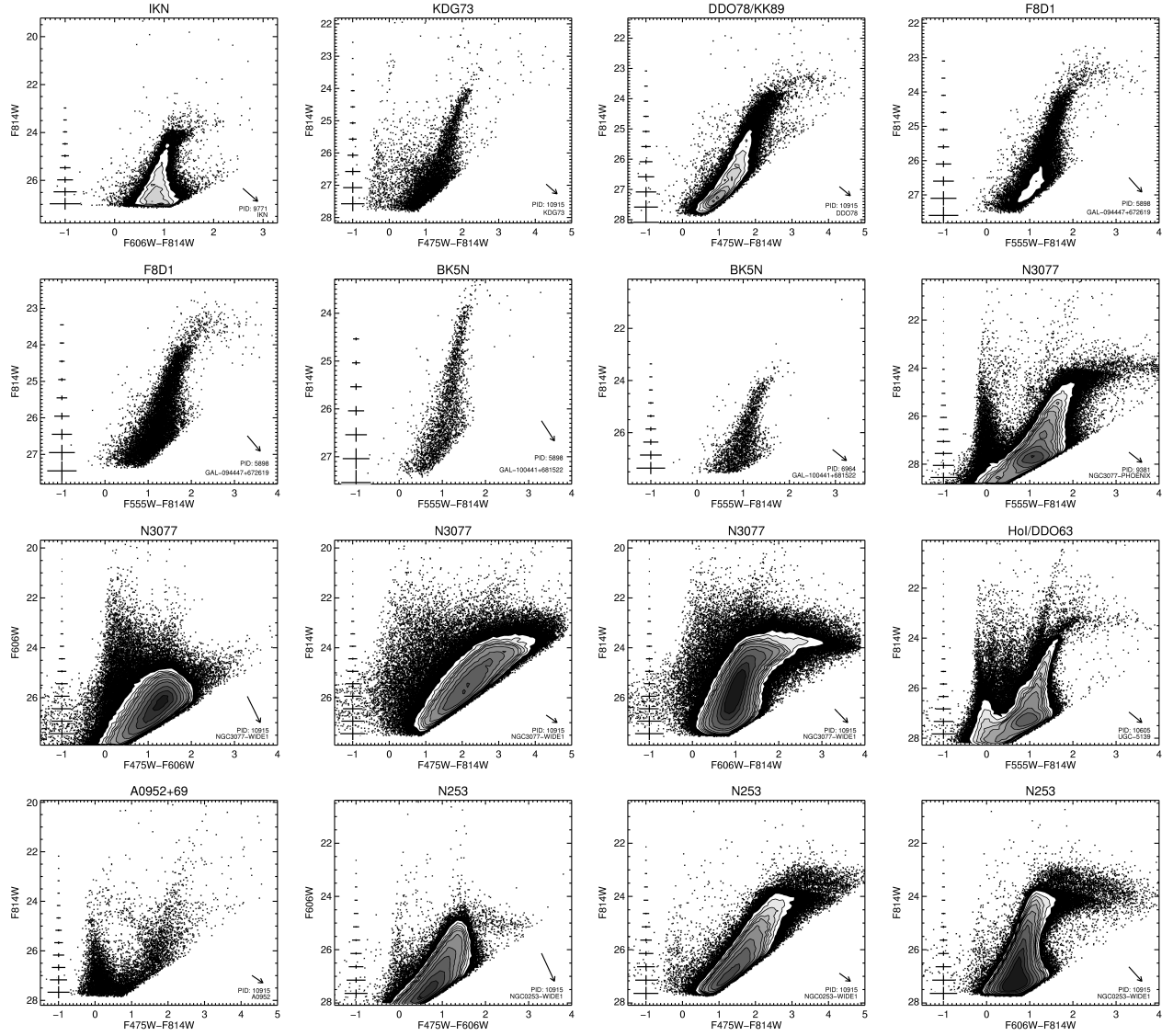


FIG. 20.— CMDs of galaxies in the ANGST data release, as described in Figure 9. Figures are ordered from the upper left to the bottom right. (a) IKN; (b) KDG73; (c) DDO78; (d) F8D1; (e) F8D1; (f) BK5N; (g) BK5N; (h) N3077; (i) N3077; (j) N3077; (k) N3077; (l) Hol; (m) A0952+69; (n) N253; (o) N253; (p) N253;

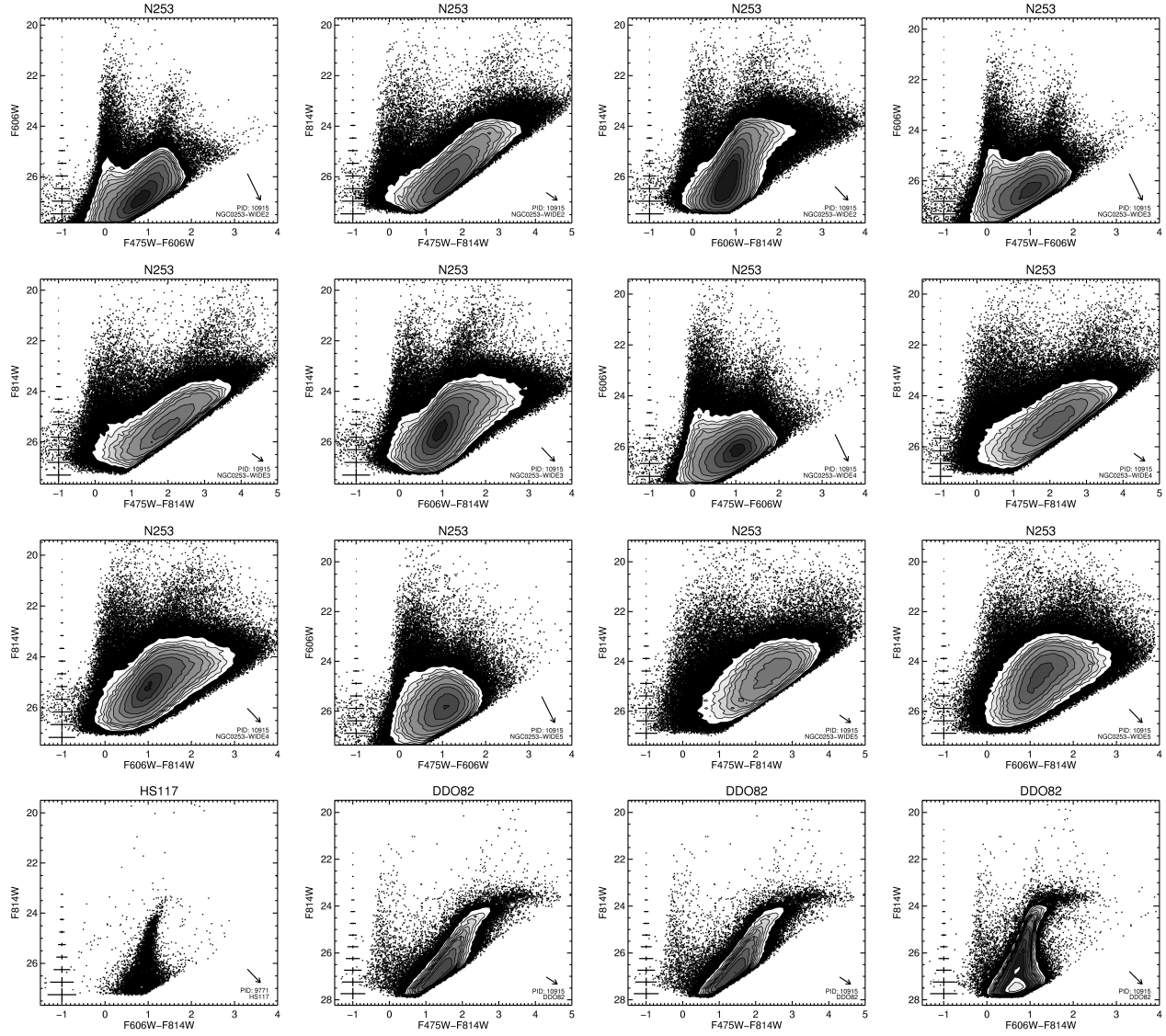


FIG. 21.— CMDs of galaxies in the ANGST data release, as described in Figure 9. Figures are ordered from the upper left to the bottom right. (a) N253; (b) N253; (c) N253; (d) N253; (e) N253; (f) N253; (g) N253; (h) N253; (i) N253; (j) N253; (k) N253; (l) N253; (m) HS117; (n) DDO82; (o) DDO82; (p) DDO82;

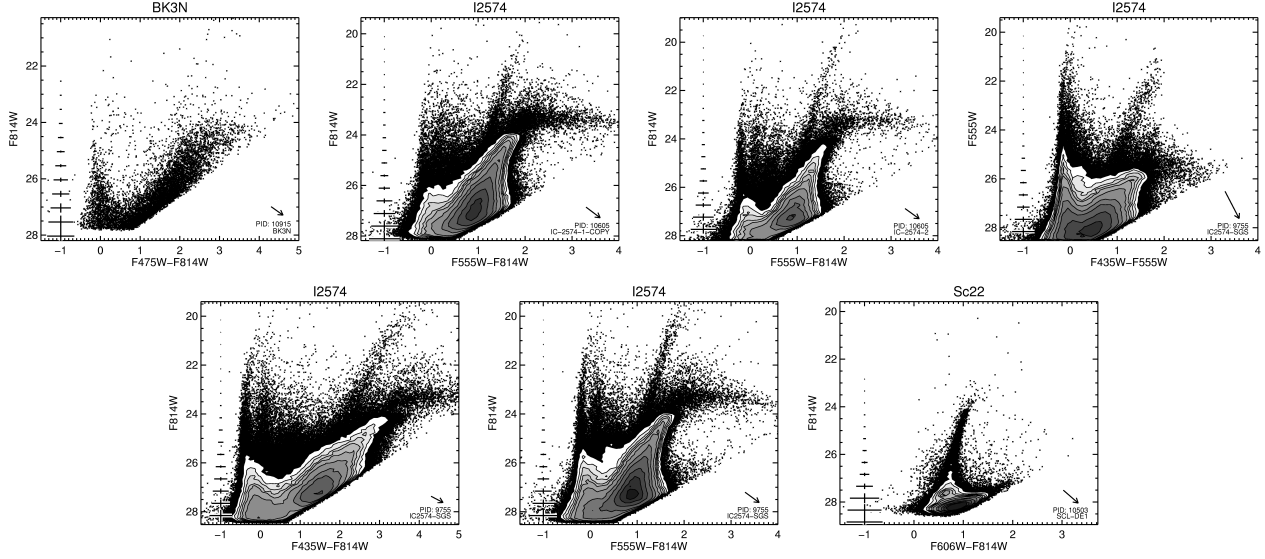


FIG. 22.— CMDs of galaxies in the ANGST data release, as described in Figure 9. Figures are ordered from the upper left to the bottom right. (a) BK3N; (b) I2574; (c) I2574; (d) I2574; (e) I2574; (f) I2574; (g) Sc22;

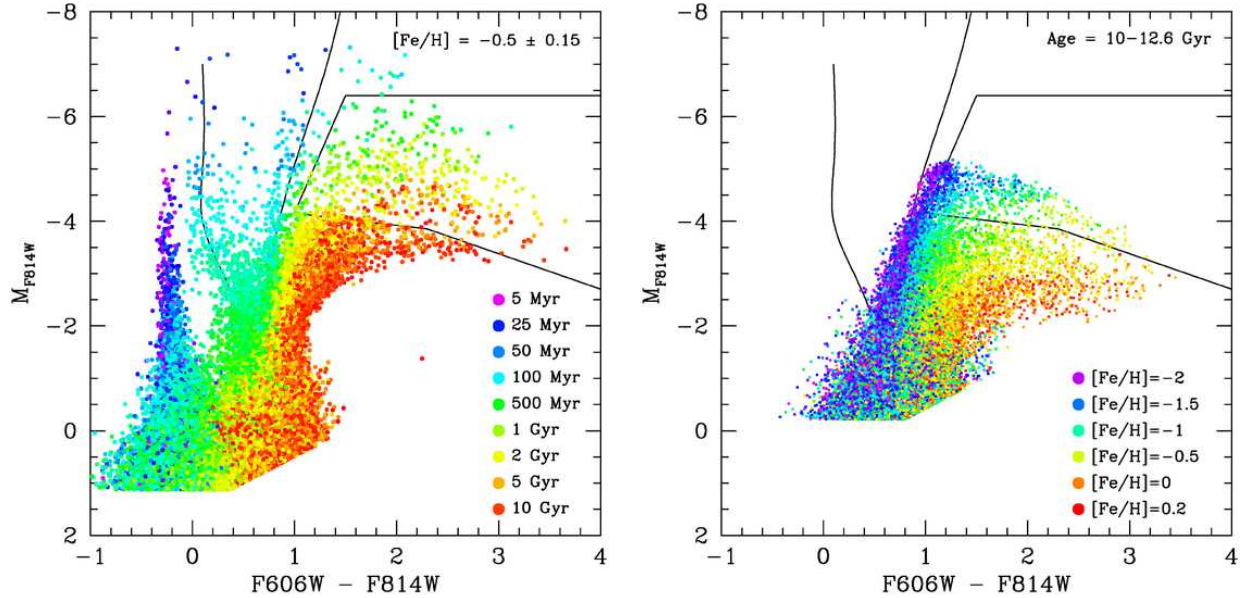


FIG. 23.— Simulated CMDs for a constant star formation rate color-coded by age (left) and for a uniform old age color-coded by metallicity (right). The panels adopt the photometric errors and biases for the NGC0300-WIDE1 (left) and NGC0253-WIDE1 (right) targets. The three (largely vertical) solid lines indicate several prominent sequences identified with young stellar populations: the main sequence (leftmost line), the blue core helium burning sequence (middle line), and the red core helium burning sequence (rightmost line). The enclosed polygon in the upper right indicates the region typically occupied by AGB stars. The simulated CMDs assume the most recent Girardi et al. (2008) isochrone set.

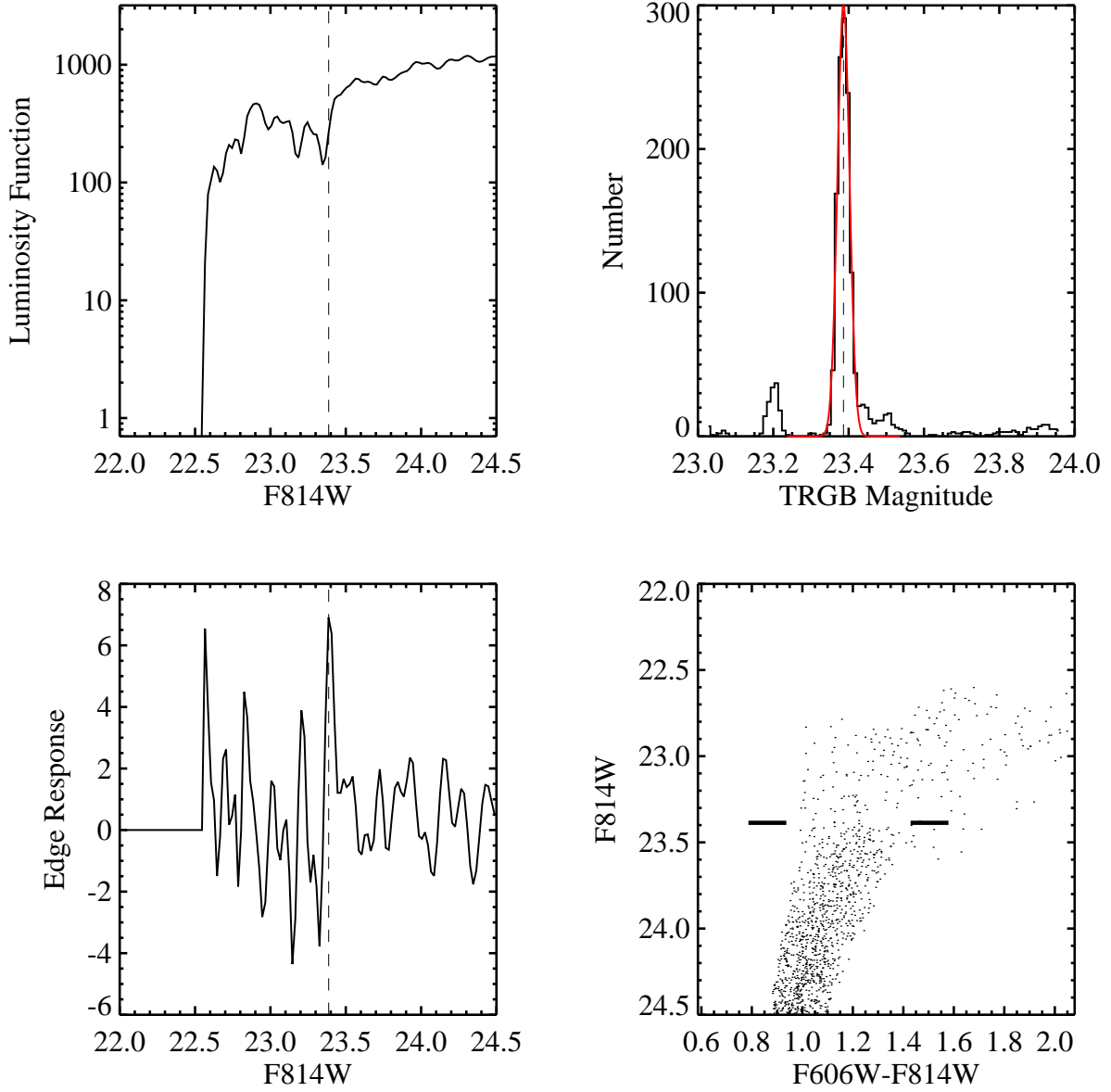


FIG. 24.— Results of TRGB fitting for NGC 2403, showing the  $F814W$  luminosity function (upper left), edge-detection response (lower left), distribution TRGB magnitudes from of Monte Carlo trials (upper right), and the CMD of stars used in the TRGB determination (lower right). The adopted TRGB magnitude is shown as the vertical line in the first three panels, and as the two horizontal tic marks in the lower right panel.



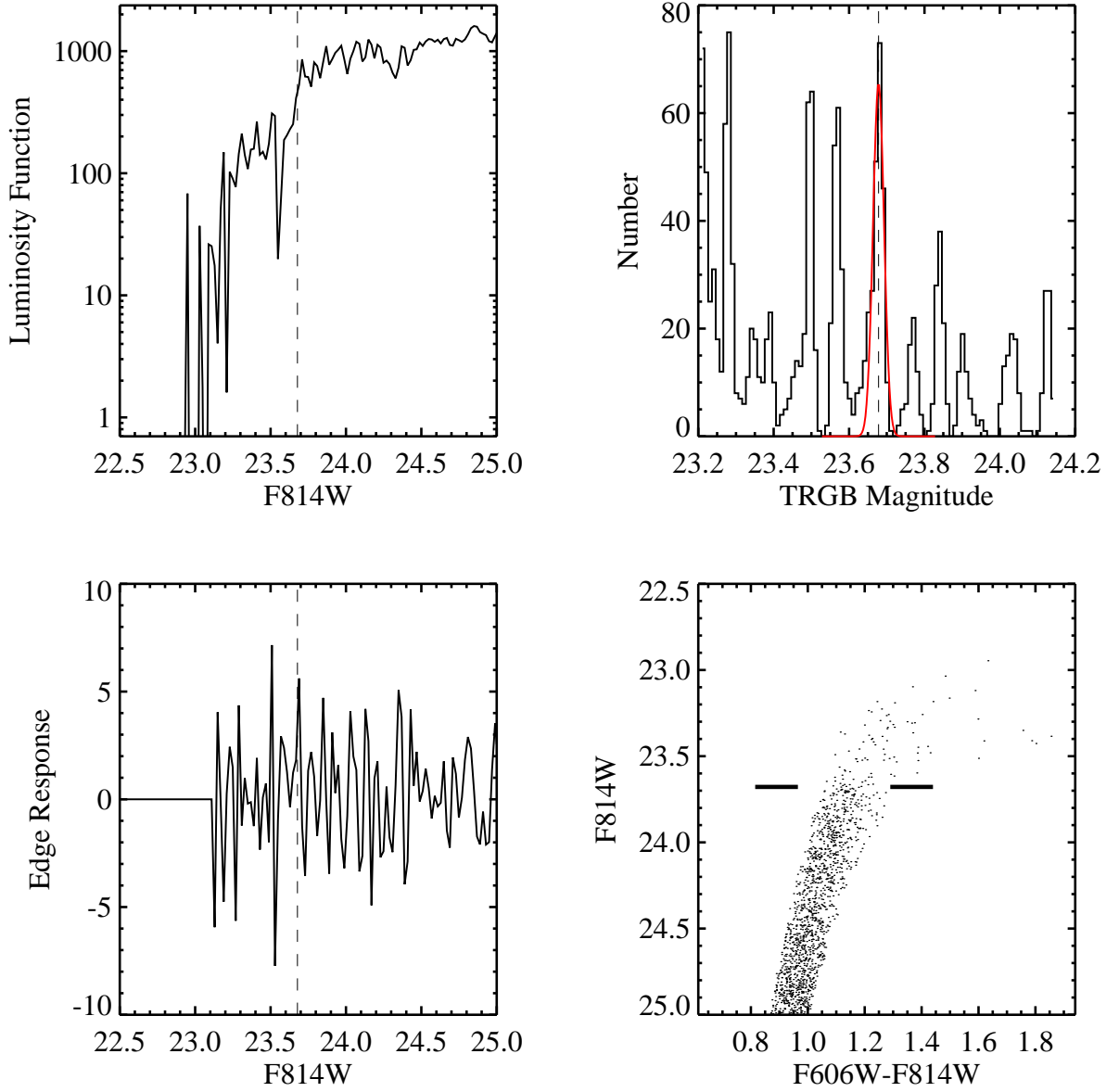


FIG. 25.— Results of TRGB fitting for KDG63. Panels are the same as in Figure 24. The histogram of Monte Carlo values is more complicated than in Figure 24, due to the smaller number of stars.

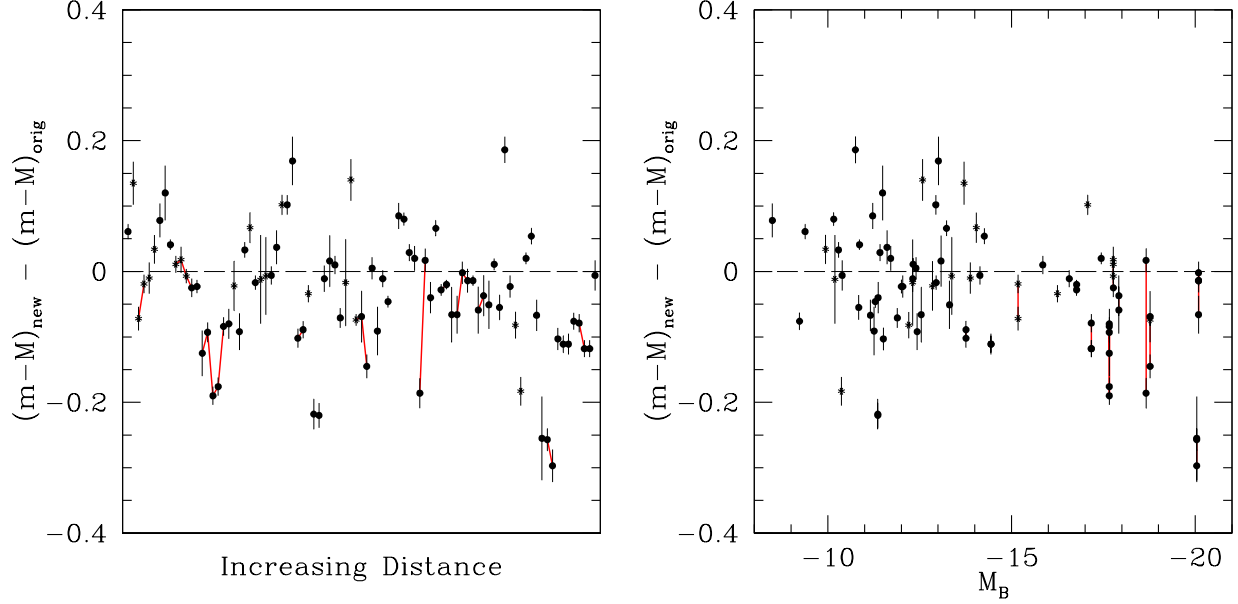


FIG. 26.— Differences between the new TRGB distance moduli and those used in Table 1 at the time of survey selection, as a function of either each target’s position in Table 5, which was sorted by the initial distance estimate (left) or absolute magnitude (right). Solid circles are used for ACS data and asterisk for WFPC2 data. Error bars indicate the Monte Carlo uncertainties reported in Table 5, but do not include systematic uncertainties due to dust extinction or the adopted TRGB absolute magnitudes. The median change in distance modulus is only  $-0.02$  mag, and the dispersion about the mean is  $0.05$  mag. Multiple observations of the same galaxy are connected with a solid line (for NGC 3109, NGC 55, NGC 300, NGC 4163, UA292, NGC 2403, M82, NGC 2976, M81, NGC 247, NGC 253, DDO82, and IC 2574), and show differences of typically less than  $0.1$  mag (i.e.  $10\%$  in distance). This variation is likely to be dominated by differences in internal extinction at different locations within the galaxy, with the outermost distance measurement being least likely to be affected by dust but more likely to be affected by Poisson uncertainties due to reduced numbers of stars.